# Numerical and Experimental Investigation of UV LED Water Treatment Reactor



## Jainil Shah

This thesis is submitted for the degree of Doctor of Philosophy

Supervisor: Professor George Aggidis

Engineering Department, Lancaster University

October 2025 – 26

#### Abstract

UV LED water treatment systems represent an emerging alternative to conventional mercury lamp reactors, offering energy efficiency, compact design, and environmental benefits. However, achieving effective pathogen inactivation in commercial-scale LED reactors requires optimized flow structures to ensure uniform UV dose distribution throughout the treated water. This thesis presents the first comprehensive investigation of swirl-enhanced flow dynamics in commercial-scale UV LED reactors through integrated computational and experimental approaches.

A validated CFD model was developed using ANSYS CFX with SST turbulence modeling, coupled with ray-tracing optical calculations to predict UV dose distribution. The model was rigorously validated through dual approaches: biodosimetry experiments using MS2 bacteriophage across nine operating conditions (three flow rates: 80-250 m³/h; three UV transmittance levels: 90-98%) achieved excellent agreement with the numerical model, well within experimental uncertainty (±29.4%). Particle Image Velocimetry measurements in a scaled reactor (DN200) validated flow field predictions for both tangential and axial velocity components.

The validated model quantified key performance drivers: stationary vanes contribute >97% of swirl generation (swirl number S = 0.37), providing 30% residence time enhancement leading to an improved mixing uniformity. Comprehensive geometric analysis established design guidelines: LED ring spacing <40 mm optimizes efficiency for UV transmittance <85%; upstream piping configurations (U-bends, T-junctions, reducers) produce <5% dose variation, eliminating straight-pipe installation requirements.

This research provides the first validated predictive framework for commercial UV LED reactor design, enabling rational optimization of geometric configurations, LED arrangements, and operating conditions. The findings have been implemented in commercial product development, reducing prototype testing requirements.

## Contents

| List of Figures  | i     |
|--|-------|
| List of Tables   | v     |
| Acknowledgements   | vi    |
| The author's declaration                                       | vii   |
| Chapter 1. Introduction  | 1     |
| 1.1. Water disinfection technologies and standards             | 1     |
| 1.1.1. Chemical Disinfection Methods                           | 1     |
| 1.1.2. UV Disinfection Technology                              | 2     |
| 1.1.3. Comparative Effectiveness and Combined Treatment Approa | ches3 |
| 1.1.4. Validation of the current UV treatment system           | 4     |
| 1.2. LED water treatment system                                | 4     |
| 1.3. Aims and Objectives                                       | 5     |
| Chapter 2. Literature Review                                   | 7     |
| 2.1. Hydraulic Systems   | 7     |
| 2.1.1 Effect of Geometry                                       | 7     |
| 2.1.2 Effect of lamps  | 9     |
| 2.1.3 Effect of Temperature                                    | 11    |
| 2.1.4 Effect of UVT  | 11    |
| 2.1.5 Effect of flow rate                                      | 12    |
| 2.2. Modelling of UV treatment System                          | 13    |
| 2.2.1. Modelling of flow (CFD)                                 | 15    |
| 2.2.2 UV modelling (UV dose)                                   | 17    |
| 2.3. Summary   | 18    |
| Chapter 3. Research Methodology                                | 20    |
| 3.1. Computational Fluid Dynamics                              | 20    |
| 3.1.1. Ansys CFX   | 20    |
| 3.1.2. Geometrical model                                       | 22    |
| 3.1.3. Geometrical Assumptions and Simplification              | 24    |
| 3.1.4. Mathematical Model                                      | 26    |
| 3.1.5. CFD Model Verification                                  | 41    |
| 3.2. PIV experimental methodology                              | 47    |
| 3.2.1 Test Rig Design and Scaling                              | 47    |
| 3.2.2 Optical Correction Box                                   | 48    |
| 3.2.3 Stationary Vane Manufacturing                            | 50    |

| 3.2.4 Additional Test Rig Components                                 | 52  |
|--|-----|
| 3.2.5 PIV Systems and procedures                                     | 53  |
| 3.2.6 Image Processing and Analysis                                  | 58  |
| 3.3. Validation of the model   | 61  |
| 3.3.1 Validation of the reactor for UV dose                          | 61  |
| 3.3.2 Validation of the Reactor Using PIV Experiments                | 63  |
| 3.4 Conclusion   | 64  |
| Chapter 4. Results and Discussion                                    | 66  |
| 4.1 Flow Characteristics in the Full-Scale UV LED Reactor            | 66  |
| 4.1.1 Residence Time Enhancement:                                    | 68  |
| 4.1.2 Velocity profile characteristics                               | 70  |
| 4.1.3 Swirl number analysis  | 73  |
| 4.1.4 Effect of flow rate on hydraulic performance                   | 74  |
| 4.2 UV dose  | 79  |
| 4.2.1 Baseline Dosage Distribution at Design Flow Rate               | 79  |
| 4.2.2 Influence of UV Transmittance on Dosage                        | 81  |
| 4.2.3 Effect of Flow Rate on UV dose Delivery                        | 82  |
| 4.2.4 Effect of LED Ring Configuration on Reactor Performance        | 85  |
| 4.3 Effect of Geometric Configuration on Reactor Performance         | 88  |
| 4.3.1 Impact of Heat Exchanger                                       | 88  |
| 4.3.2 Role of Individual Components in Flow Development and Mixing   | 89  |
| 4.3.3 Effect of Upstream Piping Configuration on Reactor Performance | 93  |
| 4.4 Conclusion   | 98  |
| Chapter 5. Experimental Results and Discussion                       | 100 |
| 5.1 Results for configuration 1                                      | 100 |
| 5.1.1 Vertical Plane Measurements                                    | 100 |
| 5.1.2 Velocity Contours  | 103 |
| 5.2 Configuration 2 results  | 107 |
| 5.3 Configuration 3 results  | 108 |
| 5.4 Conclusion   | 110 |
| Chapter 6. Model Validation  | 111 |
| 6.1 UV dose Validation with Biodosimetry Experiments                 | 111 |
| 6.1.1 Comparison Across UVT Conditions                               | 111 |
| 6.1.2 Systematic Trends and Model Accuracy                           | 114 |
| 6.1.3 Overall Validation Assessment                                  | 116 |
| 6.2 Flow Field Validation with PIV Experiments                       | 117 |

| 6.2.1 Swirl Number Comparison  | 117    |
|--|--------|
| 6.2.2 Axial Velocity Profile Comparison  | 118    |
| 6.2.3 Tangential Velocity Profile Comparison                                       | 119    |
| 6.2.4 Velocity Contour Comparisons   | 122    |
| 6.3 Summary of Validation Results:   | 125    |
| Chapter 7. Conclusions and Future Work   | 127    |
| 7.1 Summary  | 127    |
| 7.1.1 Model Validation:  | 128    |
| 7.1.2 Key Research Findings:   | 128    |
| 7.2 Contributions and Novelty  | 130    |
| 7.2.1 First Validated CFD-Optical Model for Commercial UV LED Reactors             | 130    |
| 7.2.2 Experimental Characterization of Swirl-Enhanced Flow in Large-Scale UV React | ors131 |
| 7.2.3 Quantitative Design Guidelines for Swirl-Enhanced UV LED Reactors            | 132    |
| 7.3 Recommendations for Future Work  | 134    |
| 7.3.1 Advanced Turbulence Modeling for High-Swirl Flows                            | 134    |
| 7.3.2 Multi-Reactor System Configurations  | 134    |
| 7.3.3 Optimization of Vane Geometry and Positioning                                | 135    |
| 7.3.4 Investigation of Reactor Scaling and Compact System Development              | 135    |
| 7.3.5 Energy Efficiency Optimization Through Adaptive Control                      | 135    |
| Glossary   | 136    |
| References   | 144    |

# List of Figures

| Figure 1-1: Chlorine dose vs UV dose vs TTHM for 4 log inactivation of pathogens            | 3      |
|---|--------|
| Figure 2-1:Layout of single lamp UV photo reactor   | 8      |
| Figure 3-1:A) Full scale water treatment plan in the Typhon Lab b) SolidWorks model ve      | ersion |
| of full-scale water treatment plant   | 24     |
| Figure 3-2: Full-scale domain geometry in Ansys DesignModeler                               | 27     |
| Figure 3-3: a): Identifying mesh in the entire geometry. Figure 3b): Mesh showing inflation | tion   |
| layer   | 30     |
| Figure 3-4: Streamline seeding points visualised in a 2d plane                              | 37     |
| Figure 3-5: Normalised velocity profile for all three components for all three mesh         | 46     |
| Figure 3-6: 3D representation of the experimental rig in SolidWorks                         | 47     |
| Figure 3-7: Preparation of the acrylic box around the clear pipe for PIV experimennts       | 49     |
| Figure 3-8: Manufactured acrylic box around the clear pipe for PIV experiments              | 49     |
| Figure 3-9: Manufactured static vanes using 3D printer                                      | 52     |
| Figure 3-10: PIV experimental setup with camera and laser                                   | 54     |
| Figure 3-11: PIV setup with laser fired up to show the seeding particles                    | 55     |
| Figure 3-12: Calibration section used for the calibration of the PIV experiments            | 57     |
| Figure 3-13: Image taken during PIV experiments showcasing the noise in the system d        | lue to |
| reflection  | 59     |
| Figure 3-14: Images taken in the PIV experiments without the seeding particles              | 59     |
| Figure 3-15: Images from the PIV experiments without the noise                              | 60     |
| Figure 3-16: The ePIV setup for post processing of the results                              | 60     |
| Figure 4-1: a) Location of the plane within the reactor b) View of the velocity contours    | at the |
| inlet of the reactor  | 67     |
| Figure 4-2: a) 5 streamlines within the reactor b) Reactor with 1000 streamlines            | 68     |
| Figure 4-3: u velocity component at entry and exit point of the reactor                     | 71     |
| Figure 4-4: w velocity component at entry and exit point of the reactor                     | 72     |
| Figure 4-5: v velocity component at entry and exit point of the reactor                     | 73     |
| Figure 4-6: Comparison of the Reynolds number with Swirl number                             | 75     |
| Figure 4-7: Velocity vector maps at entry and exit of the reactor for 100% flow rate        | 76     |
| Figure 4-8: Velocity vector maps at entry and exit of reactor at 200% flow rate             | 77     |

| Figure 4-9: Velocity vector maps at entry and exit of reactor for 50% flow rate7               | 8 |
|--|---|
| Figure 4-10: Velocity vector maps at entry and exit of reactor at 10% flow rate7               | 9 |
| Figure 4-11: a) Optical flow for a single LED b) Optical flow for all the LEDs8                | 0 |
| Figure 4-12: a) Fluence within the reactor for single cross section b) Cross section presented |   |
| of the reactor8  | 0 |
| Figure 4-13: RED dosage received by the water at 100% flow rate8                               | 1 |
| Figure 4-14: Comparison of the normalised UV dose vs UVT8                                      | 2 |
| Figure 4-15: Relationship between LED power, Flow rate and MS2 RED8                            | 4 |
| Figure 4-16: Relationship between UVT, LED power and Flow rate8                                | 5 |
| Figure 4-17: Comparison for the number of LED rings for the ratio of LED power and flow        |   |
| rate with MS2 dosage at 73 UVT8  | 6 |
| Figure 4-18: Comparison for the number of LED rings for the ratio of LED power and flow        |   |
| rate with MS2 dosage at 88 UVT8  | 7 |
| Figure 4-19: Comparison for the number of LED rings for the ratio of LED power and flow        |   |
| rate with MS2 dosage at 98 UVT8  | 7 |
| Figure 4-20: Comparison of UVT vs MS2 dosage for different number of LED rings8                | 8 |
| Figure 4-21: Comparison of UV dose against UVT for both with and without heat exchanger        |   |
| 8  | 9 |
| Figure 4-22: Streamline presentation for the three different configuration of the reactor 9    | 0 |
| Figure 4-23: Maximum dosage received by the water for reactor only, reactor with elbow         |   |
| and full assembly configuration9   | 2 |
| Figure 4-24: Mean dosage received by the water for reactor only, reactor with elbow and        |   |
| full assembly configuration9   | 3 |
| Figure 4-25: Dosage distribution for Maximum dosage received by the water for reactor          |   |
| only, reactor with elbow and full assembly configuration9                                      | 3 |
| Figure 4-26: Geometrical representation of the changes to the upstream components -            |   |
| Upstream U, Upstream Elbow and Upstream TEE9   | 4 |
| Figure 4-27: Geometrical representation of the changes to the upstream components -            |   |
| Upstream reducer DN300 to DN150, DN300 to DN200 and DN300 to DN 2509                           | 4 |
| Figure 4-28: Normalised velocity components for all upstream geometrical configuration9        | 6 |
| Figure 4-29: Relationship between LED power, UV dose and Flow rate for different upstream      | า |
| components for 3 different UVT9  | 7 |

| Figure 5-1: Axial velocity profile from the experimental results at entry and exit point for  |
|---|
| vertical plane  |
| Figure 5-2: Tangential velocity profile from the experimental results at entry and exit point |
| for vertical plane  |
| Figure 5-3: Axial velocity profile from the experimental results at entry and exit point for  |
| horizontal plane  |
| Figure 5-4: Tangential velocity profile from the experimental results at entry and exit point |
| for horizontal plane103   |
| Figure 5-5: Velocity contours for axial and tangential velocity components for 87 m3/h flow   |
| rate for vertical plane104  |
| Figure 5-6: Velocity contours for axial and tangential velocity components for 132 m3/h flow  |
| rate for vertical plane104  |
| Figure 5-7: Velocity contours for axial and tangential velocity components for 175 m3/h flow  |
| rate for vertical plane105  |
| Figure 5-8: Velocity contours for axial and tangential velocity components for 87 m3/h flow   |
| rate for horizontal plane106  |
| Figure 5-9: Velocity contours for axial and tangential velocity components for 132 m3/h flow  |
| rate for horizontal plane   |
| Figure 5-10: Velocity contours for axial and tangential velocity components for 175 m3/h      |
| flow rate for horizontal plane  |
| Figure 5-11: Comparison of the axial and tangential velocity profile for the Upstream vanes   |
| with Downstream vanes configuration108  |
| Figure 5-12: Comparison of the axial and tangential velocity profile with Upstream vanes      |
| with Downstream vanes configuration109  |
| Figure 6-1: Comparison of the RED dosage vs UVT for 125 m3/h flow rate for experimental       |
| result vs numerical result  |
| Figure 6-2: Comparison of the RED dosage vs UVT for 250 m3/h flow rate for experimental       |
| result vs numerical result  |
| Figure 6-3: Comparison of the RED dosage vs UVT for 80 m3/h flow rate for experimental        |
| result vs numerical result  |
| Figure 6-4: Difference between the experimental result and model result in percentage for     |
| all flow rates  |

| Figure 6-5: RED comparison of the experimental result vs numerical model result117          |
|---|
| Figure 6-6: Comparison of swirl number between experimental and numerical results118        |
| Figure 6-7: Comparison of the experimental results with the numerical results for 87, 132   |
| and 175 m3/h flow rate119   |
| Figure 6-8: Comparison of the tangential velocity for experimental and numerical at 87 m3/h |
| flow rate120  |
| Figure 6-9: Comparison of the tangential velocity for experimental and numerical at 132     |
| m3/h flow rate121   |
| Figure 6-10: Comparison of the tangential velocity for experimental and numerical at 175    |
| m3/h flow rate122   |
| Figure 6-11: Comparison of the velocity contours for experimental vs the numerical results) |
| at 87 m3/h flow rate123   |
| Figure 6-12: Comparison of the velocity contours for experimental vs the numerical results  |
| at 132 m3/h flow rate124  |
| Figure 6-13: Comparison of the velocity contours for experimental vs the numerical results  |
| at 175 m3/h flow rate125  |

## List of Tables

| Table 1-1: Effectiveness of disinfection processes against pathogens                         | 3    |
|--|------|
| Table 1-2: Comparison of Mercury Lamps with LED lamps  | 4    |
| Table 2-1: Fluid flow vs Turbulence model vs UV dose modelling                               | 18   |
| Table 3-1: Mesh quality and statistics   | 29   |
| Table 3-2: Domain properties and material definition   | 31   |
| Table 3-3: Named selections, boundary conditions, and justification                          | 32   |
| Table 3-4: Solver control settings and justification   | 34   |
| Table 3-5: Solver definition and computational resources                                     | 35   |
| Table 3-6: Grid convergence results normalized to the coarsest grid for mesh refinement .    | 43   |
| Table 3-7: Grid convergence criteria for mesh refinement                                     | 45   |
| Table 3-8: Lab flow conditions for PIV experiments   | 53   |
| Table 4-1: Comparison of swirl number at inlet and exit of the reactor for different flow ra | ates |
|  | 74   |
| Table 4-2: Dosage Delivery Efficiency Comparison for Different LED Ring Configurations       | 86   |
| Table 4-3: Comparison of swirl intensities for different configuration                       | 91   |

## Acknowledgements

I would like to express my profound gratitude to all those who have contributed to the successful completion of this doctoral research.

First and foremost, I am really grateful to my academic supervisor, Professor George Aggidis, for his invaluable guidance, unwavering support, and mentorship throughout my doctoral journey. His expertise, encouragement, and insightful feedback have been instrumental in shaping this research and my development as a researcher.

I am immensely grateful to my industrial supervisor, Dr. Audrius Židonis, whose technical insight, consistent support, and practical guidance have been crucial to the success of this project. I also wish to acknowledge Dr. Matt Simpson for his valuable contributions and support throughout various stages of this research.

This research would not have been possible without the financial support and collaborative partnership provided by Typhon Treatment Systems Ltd (now NUUV). I am particularly grateful for the opportunity to work on this industrially relevant project and for access to the technical data, and the patented reactor design that formed the foundation of this investigation.

I extend special thanks to the technical staff at Lancaster University, whose assistance with the experimental rig design, PIV system setup, and laboratory facilities was essential for the successful completion of the experimental validation work.

On a personal note, I am profoundly grateful to my wife for her endless encouragement, patience, and unwavering support, particularly during the challenging phases of experimental work and thesis writing. I would also like to thank my family for their constant love, support, and words of encouragement that sustained me throughout this journey.

Finally, I acknowledge the examiners for their thorough review and constructive feedback, which has strengthened the quality and rigor of this thesis.

## The author's declaration

The author declares that this thesis has not been previously submitted for award of a higher degree to this or any university, and that the contents, except where otherwise stated, are the author's own work.

## Chapter 1. Introduction

Safe drinking water is a fundamental human right. Drinking water is available from surface water and ground water sources. These water bodies contain several different types of contamination such as bacteria, parasites and viruses. Such contamination can lead to various waterborne diseases. Treating water becomes essential, and international organizations like the World Health Organization (WHO), along with national regulatory bodies such as the US Environmental Protection Agency (EPA) and the European Union's Drinking Water Directive, have established comprehensive standards for water quality delivered to consumers [1].

Water treatment practices date back to 2000 BC, when ancient civilizations filtered water through sand and gravel to improve turbidity and taste [2]. Since then, the discovery of pathogenic microorganisms has driven scientists to develop increasingly sophisticated treatment methods. The first municipal water treatment plant was established in Paisley, Scotland in 1804, using slow sand filtration [3]. Following John Snow's 1854 discovery linking cholera outbreaks to contaminated water supplies, he advocated for water treatment, though chlorination was not widely adopted until the early 1900s [4]. While chlorination successfully reduced waterborne diseases such as cholera and typhoid, concerns about disinfection byproducts and their potential health effects have led to the development of alternative and supplementary disinfection methods. International standards for water treatment have evolved accordingly, with organizations worldwide establishing guidelines to ensure public health protection while minimizing treatment risks [5].

## 1.1. Water disinfection technologies and standards

Drinking water regulations typically require 3-log (99.9%) reduction for Giardia cysts and 4-log (99.99%) reduction for viruses to ensure public safety [6]. Various disinfection methods are available to achieve these standards, each with distinct advantages and limitations.

#### 1.1.1. Chemical Disinfection Methods

Chlorination is the most common disinfectant used worldwide, applied as chlorinate ions in either liquid or gaseous form. The major advantage of chlorination is that residual chlorine maintains water quality throughout the distribution system until it reaches consumers.

Additionally, chlorination is simple to implement and cost-effective compared to other processes. The World Health Organization (WHO) has established guidelines for chlorine usage in water disinfection. However, chlorine presents several disadvantages. As a hazardous chemical, chlorine mishaps can cause serious injuries or fatalities throughout its lifecycle from transportation to on-site usage. Its reactive nature is both beneficial for disinfection and dangerous for handling [4], [5]. Furthermore, chlorine produces disinfection by-products (DBPs), and due to the harmful nature of DBPs, regulatory guidelines limit chlorine dosages to minimize by-product formation. Chlorine also shows limited effectiveness against certain microorganisms, particularly Cryptosporidium [7]. The 1993 Milwaukee outbreak affected over 400,000 people, demonstrating this vulnerability [8].

Alternative chemical disinfectants include chloramine, chlorine dioxide, and ozone. Ozone provides effective treatment and superior control of taste and odor compared to chlorine [9]. Like chlorine, ozone is hazardous and produces its own by-products with potential health effects. While bromine serves as an alternative disinfectant in some applications, its use in potable water treatment remains limited due to cost and regulatory considerations [10].

#### 1.1.2. UV Disinfection Technology

UV treatment offers a non-chemical alternative that produces no chemical by-products and provides instantaneous disinfection without chemical handling requirements. UV systems predominantly use low or medium-pressure mercury lamps. Low-pressure mercury lamps produce nearly monochromatic light at 253.7 nm, which closely matches the 260-265 nm peak absorption of nucleic acids that disrupts pathogen DNA. Medium-pressure lamps produce polychromatic light (200-400 nm), providing broader spectrum coverage but with lower germicidal efficiency at the critical wavelengths. The UV dose, defined as the product of UV intensity and exposure time (mJ/cm²), determines treatment effectiveness [5], [11], [12].

UV disinfection reactors are classified into three categories: external (lamps outside the flow with UV transmitted through quartz windows), distributive (UV transmitted via optical fibres or light guides from external sources), and immersive (lamps placed directly in the water flow). The immersive type, with lamps oriented perpendicular or parallel to flow direction, dominates commercial applications [13], [14].

#### 1.1.3. Comparative Effectiveness and Combined Treatment Approaches

Table 1-1 presents the relative effectiveness of disinfection processes against different pathogen types, for achieving required log reductions at standard CT values (concentration × time) [15], [16], [17], [18].

| Types      | of | Free chlorine | Chloramine | Chlorine  | Ozone     | UV        |
|------------|----|---------------|------------|-----------|-----------|-----------|
| pollutants |    |               |            | dioxide   |           |           |
| Bacteria   |    | Excellent     | Good       | Excellent | Excellent | Good      |
| Viruses    |    | Excellent     | Fair       | Excellent | Excellent | Fair      |
| Protozoa   |    | Fair to poor  | poor       | Good      | Good      | Excellent |

While ozone and UV could theoretically eliminate chlorine by-products when used together, practical considerations including cost, operational complexity, and the need for residual protection in distribution systems make complete chlorine replacement challenging. Figure 1-1 illustrates the relationship between chlorine dose, UV dose, and trihalomethane (TTHM) formation for achieving 4-log pathogen reduction. Combined UV-chlorine treatment can reduce chlorine requirements by up to 50%, substantially decreasing TTHM formation while maintaining regulatory compliance [19].

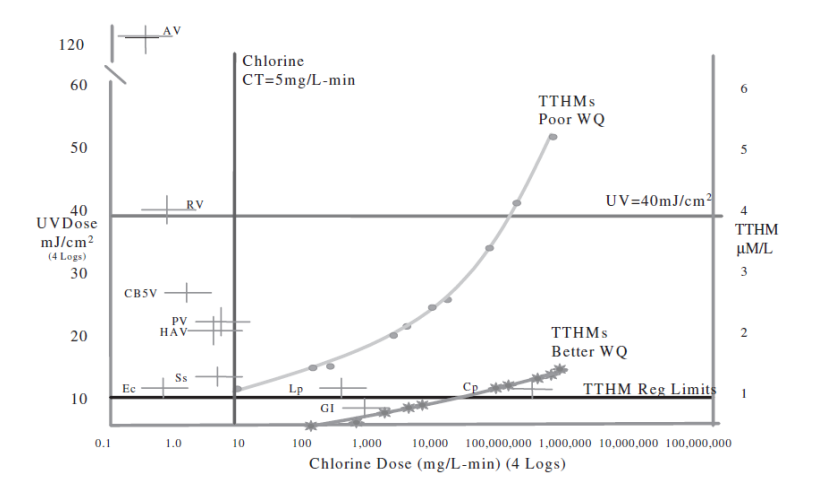


Figure 1-1: Chlorine dose vs UV dose vs TTHM for 4 log inactivation of pathogens

#### 1.1.4. Validation of the current UV treatment system

System validation follows the bioassay protocol as the industry standard, where MS2 bacteriophage is introduced upstream and measured downstream to determine log reduction. Performance is evaluated using Reduction Equivalent Dose (RED), which accounts for the minimum dose received, rather than average dosage which can mask inadequate treatment zones. While research explores alternative validation methods including monitored tunable biodosimetry (MTB) and photochromic materials, commercial systems continue using traditional biodosimetry for regulatory compliance [6], [20].

#### **1.2.** LED water treatment system

Mercury-based UV systems face several limitations that LED technology addresses. Table 1-2 compares the key characteristics of mercury lamps and LED systems for water treatment applications [5], [7], [11], [21].

Table 1-2: Comparison of Mercury Lamps with LED lamps

| Parameter        | Mercury Lamps  | LED lamps                     |  |  |
|------------------|--|-------------------------------|--|--|
| Material         | Contains toxic mercury (5-                           | No toxic materials            |  |  |
|                  | 400mg per lamp)                                      |                               |  |  |
| Warm-up time     | 5-10 minutes to reach full Instant on/off capability |                               |  |  |
|                  | intensity  |                               |  |  |
| Energy efficient | 35-40% for LP mercury at                             | 2-5% wall-plug efficiency for |  |  |
|                  | 254nm  | UVC LEDs at 275nm             |  |  |
| Life span        | 8,000-16,000 operational                             | 10,000-20,000 hours (with     |  |  |
|                  | hours  | 70% output retention)         |  |  |
| Carbon footprint | Higher due to mercury                                | Lower due to reduced          |  |  |
|                  | disposal requirements and                            | hazardous waste and longer    |  |  |
|                  | shorter replacement cycles operational life          |                               |  |  |

While mercury lamps currently demonstrate superior electrical efficiency for UVC generation (35-40% versus 2-5% for LEDs), LED technology offers significant operational advantages. The instant on/off capability eliminates warm-up periods, reducing energy waste during intermittent operation. LEDs contain no toxic materials, eliminating mercury disposal

concerns and associated environmental regulations. Additionally, their longer operational lifespan of 10,000-20,000 hours compared to 8,000-16,000 hours for mercury lamps reduces maintenance frequency and replacement costs [22].

Extensive research has validated LED effectiveness for water disinfection at bench scale [22]. Recent advances have enabled the first full-scale UV-LED drinking water disinfection systems for municipal applications, demonstrating equivalent water quality and treatment capacity to mercury-based systems [23]. These installations mark a significant milestone in LED technology adoption for large-scale water treatment.

The United Nations Environmental Program's Minamata Convention aims to phase out mercury and mercury-containing products globally. While UV-mercury lamps are not explicitly mentioned, this convention signals the international commitment to eliminating mercury usage, creating regulatory pressure for alternative technologies [24].

The Drinking Water Inspectorate (DWI), the water quality regulator for England and Wales, reported in 2017 that UV treatment systems processed 1,492 MI/d through 139 units, representing approximately 10% of total water treatment capacity [25]. This indicates substantial opportunity for increased implementation of UV treatment processes, particularly as LED technology matures and efficiency improves.

The transition from mercury to LED-based UV systems represents a critical evolution in water treatment technology, driven by environmental regulations, operational advantages, and improving LED performance despite current efficiency limitations.

## 1.3. Aims and Objectives

#### Aim

The aim of this thesis is to develop and validate a comprehensive computational methodology for predicting flow behaviour and UV dose distribution in a large-scale commercial UV LED-based water treatment plants, addressing the critical gap in reactor performance for municipal water treatment applications.

#### **Objectives**

To achieve this aim, the following strategic objectives were established:

- Develop a validated CFD modeling framework for UV LED water treatment systems
  that accurately captures the complex flow dynamics induced by internal geometric
  features (static vanes, elbows) and predicts their impact on treatment efficiency.
- Establish the relationship between hydraulic characteristics and UV dose distribution by integrating CFD-generated flow field data with optical radiation modeling to quantify treatment performance across varying operational conditions (flow rates, UVT values).
- Experimentally validate the computational methodology through:
  - Use results from Biodosimetry experiments to verify predicted UV dose
  - PIV measurements to confirm flow structure predictions and mixing characteristics
- Quantify the influence of geometric design parameters on reactor performance, including the effects of static vane positioning, upstream configurations, and scale effects on dosage uniformity and treatment efficiency.
- Develop design guidelines and optimisation strategies for commercial LED water treatment systems based on the validated modeling framework, enabling prediction of optimal operating conditions for different water quality parameters.

These objectives directly support the development of the first comprehensive modeling approach for commercial-scale UV LED water treatment plants, filling a significant gap in current literature which has focused primarily on mercury-based systems or small-scale LED applications.

## Chapter 2. Literature Review

This chapter examines the current state of knowledge in UV water disinfection systems, with particular emphasis on the computational and experimental approaches used to understand and optimize reactor performance. The review first addresses the modelling methodologies employed for UV treatment systems, including both flow dynamics (CFD) and UV dose calculations. Subsequently, the hydraulic characteristics affecting UV reactor performance are analysed, examining geometric configurations, lamp arrangements, and operational parameters. Finally, the computational fluid dynamics techniques and governing equations used in reactor modelling are discussed. This comprehensive review establishes the theoretical foundation and identifies knowledge gaps that this research aims to address.

## 2.1. Hydraulic Systems

UV reactor configurations are broadly categorized into two primary topologies: open channel and closed channel reactors [17]. Figure 2.1 illustrates these configurations and their inlet/outlet arrangements. Closed channel reactors predominantly serve drinking water applications due to their ability to maintain system pressure and prevent contamination. Open channel reactors are typically employed for wastewater treatment, though research has explored their application in drinking water systems where their highly turbulent flow characteristics can reduce installation costs. Conversely, closed reactors have been investigated for wastewater applications despite traditionally serving potable water treatment [8], [17]

#### 2.1.1 Effect of Geometry

Under ideal conditions for the closed channel reactor, there is a complete mixing of the water flow inside the reactor, i.e. plug flow, which will lead to equal distribution of the UV dose. This, however, is not possible in real flow conditions because the flow of particles inside the reactor is unique and thus will receive unique dosage. Hence, the calculation of the UV dose is in terms of distribution rather than a fixed value [2]. There are various hydraulic features, which affect the dosage received by the water. One of the easiest changes made includes the inlet and outlet location. Offsetting the reactor inlet and outlet leads to better mixing of the water [26]. Based on inlet-outlet location, there are different types of reactors such as L type,

reverse L type, linear type, and U type. The L type reactor has the inlet perpendicular to the axis of the reactor while outlet is parallel. Reverse L type has an inlet parallel and outlet perpendicular to the axis of the reactor. The linear type has both inlet and outlet parallel to the axis of the reactor. U type of reactor has inlet and outlet both perpendicular to the axis of the reactor. U type and L type are more turbulent compared to the other two because of the perpendicular inlet. L type of reactor performed better than the U type of reactor for set conditions in terms of fluence distribution. Geometrical changes brought different results in terms of distribution and treatment of water. Changes in the dimensions of the reactor introduce changes in the dosage received by the water. While in general, the increase in the length of the reactor and decreasing the cross-section area of the reactor improves the reactor performance for the U type reactor. Figure 2.1 shows different type of inlet outlet location as discussed above. [27].

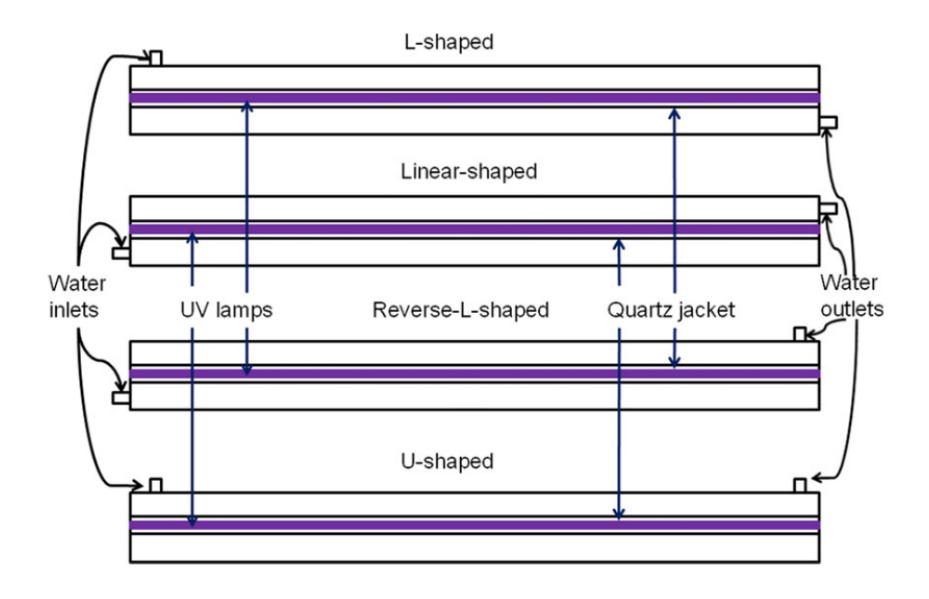


Figure 2-1:Layout of single lamp UV photo reactor

Changes in the shape of the reactor can remove dead zones (areas that receive no dosage). Accomplished by flattening the reactor instead of the complete circular reactor. Such an improvement in the reactor can lead to reducing 37% of the lamp output for a similar dosage [16]. Similarly, changes in the upstream hydraulics can also affect the dosage. 90 degree bends perpendicular and parallel to the reactor axis upstream of the reactor inlet are less efficient compared to the pipe straight to the inlet reactor [28]. Roughness of the wall produces effects not only on the hydraulics of the system but also on the dosage and RED values of the reactor. There is a drop in the velocity with an increase in the roughness value of the pipe. Compared

to the smooth pipe, a rough pipe increases the value of RED depending upon the Reynolds number of the flow. At lower Reynolds numbers, there is a higher percentage difference between the smooth and the rough surface [29].

The above methods rely on improving the system's geometry to achieve the required amount of dosage and in addition, achieved by using reactors in series. The theoretical evaluation of reactors in the series concludes that the dosage received by two identical reactors is twice the single reactor's dosage [30], [31]. Hence, for treating the microorganisms, which requires two times the RED value of a single reactor, can be treated using two reactors in series [32].

Open channel reactors have different challenges to the closed channel reactors in terms of hydraulics of the system. As open channel reactors are mainly for wastewater applications, UVT of the water is less than 70%. UVT has an exponential relationship with UV sensitivity; hence, the treatment of highly insensitive microbes does not improve with an increase in UVT. Thus, it is better to decrease the distance between the lamps to treat the microbes with higher sensitivity than to increase the UVT [33]. Like the closed channel reactor, roughness also affects the open channel reactor. However, these effects are negligible for higher Reynolds numbers. Analysing the open channel reactor requires a large amount of computational power. However, these simulations are more cost-effective than experiments. De featuring the geometry can simplify the model. A simple geometry consisting of channel and lamp provided very close results to a full-scale geometry consisting of all reactors' features. The use of this can decrease the complexity and cost of the simulation [14], [34]–[36].

#### 2.1.2 Effect of lamps

he arrangement of UV lamps within closed channel reactors fundamentally affects treatment performance. Reactors are classified as either parallel or perpendicular based on lamp orientation relative to the flow axis. The effects of lamp configuration interact complexly with hydraulic factors discussed in Section 2.1.1. Closed channel reactors classified as parallel and perpendicular reactors, based on the arrangement of the lamps [37]. A system with lamps perpendicular to the reactor axis is classified as perpendicular reactors while a system with lamps parallel to the axis of the reactor is classified as parallel reactor. The effects of different configuration are complex and dependent on several different other hydraulic factors. When compared to similar UV dose and a similar number of lamps, parallel lamp configuration

provided better log reduction compared to the perpendicular lamp configuration. These factors are highly sensitive, with small changes in location and configuration results in different dosage [38]. For example, a similar number of lamps and parallel configuration, but with two different orientation types, leads to different log reduction results. Lamps placed under the inlet-outlet have better log reduction compared to the evenly distributed lamps inside the reactor [27], [39]. The use of a genetic algorithm methodology can achieve arrangement optimisation. This algorithm finds the optimum location and arrangement of lamps inside the reactor for the highest minimum value of RED. The calculation for the optimum lamp circle uses the following formula:  $\frac{D_c}{2} \pm 20 \ units$ . Where D<sub>c</sub> is the diameter of the reactor. In addition, the asymmetric lamp arrangement shows better results than symmetric arrangement in terms of dosage received by the microorganism. Research shows that asymmetric arrangement improves RED value by 15%. The relationship between the lamp arrangement and RED is quite complex, hence the use of genetic algorithm methodology to find the optimum arrangement inside the reactor [40], [41]. Turning off lamps one by one, can establish the importance of each lamp. Turning off the lamps without removing them from the reactor to maintain similar hydraulics and flow pattern inside the reactor. Using this technique, it is found that the lamps closer to the main flow are more effective than the lamps away from the main flow for the overall dosage received by the reactor [42].

A single lamp with equivalent power to six lamps performs better than six lamps. The reason for this is because of the higher power and the barrier effect. Increasing the flow rate due to the hydraulic pressure can minimise the barrier effect. There is the use of multi reactors in industrial scale for large cross-sections. Similarly, research indicates that the single lamp reactor's energy distribution is better than the double lamp reactor, while the volume emission rate is similar. However, two lamps have better irradiation near the walls compared to the single lamp [27], [43].

Using an online monitoring system can optimize UV dose delivery by adjusting lamp power output based on real-time conditions. The system monitors lamp output, attenuation coefficient, UV transmission, and quartz sleeve fouling coefficient. The data collected from this could help in improving the efficiency of the system in real-time by changing the power of the lamps. In addition, it determines the accidental breaking of lamps inside the water or

cleaning required inside the reactor. The increase in the lamp power increases the dosage received by the microorganisms [15], [44].

Open reactors are again subdivided into two types based on the configuration of the lamps arrangement inside the open channel reactor: 1) horizontal configuration and 2) Vertical configuration. The horizontal configuration is advantageous over vertical configuration in terms of residence time for the microorganism. This is because the flow of water is along with the lamps [14]. However, the research presents contradictory results that the vertical lamp configuration performed better than the horizontal lamp configuration. In addition, staggered lamp positioning is better than parallel lamp positioning in terms of RED value received by the water. The differences in the value of the RED for vertical and horizontal configuration is more at lower Reynolds numbers [34].

#### 2.1.3 Effect of Temperature

There is no temperature effect on treating the water or on the hydraulics of the system if there is a continuous flow of water with small variation in the inlet temperature [42]. However, if there is a significant increase in the water temperature, then relative UV intensity increases from 0.53 at 4.7-degree Celsius until approximately 32 degree Celsius to 1.26 after that temperature decreases. This could have a significant impact if the temperature of the inlet water varies widely during different seasons. The use of other factors such as varying flow rate inside the reactor can offset the effect of the temperature [44]. However, if there is a significant increase in the water temperature, then relative UV intensity increases from 0.53 at 4.7°C to 1.26 at approximately 32°C, after which temperature decreases reduce intensity. [42].

#### 2.1.4 Effect of UVT

Drinking water applications have UVT higher than 70% while wastewater application usually has UVT less than 70%. Higher UVT of the water improves the dosage received by the microorganism because the fluence rate inside the reactor increases exponentially with an increase in UVT. Increase in UVT also leads to better energy distribution inside the reactor [15], [43]. Flow rate must be lower for lower UVT to allow higher residence time for the particle while, at higher UVT values, the flow rate is higher [45].

#### 2.1.5 Effect of flow rate

The flow rate is an essential parameter while considering the hydraulics of the reactor. Ideally, if a reactor can treat all the water that flows in it, then the flow rate should be as high as possible to obtain maximum efficiency out of the system. However, due to the limitations of the reactors, it is not possible to attain this. Hence, it is very important to determine the ideal flow rate for each system. It is not possible to carry out experiments for every change in flow rate. Hence, CFD is a vital tool in determining the flow rate of the system. Current systems use different flow rates ranging from as low as 1 m³/h up to as high as 552 m³/h. Low flow rates are generally used for laboratory-scale experiments where the models are scaled. Industrial-scale models use higher flow rates. Published research indicates the considerable amount of laboratory-scale model tests carried out. However, for the industrial-scale models, such information is scarce.

Higher Reynolds numbers decrease the RED value, which is because there is less residence time for the particle. At low Reynolds numbers, flow approaches laminar flow; this leads to too little to no mixing of flow inside the reactor. At low Reynolds numbers, (usually corresponds to a low flow rate) the flow is laminar. At such a low flow rate, there is little mixing of the flow. This leads to an inefficient system, as the UV dose is not uniformly distributed. At higher Reynolds numbers there is proper mixing because of the swirl caused inside the reactor. This leads to a better mixing of water [26]. CFD used to determine the ideal flow rate for each reactor. Each reactor because of its uniqueness provides a different ideal flow rate to the system [16]. Water profile plays an important role, including the determination of the dosage inside the reactor. With changes in the internal reactor profile, there are changes in the water profile. This, in turn, affects the path of the microorganism. Due to such effect, the flow velocity is higher with lower turbulent velocity in the parallel reactor compared to the vertical reactor.

The significant effect of hydraulics as well as the models used for the determination of the dosage it has become apparent that it is essential to understand both the assumptions and the limitations of the model. The method employed by researchers for the determination of the optimum flow rates for the given reactor is to initially find the optimum configuration using a constant flow rate and then using this optimum configuration to find the optimum flow rate [40]. Table 2.2 summarises all the effects on the UV systems.

| Parameter       | Configuration/Range  | Effect on   | Key Finding        | References      |
|-----------------|----------------------|-------------|--------------------|-----------------|
|                 |                      | RED         |                    |                 |
| Geometry        |                      |             |                    |                 |
| Closed channel  | L-type inlet/outlet  | +15% vs     | Perpendicular      | [29], [32],     |
|                 |                      | linear      | inlet enhances     | [34], [41],     |
|                 |                      |             | mixing             | [42], [45]      |
| Open channel    | Baffled vs unbaffled | +20% with   | Baffles increase   | [14], [34],     |
|                 |                      | baffles     | residence time     | [35], [44],     |
|                 |                      |             |                    | [46], [47]      |
| Lamps           |                      |             |                    |                 |
| Power           | Single high-power    | +10% vs     | Reduces            | [6], [7], [48], |
| distribution    |                      | multiple    | shadowing effects  | [49], [50]      |
| Arrangement     | Asymmetric           | +15% vs     | Better coverage of | [19], [21],     |
|                 |                      | symmetric   | flow field         | [51]–[54]       |
| Flow Rate       |                      |             |                    |                 |
| Low Re (<2,300) | Laminar flow         | -30% vs     | Poor mixing        | [13], [34],     |
|                 |                      | turbulent   | reduces efficiency | [40], [55],     |
|                 |                      |             |                    | [56]            |
| High Re         | Turbulent flow       | Optimal at  | Balance of mixing  | [11], [22],     |
| (>10,000)       |                      | Re~50,000   | and residence      | [31], [49],     |
|                 |                      |             | time               | [57]–[60],      |
|                 |                      |             |                    | [61]            |
| Temperature     | 4.7-32°C             | Minimal     | Minimal impact in  | [15],[23]       |
|                 |                      | impact      | normal range       |                 |
| UVT             | 70-98%               | Exponential | 2× dosage per      | [8], [15],      |
|                 |                      | increase    | 10% UVT increase   | [22], [28],     |
|                 |                      |             |                    | [43], [62]      |

# 2.2. Modelling of UV treatment System

The UV modelling includes two sections:

- 1. Modelling of the flow inside the reactor (Computational Fluid Dynamics CFD).
- 2. Modelling of the UV dose rate inside the reactor.

The two different methodologies usually adopted for modelling include Simultaneous UV dose rate and Fluid dynamics (SURF) and Three-step UV dose rate and Fluid dynamics (TURF) [27], [39].

The SURF method is an integrated approach that incorporates the simultaneous calculation of the fluid dynamics (flow) and the UV dose rate. This is typically achieved by defining the UV dose rate within the flow solver (CFD software) using a User-Defined Function (UDF). This allows the local flow conditions and velocity field to instantaneously influence the calculated UV radiation field as the simulation runs.

In contrast, the TURF method is a segregated or three-step approach:

- 1. Step 1: Calculate the steady-state flow field (velocities, turbulence) using a fluid dynamics model (CFD).
- 2. Step 2: Calculate the steady-state UV dose rate field based on the reactor geometry and water quality (UVT), independent of the flow field initially.
- 3. Step 3: Use the flow field results (streamlines or particle paths) from Step 1 and the fluence rate field from Step 2 to compute the Reduction Equivalent Dose (RED) received by water particles along their paths.

The key difference is that SURF calculates the UV dose simultaneously with the flow, allowing for potential coupling effects (like local temperature changes affecting both flow and UV output) if specified, whereas TURF carries out separate, uncoupled calculations for the flow and the UV dose field, and combines them in a third post-processing step [63]. This distinction can impact the computational cost and the level of detail regarding transient flow-radiation interaction.

In addition, another method involves calculating the flow field and UV dose rate simultaneously using a UDF within the CFD solver, but the final dosage calculation is carried out separately during post-processing using a specific custom code [14].

#### 2.2.1. Modelling of flow (CFD)

Computational fluid dynamics provides the foundation for understanding water movement and mixing patterns within UV reactors. The flow field directly influences pathogen trajectories, residence time distributions, and ultimately the UV dose delivered to microorganisms. Accurate flow modeling requires careful consideration of mesh resolution, turbulence models, and boundary conditions to capture the complex hydraulic phenomena including recirculation zones, dead spaces, and lamp-induced flow disruptions. The following sections examine key considerations from the literature for developing reliable CFD models of UV reactors.

#### 2.2.1.1 Mesh

Literature reports varying mesh requirements for UV reactor simulations, ranging from 0.5 million cells for simple geometries to over 2 million cells for complex multi-lamp configurations [14], [27], [39], [45]. Liu et al. demonstrated that for a single-lamp reactor (100mm diameter, 1m length), mesh independence was achieved at 1.2 million cells, with less than 2% deviation in predicted dose distribution beyond this threshold. For particle tracking studies, convergence typically occurs between 5,000-10,000 particles, with residence time distributions stabilizing above this range [16], [35], [42], [64], [65].

Lagrangian particle tracking employs micro-particles (10<sup>-6</sup> m diameter) to simulate pathogen trajectories through the reactor. Bolton et al. [8] showed that particle diameter variations between 10<sup>-7</sup> and 10<sup>-5</sup> m produced negligible differences in calculated dose distributions, confirming that Brownian motion effects are minimal at reactor-scale Reynolds numbers [2], [14], [16], [27], [34], [35], [39], [40], [42], [43], [45], [62], [66]–[69].

#### 2.2.1.2. Model settings

Reactor configuration determines modeling complexity. Closed conduit reactors require single-phase flow models, while open channel systems necessitate volume-of-fluid (VOF) or similar multiphase approaches to capture the free surface. When comparing single-phase and VOF modeling approaches for open channel reactors, they found that transient water level variations resulted in UV dose fluctuations of up to 15% [20], [70].

#### 2.2.1.3 Boundary settings

Standard boundary implementations include velocity or mass flow rate specifications at inlets with 2-3% turbulence intensity for municipal water systems. Wols et al. [10] demonstrated that inlet turbulence intensity variations between 1-5% produced less than 3% change in reactor dose distribution for Re > 10,000. Outlet conditions typically employ zero gauge pressure, while walls utilize no-slip conditions [14], [45].

#### 2.2.1.4 Turbulence model

Comprehensive turbulence model comparisons for UV reactors reveal performance variations based on flow characteristics. Liu et al. evaluated six turbulence models against PIV data in a single-lamp reactor [22]:

- 1. Standard k-ε: Accurate in bulk flow (±5% velocity deviation) but underpredicted near-wall velocities by 15-20%
- 2.  $k-\omega$  SST: Superior wake prediction behind lamps ( $\pm 8\%$  accuracy) and better near-wall treatment
- Reynolds Stress Model (RSM): Best overall performance (±5% throughout domain) but
   3-4 times higher computational cost
- 4. Large Eddy Simulation (LES): Required for baffle-induced unsteady flows, capturing vortex shedding missed by RANS models [24]

The judgement for this comparison uses the experimental data from a PIV experiment. Because of the different flow pattern, there is a turbulence model effect on the UV dose distribution. The difference highlighted in terms of the dominant peak and secondary peak of the dose distribution. There is both dominant and secondary peak in std k- $\epsilon$ , realisable k- $\epsilon$ , k- $\omega$ , RNG and TFM. In the RTSM model, there is no secondary peak, because of better flow near the wall region. k- $\omega$  has neither a dominant nor a secondary peak and observes a wider spread of the UV dose distribution. The Reynold stress model provides similar results for velocity and dosages but more significant variation in the turbulent kinetic energy [71]. Additionally, comparison carried out for the k- $\epsilon$  model, RNG k- $\epsilon$  model and Reynold stress model. The k- $\epsilon$  model considered adequate, as there is a slight difference in the value of velocity and dosages. The k- $\epsilon$  model is 3-4 times cheaper compared to the Reynold stress model [26]. However, k- $\epsilon$ 

model fails to accurately predict the disinfection model for certain geometry such as introduction of baffle upstream of the flow. Higher turbulence model such as LES are required to correctly calculate the wakes created because of the obstruction in the flow [36]. There is an effect on the mass transfer rate because of the flow in certain UV processes like Advanced Oxidation Process (AOP). However, those effects are not studied for the UV treatment of drinking water application [12], [72], [73].

#### 2.2.2 UV modelling (UV dose)

The UV modelling helps to determine the fluence rate inside the reactor. The UV modelling carried out either through user-defined function in CFD or through separate modelling using software like MATLAB. There is different type of models used for modelling the fluence distribution inside the reactor. Most commonly used models are MPSS (Multi point source summation model) and MSSS models (Multi segment source summation model).

#### 2.2.2.1 MPSS (Multi point source summation model) model

The MPSS model used to simulate the fluence rate field inside the reactor. The MPSS model considers each lamp as a collection of light-emitting point sources of equal power. Considers the light emitted is in an axial direction. Each point receives a fluence rate equalling to the total fluence rate received from each point source. The calculated light beam laws use Snell's law and Fresnel's law. The calculation for the absorption law uses the Beer-Lambert's law [27], [39].

#### 2.2.2.2 MSSS (Multi segment source summation model)

The MSSS model is like the MPSS model in terms of refraction reflection and adsorption; however, it considers the lamp as a cylindrical source. The light intensity decreases with the cosine angle between the unit normal vector and the directional vector. The MSSS model is computationally expensive compared to other models [27], [39]. Table 2-1 summarises the type of modelling software used to calculate the dosage data for the UV treatment system and the fluid data such as the turbulence model used.

Table 2-1: Fluid flow vs Turbulence model vs UV dose modelling

| Fluid flow   | Turbulence | UV dose         | References                          |
|--------------|------------|-----------------|-------------------------------------|
| modelling    | model      | modelling       |                                     |
| software     |            |                 |                                     |
| Ansys Fluent | k-ε        | Calc3D          | [40], [41]                          |
|              |            | Integrated      | [29], [43], [45], [66], [70], [74], |
|              |            | model in fluent | [75]                                |
|              |            | User defined    | [14], [15], [42], [69]              |
|              |            | functions in    |                                     |
|              |            | fluent          |                                     |
|              |            | MATLAB          | [27], [39]                          |
| Ansys CFX    | k-ω SST    | Calc3D          | [35]                                |
| COMSOL       | k-ε        | Not mentioned   | [12], [16], [36]                    |
|              | Large eddy |                 | [36]                                |
|              | simulation |                 |                                     |
|              | (LES)      |                 |                                     |
|              | Not given  |                 | [8], [22], [60]                     |
| COMET        | k-ε        |                 | [47]                                |
| PHOENICS     |            |                 | [28], [71], [76]                    |
| Finlab       |            |                 | [9]                                 |

### 2.3. Summary

This literature review has examined UV water disinfection technology, computational modeling approaches, and experimental validation methodologies, revealing critical gaps that limit commercial-scale UV LED reactor development.

#### **Key Findings:**

UV LED technology offers significant advantages over mercury lamps (instant operation, compact design, environmental safety, wavelength tunability) but faces challenges in achieving cost-competitiveness due to lower UV output per device. Peripheral LED placement

enables fundamentally different reactor designs compared to mercury lamp systems, particularly swirl-enhanced flow structures for improved mixing.

CFD modeling with RANS turbulence models (k- $\epsilon$ , SST k- $\omega$ ) has become essential for reactor design, with SST models demonstrating superior accuracy for swirling flows. Integration with optical ray-tracing models enables comprehensive performance prediction, though LED systems require more sophisticated optical models than mercury lamps. Biodosimetry validation using MS2 bacteriophage provides definitive performance verification [77], [78].

#### **Critical Research Gaps:**

Despite extensive UV reactor research, several gaps impede LED reactor development:

- Scale gap: Existing LED reactor studies focus on small systems (<10 L/h), while commercial applications require 80-250 m³/h—a 100-1000× capacity increase. No validated models exist at commercial scale.
- Swirl characterization: No systematic investigation of engineered swirl effects on UV dose distribution exists. Optimal swirl intensity, generation methods, and geometric parameters remain undefined.
- Experimental validation: PIV studies limited to small mercury lamp reactors (DN50-DN100, Re < 50,000). No detailed velocity measurements exist for LED reactors at commercial Reynolds numbers (Re = 100,000-500,000).</li>
- Geometric effects: Systematic quantification of upstream configuration, scaling, and LED arrangement effects on performance is absent, preventing installation flexibility assessment.
- Design guidelines: Practical guidance for commercial implementation (component selection, installation requirements, scaling rules) is unavailable.

This thesis addresses these gaps through comprehensive CFD modeling validated by dual experimental approaches (biodosimetry and PIV), systematic geometric analysis, and development of quantitative design guidelines for commercial UV LED reactor optimization.

## Chapter 3. Research Methodology

This chapter presents the comprehensive methodology developed for investigating flow dynamics and UV dose distribution in LED-based water treatment systems. The research employs an integrated approach combining computational fluid dynamics (CFD) modelling, optical radiation modelling, and experimental validation through Particle Image Velocimetry (PIV) measurements.

## 3.1. Computational Fluid Dynamics

Computational Fluid Dynamics (CFD) is a powerful analytical tool that uses numerical methods and algorithms to study fluid flows. While experimental studies provide valuable data, they can be expensive and limited in scope, particularly for complex geometries and fluid interactions. CFD offers a practical alternative by enabling detailed flow simulations through computer modelling. This approach is especially valuable for studying velocity profiles and flow components where physical experiments would require sophisticated and expensive measurement techniques. With advancing technology and refined computational models in established software packages, CFD allows comprehensive analysis of fluid behaviour that might be impractical to study experimentally. This enables study of optimisation of the system through detailed understanding of the flow while managing the research costs [26], [79].

The following methodology is applied while developing the CFD model:

- Spatial Discretisation: Creating a mesh made up of discrete control volumes or cells which defines the solution domain.
- Equation Discretisation: Converting the continuous fluid flow equations into algebraic equations to get the approximate solution for flow properties.
- Time Integration: Implementation of the numerical schemes for time-dependent problems. However, for steady state solutions these governing equations are not taken into account.

#### 3.1.1. Ansys CFX

ANSYS CFX is used in this study to solve the fluid flow equations. ANSYS CFX is a finite volume-based computational fluid dynamics solver that employs cell vertex discretisation

methodology. The software can simulate both laminar and turbulent flows across various mesh types including hexahedral, tetrahedral, prism, and pyramid elements in structured, unstructured, or hybrid configurations. CFX's automatic mesh interface handling and adaptive refinement capabilities enable accurate flow solutions. For in-depth technical understanding of mathematical models and solution techniques, users can refer to the ANSYS CFX solver theory guide [80].

#### **Governing equation**

There are three fundamental equations in the fluid dynamics.

1) Conservation of Mass

$$\frac{\partial \rho}{\partial t} + \nabla(\rho V) = 0 \tag{1}$$

Where  $\rho$  is the density of the fluid, t is time and V is the velocity vector

2) Conservation of Momentum expressed as Navier stokes Equation:

$$\frac{\partial(\rho V)}{\partial t} + \rho(V.\nabla)V = -\nabla p + \nabla.\tau_{ij} + \rho g \tag{2}$$

Where p is static pressure,  $\tau_{ij}$  is stress tensor,

For incompressible Newtonian fluid such as water the momentum equation simplifies in terms of stress tensor. Moreover, the equation further simplifies for the steady state as

$$\partial(\rho V)/\partial t = 0 \tag{3}$$

3) The final equation is regarding the conservation of energy which is only required if there is heat transfer or compressibility.

#### 3.1.2. Geometrical model

UV LED water treatment systems are generally categorised into two primary configurations based on LED positioning: internal and external mounting systems [66]. This research focuses on external LED configuration systems, where LEDs are positioned around the reactor periphery rather than within the water flow path. This configuration offers several operational advantages that make it particularly suitable for commercial-scale water treatment applications. The external LED mounting configuration provides significant operational benefits over internal lamp systems:

- Fouling Prevention: Unlike conventional mercury-based systems where lamps are submerged within the water stream, external LED placement eliminates direct contact with the treatment medium. This design inherently prevents biofilm formation and mineral deposition on optical surfaces, which commonly necessitate frequent maintenance intervals in traditional UV systems [81].
- Maintenance Accessibility: The external configuration facilitates straightforward LED replacement and maintenance procedures without requiring system drainage or flow interruption. This accessibility is particularly crucial given the finite operational lifespan of LED components and the need for periodic replacement to maintain treatment efficacy [57].
- Hydraulic Independence: By positioning LEDs outside the flow path, the system
  maintains unobstructed hydraulic conditions within the reactor. This separation
  allows for independent optimization of flow dynamics and optical delivery, providing
  enhanced control over mixing patterns and residence time distributions without
  interference from lamp fixtures or support structures [35].

#### **BIO310 Reactor System Components**

The BIO310 UV LED water treatment plant as shown in the Figure 3-1 developed by Typhon Treatment Systems Ltd shows the commercial-scale external LED reactor design [21]. The system architecture comprises five integrated modules, each serving specific functional requirements:

- **1. Inlet Connection Module** The inlet section provides hydraulic interface with existing municipal water infrastructure. Adaptable reducer fittings accommodate varying pipe diameters, ensuring compatibility with diverse installation requirements while maintaining optimal inlet flow conditions.
- **2.** Thermal Management Module The heat exchanger system addresses the substantial thermal load generated by high-intensity LED arrays. Efficient heat dissipation is critical for maintaining LED output efficiency and extending operational lifespan, as LED performance exhibits strong inverse correlation with junction temperature.
- **3. Flow Conditioning Module** The flow conditioning system incorporates two hydraulic elements:
  - **Static guide vanes:** Eight radially-distributed vanes oriented at predetermined angles to impart rotational momentum
  - 90° elbow: Reinforces tangential velocity components introduced by the guide vanes

This dual-component configuration generates controlled swirl flow, promoting cross-sectional mixing and enhancing radial distribution of water parcels throughout the irradiation zone. The induced secondary flow patterns are fundamental to achieving uniform UV dose distribution.

- **4. Irradiation Chamber** The reactor core houses 1000 UV LEDs arranged in 50 circumferential rings along the reactor length. LEDs are mounted externally to a quartz sleeve that maintains hydraulic isolation while providing high UV transmittance.
- **5. Outlet Configuration** The outlet section provides transition from the treatment zone to downstream distribution infrastructure, incorporating appropriate fittings for system integration while minimizing pressure losses and maintaining treated water quality.

A) B)



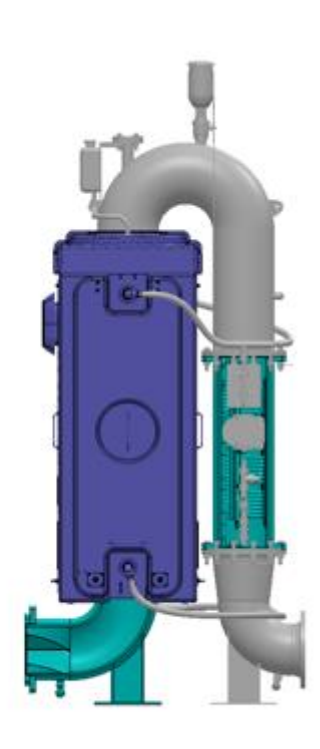


Figure 3-1:A) Full scale water treatment plan in the Typhon Lab b) SolidWorks model version of full-scale water treatment plant

#### 3.1.3. Geometrical Assumptions and Simplification

To achieve computational feasibility within realistic timeframes while maintaining the required accuracy, the complex commercial geometry of the UV LED reactor required several justified geometrical simplifications. These assumptions were made based on preliminary analysis, physical reasoning, and best practices in Computational Fluid Dynamics (CFD).

#### **Heat Exchanger Module**

The UV LED system, includes a heat exchanger module designed to cool the LED units and maintain optimal performance. The full assembly of the commercial prototype (BIO310) positions the heat exchanger coil downstream of the reactor module.

To manage model complexity and computational time, the heat exchanger coil itself was omitted from the main fluid domain model used for the primary CFD analysis. This omission was justified because preliminary testing indicated that the coil had a negligible effect on the

overall flow dynamics and UV dose distribution within the reactor, causing less than a deviation in key dosage values.

Furthermore, for the modeling of the heat exchanger components when included in secondary analyses or flow models for validation, the following assumptions were made:

- All significant flow diameters in the heat exchanger were assumed to be of the external diameter of the heat exchanger pipe.
- Small, intricate changes in diameter and minor structural details within the heat exchanger were ignored in the CAD preparation.

# **General Simplifications**

Beyond the heat exchanger, additional simplifications were applied to the CAD model (developed in SolidWorks 2020) to focus the computational effort on the critical flow mixing regions:

- Bellows and Flanges: The geometric details of all industrial connecting components, such as flanges and bellows (which connect the quartz tube to the pipe system), were simplified or omitted. These components were deemed to have minor influence on the developed turbulent flow and secondary flow structures deep within the fluid domain.
- Static Vane: The stationary guide vanes upstream of the reactor were modeled based on the patented design specifications. Minor features such as mounting brackets, weld fillets, and edge chamfers were omitted as these small-scale features do not significantly influence the bulk flow characteristics while substantially increasing mesh requirements.
- LED Housings: Since the fluid domain only models the water volume, the external
  casings and detailed LED housing geometry surrounding the reactor were excluded.
   The influence of the LEDs is accounted for separately in the optical model.
- Internal Fasteners: All small features like nuts, bolts, or minor internal supports were removed to create a cleaner, continuous fluid domain, thereby reducing the cell count necessary for meshing.

Validation Model Adaption: When developing the CFD model specifically for PIV validation (as detailed in Chapter 6), the geometry was scaled and modified to precisely match the experimental rig dimensions (e.g., pipe diameter) and component arrangements, ensuring geometric similarity for direct comparison.

#### 3.1.4. Mathematical Model

ANSYS 2019 R3 version is used for developing the model and analysing the mathematical model. The geometrical features of the model are developed within SolidWorks 2020. The geometry is then imported in Ansys DesignModeler and meshed using ANSYS mesher. Key assumptions were made regarding the underlying physics and numerical methods to develop a practical CFD model. This section provides the rationale for each modelling choice, whether related to simplifying the physics or choosing suitable numerical approximations. By outlining the assumptions and discretisations underpinning the CFD model, this section aims to demonstrate the balanced approach of retaining critical physics while efficiently resolving the key fluid dynamics within the UV reactor. The end result is a validated modelling methodology capable of providing meaningful performance insights despite necessary approximations.

# 3.1.4.1. Turbulence Model

The Shear Stress Transport (SST) model is a turbulence model used in Computational Fluid Dynamics (CFD) simulations to accurately predict the behaviour of turbulent flows. The SST model combines two distinct turbulence models, the k- $\epsilon$  and k- $\omega$  models, in order to capture different aspects of the turbulence physics [35]. The k- $\epsilon$  model is employed near the walls where the flow is close to being fully turbulent. It focuses on the turbulent kinetic energy (k) and its dissipation rate ( $\epsilon$ ), considering the turbulent eddies' interaction with the mean flow and the wall boundary layer. This region is often referred to as the viscous sublayer. As the flow moves away from the walls, where the flow becomes freer and more separated, the k- $\omega$  model takes over. It concentrates on the turbulent intensity ( $\omega$ ) and its specific dissipation rate ( $\beta$ ). The k- $\omega$  model is particularly effective in capturing the flow separation and reattachment regions, where the flow changes direction or encounters significant disturbances. Hence, SST model is able to combine properties of both turbulence models to effectively simulate the flow conditions in the reactor [80] [82].

#### 3.1.4.2. Domain geometry

The complete geometry constructed in SolidWorks is imported into ANSYS DesignModeler for computational domain preparation. As illustrated in Figure 3.2, the computational domain encompasses all critical flow components including the inlet section, outlet section, stationary swirl vanes, pipe walls, and heat exchanger coils. The flow enters through the inlet located at the bottom left of the assembly and exits through the outlet positioned at the top right, as depicted in Figure 3.2. The stationary vanes and heat exchanger coils are clearly visible in the geometric representation.

Within DesignModeler, named selections are systematically applied to each geometric component to facilitate accurate boundary condition specification during the CFD setup phase. Descriptive nomenclature is assigned to each component (e.g., "inlet\_surface," "outlet\_surface," "vane\_walls," "pipe\_walls," "heat\_exchanger\_coils"), ensuring unambiguous identification when defining boundary conditions, material properties, and solver settings in subsequent preprocessing stages. This systematic naming convention enhances model organization, reduces setup errors, and enables efficient modification of boundary conditions during parametric studies.

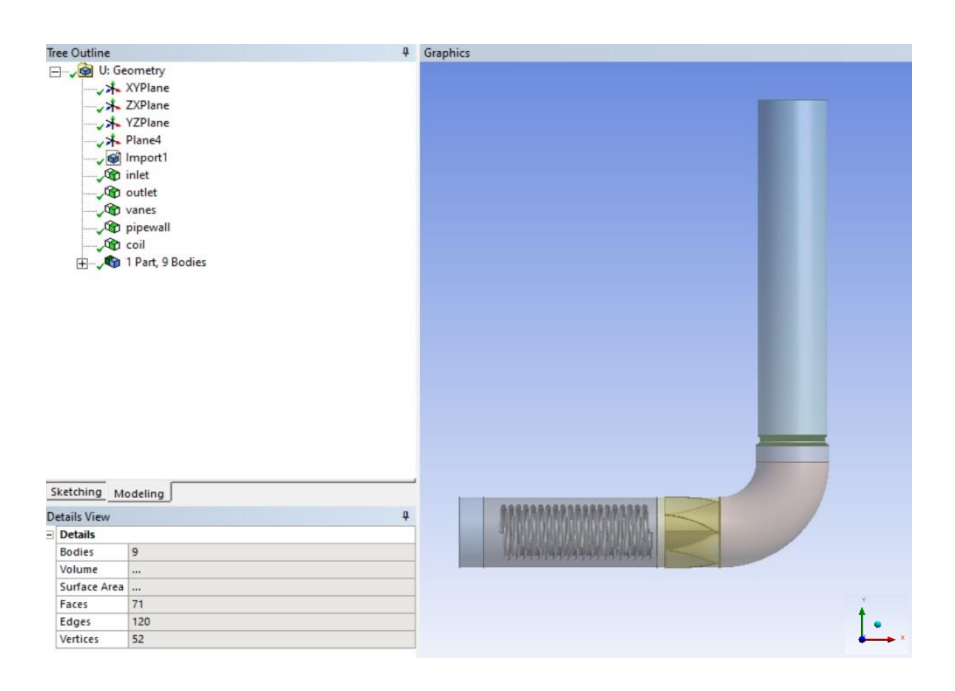


Figure 3-2: Full-scale domain geometry in Ansys DesignModeler

#### 3.1.4.3. Mesh

The computational mesh was generated using a hybrid approach combining structured and unstructured elements to optimize accuracy and computational efficiency. Two distinct meshing strategies were applied based on geometric complexity: tetrahedral elements for complex regions and hexahedral elements for simpler pipe sections.

#### Mesh Strategy

Sections containing the heat exchanger coils and stationary vanes were meshed using tetrahedral elements due to their geometric complexity. These unstructured elements provide flexibility in capturing intricate geometric features without excessive manual intervention. The remaining pipe sections, characterized by simpler cylindrical geometry, were meshed using the sweep methodology to generate structured hexahedral elements. This approach produces high-quality aligned elements in regions of relatively uniform flow, reducing numerical diffusion and improving solution accuracy.

## **Boundary Layer Resolution**

Inflation layers were applied to all wall boundaries throughout the computational domain to accurately resolve the boundary layer. These prismatic layers transition from the wall surface into the core flow region, providing high mesh density where velocity gradients are steepest. The inflation layer strategy ensures accurate prediction of near-wall flow phenomena including flow separation, reattachment, and transitional effects. This refinement is particularly critical in regions near the stationary vanes and elbow where flow behaviour is complex and strongly influenced by wall interactions. The boundary layer mesh captures the velocity gradients and turbulence effects essential for accurate prediction of flow behaviour.

#### **Local Mesh Refinement**

Localized mesh control was implemented using face sizing and edge sizing methods to ensure adequate resolution in critical flow regions. The reactor region, where UV dose calculations are performed, was discretized with a particularly dense mesh. This finer resolution enables the generation of accurate streamlines, which are essential for precise calculation of UV dose distribution within the reactor.

#### **Mesh Quality and Statistics**

The final computational mesh contains 4.3 million elements and 1.4 million nodes. Mesh quality was assessed using standard metrics to ensure solution accuracy and stability. Table 3-1 summarizes the mesh settings and quality parameters.

Table 3-1: Mesh quality and statistics

| Setting/Value                  |
|--------------------------------|
| 4,300,000                      |
| 1,400,000                      |
|                                |
| Tetrahedral                    |
| Hexahedral (sweep method)      |
| Prismatic (inflation layers)   |
|                                |
| 10                             |
| 0.1                            |
| 1.2                            |
|                                |
| Dense                          |
| Refined using face/edge sizing |
|                                |
| > 0.1                          |
| < 0.9                          |
|                                |

The high orthogonal quality (> 0.1) maintained throughout the mesh ensures numerical stability and solution accuracy. The combination of structured hexahedral elements in uniform regions and unstructured tetrahedral elements in complex zones provides an optimal balance between computational efficiency and geometric fidelity. Figure 3-3 shows the mesh applied to the geometry.

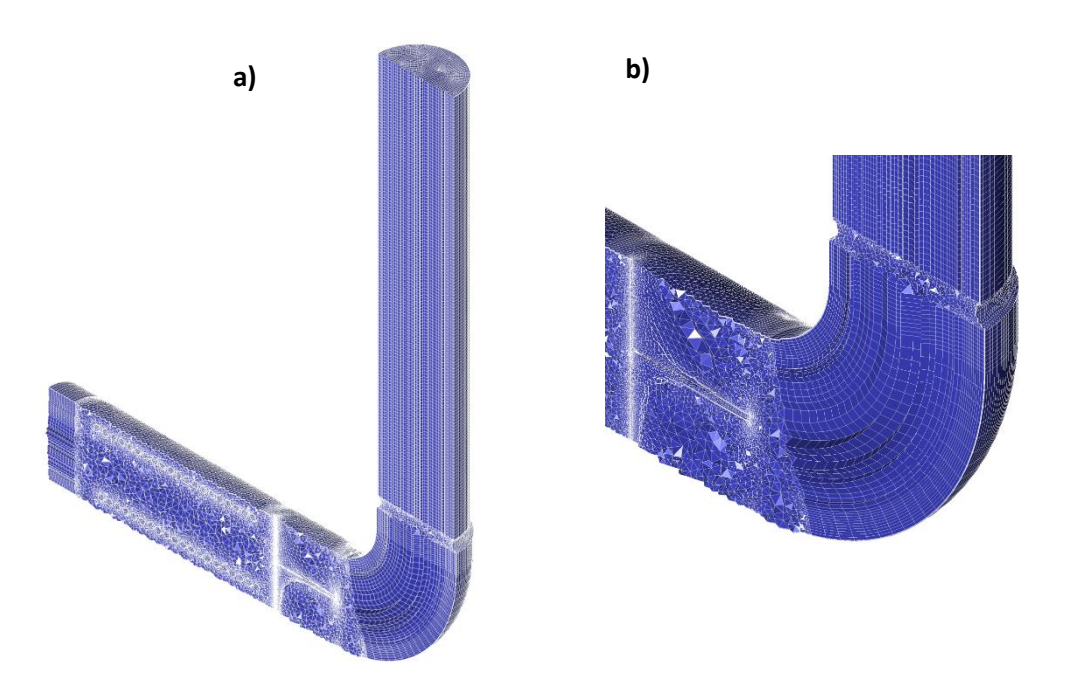


Figure 3-3: a): Identifying mesh in the entire geometry. Figure 3b): Mesh showing inflation layer

#### 3.1.4.4. Model settings

The following sections detail the physics definitions, domain properties, boundary conditions, and solver settings implemented in ANSYS CFX. These settings are based on established best practices in CFD modeling of water treatment systems and validated approaches from published literature.

## **Physics Definition**

The physics for the model were configured in the CFX-Pre module following the mesh import from ANSYS Meshing. Named selections created in DesignModeler were utilized to systematically define boundary conditions, ensuring consistent identification of geometric features throughout the setup process. This approach follows the standard workflow recommended for complex multi-component geometries in ANSYS CFX and has been successfully employed in similar water treatment reactor studies

#### **Domain Properties**

The domain properties define the fundamental physical characteristics of the fluid and the simulation framework. Table 3-2 presents the domain property settings for the full-scale reactor model.

Table 3-2: Domain properties and material definition

| Property              | Setting                         | Justification   |
|-----------------------|---------------------------------|---|
| Material              | Water at 25°C                   | Standard drinking water temperature; density: 998 kg/m³, dynamic viscosity: 0.001003 Pa·s                     |
| Morphology            | Continuous Fluid                | Single-phase incompressible flow typical of water treatment systems   |
| Reference<br>pressure | 1 atm (101,325 Pa)              | Atmospheric reference for gauge pressure calculations   |
| Buoyancy<br>model     | Non-buoyant                     | Temperature variations negligible; buoyancy effects not significant in forced convection flows                |
| Domain<br>motion      | Stationary                      | Fixed reactor geometry with no moving components  |
| Turbulence<br>model   | Shear Stress<br>Transport (SST) | Combines k- $\epsilon$ and k- $\omega$ advantages; proven accuracy for swirling flows and near-wall behaviour |
| Heat transfer         | None                            | Isothermal assumption justified by negligible temperature variations during continuous operation              |

The selection of water properties at 25°C represents typical drinking water treatment conditions. Studies have shown that temperature variations in the range of 15-30°C have minimal impact on reactor hydraulics and UV dose distribution for continuous flow systems. The Shear Stress Transport (SST) turbulence model was selected based on its superior performance in capturing both free-stream turbulence and near-wall flow phenomena, particularly important for swirling flows generated by the stationary vanes. The SST model has been extensively validated for UV reactor applications and demonstrates better prediction of secondary flows compared to standard k-ε models.

## **Boundary Conditions and Named Selections**

Boundary conditions define the interaction between the fluid domain and its surroundings. The named selections created in DesignModeler provide a systematic method for applying these conditions to specific geometric features. Table 3-3 combines the named selections with their corresponding boundary conditions and provides justification for each setting.

Table 3-3: Named selections, boundary conditions, and justification

| Named     | Description                             | Boundary | Boundary Details  | Justification  |
|-----------|---|----------|---|--|
| Selection |   | Туре     |   |  |
| Inlet     | Inlet face –<br>entry point<br>of water | Inlet    | Flow regime: Subsonic Mass and momentum: Normal   | Normal speed specification ensures flow perpendicular to inlet face. Turbulence intensity of 5% typical for developed pipe flow                      |
|           |   |          | Velocity magnitude: Variable (flow rate dependent) Turbulence: Intensity 5%, Length scale: 0.01 |  |
| Outlet    | Outlet face  – exit point of water      | Outlet   | Flow regime: Static Pressure: 0 bar   | Static pressure outlet allows flow to develop naturally without imposing velocity constraints. Zero- gauge pressure represents atmospheric discharge |
| Vanes     | Stationary<br>guide vane<br>surfaces    | Wall     | Mass and momentum: No-slip wall Wall roughness: Smooth wall                                     | No-slip condition mandatory for viscous flows. Smooth wall assumption justified for manufactured stainless   |

|          |                                   |      |   | steel vanes (roughness < 0.002 mm, negligible effect on flow)   |
|----------|-----------------------------------|------|---|---|
| Coil     | Heat exchanger coil surfaces      | Wall | Mass and momentum: No-slip wall Wall roughness: Smooth wall | Heat exchanger tubes assumed hydraulically smooth. Analysis shows minimal impact on reactor dosage (Chapter 4.3.1)                |
| Pipewall | Main pipe<br>and reactor<br>walls | Wall | Mass and momentum: No-slip wall Wall roughness: Smooth wall | Acrylic and quartz surfaces hydraulically smooth. Studies show wall roughness effects negligible at Re > 100,000 for smooth pipes |

## **Initial Conditions**

Initial conditions provide the starting point for the iterative solution process, influencing both convergence speed and stability. The domain was initialised with water at rest except for the primary flow direction, following established practices for internal flow simulations.

The velocity field was initialized as follows:

- Axial velocity (y-direction): Set to the inlet velocity corresponding to 100% flow rate
- Radial velocity (x-direction): 0 m/s
- Tangential velocity (z-direction): 0 m/s

The static pressure was initialized at 0 MPa (gauge), representing atmospheric reference conditions. This initialization strategy accelerates convergence by providing a reasonable first approximation of the flow field, reducing the number of iterations required to reach a converged solution.

## **Solver Control**

The solver control parameters govern the numerical solution strategy and convergence criteria. Table 3-4 summarizes the solver control settings.

Table 3-4: Solver control settings and justification

| Parameter        | Setting              | Justification  |  |  |  |  |
|------------------|----------------------|--|--|--|--|--|
| Simulation type  | Steady-state         | Flow conditions constant in time; steady-state appropriate for continuous operation. |  |  |  |  |
| Advection        | High                 | Blends 1st and 2nd order discretization; reduces                                     |  |  |  |  |
| scheme           | Resolution           | numerical diffusion while maintaining stability.                                     |  |  |  |  |
| Turbulence       | High                 | Consistent with advection scheme; improves accuracy                                  |  |  |  |  |
| numerics         | Resolution           | of turbulence transport.   |  |  |  |  |
| Timescale        | Automatic            | Adaptive timestep calculation improves convergence                                   |  |  |  |  |
| control          |                      | robustness.  |  |  |  |  |
| Length scale     | Conservative         | Prevents overly aggressive timesteps; ensures  |  |  |  |  |
| option           |                      | stability in complex geometries.   |  |  |  |  |
| Timescale factor | 1.0                  | Default value appropriate for well-conditioned problems                              |  |  |  |  |
| Maximum          | 10,000               | Sufficient for convergence; typical for complex                                      |  |  |  |  |
| iterations       |                      | reactor geometries.  |  |  |  |  |
| Residual target  | 1 × 10 <sup>-6</sup> | Stringent criterion ensuring high solution accuracy;                                 |  |  |  |  |
|                  |                      | consistent with literature.  |  |  |  |  |
| Convergence      | Either target        | Simulation terminates when iterations or residuals                                   |  |  |  |  |
| criterion        | met                  | satisfied  |  |  |  |  |

The steady-state simulation approach is appropriate for continuous-flow UV reactors operating under constant conditions, as demonstrated in numerous published studies. While transient effects may exist during startup or flow rate changes, the steady-state solution

represents the time-averaged behaviour relevant for performance prediction and design optimization.

The High-Resolution advection scheme was selected for both momentum and turbulence equations. This scheme employs a blend of first-order and second-order discretization, automatically adjusting the blend factor to maintain boundedness while minimizing numerical diffusion. This approach is particularly important for capturing swirling flows and secondary flow structures where excessive numerical diffusion can artificially dissipate rotational motion.

The convergence criterion combines both a maximum iteration limit (10,000 iterations) and a residual target ( $1 \times 10^{-6}$ ). The residual target of  $10^{-6}$  is significantly more stringent than the default value of  $10^{-4}$  and ensures high solution accuracy essential for subsequent UV dose calculations. In practice, all simulations in this study converged to the residual target well before reaching the iteration limit, typically achieving convergence within 3,000-5,000 iterations.

#### **Solver Definition**

The solver configuration determines the computational approach and hardware utilization. Table 3-5 presents the solver definition settings.

Table 3-5: Solver definition and computational resources

| Parameter            | Setting                              | Justification   |
|----------------------|--------------------------------------|---|
| Precision            | Double precision                     | Required for complex geometries and small residual targets; prevents round-off errors |
| Run mode             | Intel MPI Local Parallel             | Enables parallel processing for reduced solution time                                 |
| Number of partitions | 18                                   | Optimized for available CPU cores (10 physical cores, 20 threads)                     |
| Hardware             | Intel Core i9-7900X<br>CPU 64 GB RAM | Sufficient memory for 4.3M element mesh; typical solution time: ~3 hours              |

| Operating | Windows             | 10 | Available operating system |
|-----------|---------------------|----|----------------------------|
| system    | Professional 64-bit |    |                            |

Double precision arithmetic was employed for all simulations, as recommended for complex flow problems with stringent convergence criteria. Double precision calculations use 64-bit floating-point numbers, providing approximately 16 decimal digits of accuracy compared to 7-8 digits for single precision. This additional precision is essential when solving for small differences in pressure and velocity that characterize swirling flows and when targeting residuals of  $10^{-6}$  [80].

The parallel processing capability was utilized through Intel MPI (Message Passing Interface) with domain decomposition across 18 partitions. While the CPU features 10 physical cores with hyperthreading (20 logical cores), benchmarking indicated optimal performance at 18 partitions, balancing computational load with communication overhead.

The computational resources (64 GB RAM) were sufficient to accommodate the 4.3 million element mesh with adequate margin, with typical memory usage during solution of approximately 45 GB. Solution time of approximately 3 hours for convergence to 10<sup>-6</sup> residuals was acceptable for the parametric studies conducted in this research.

# *3.1.4.5. Post-Processing*

Post-processing in ANSYS CFX-Post was conducted to extract quantitative flow data and generate visualizations for analysis. The post-processing strategy was designed to support two primary objectives:

- Characterization of flow hydrodynamics within the reactor
- Generation of streamline data for subsequent UV dose calculations.

This dual-purpose approach enables comprehensive evaluation of both hydraulic performance and disinfection efficiency.

#### **Streamline Generation for UV dose Analysis**

Streamlines were generated to track water particle trajectories through the reactor, providing the foundation for UV dose calculations. The streamline seeding strategy employed concentric circular patterns positioned on a plane at the reactor inlet, as illustrated in Figure

3-4. This structured seeding approach ensures uniform spatial coverage across the reactor cross-section and provides adequate resolution to capture the swirling flow behaviour induced by the upstream stationary vanes and elbow [83].

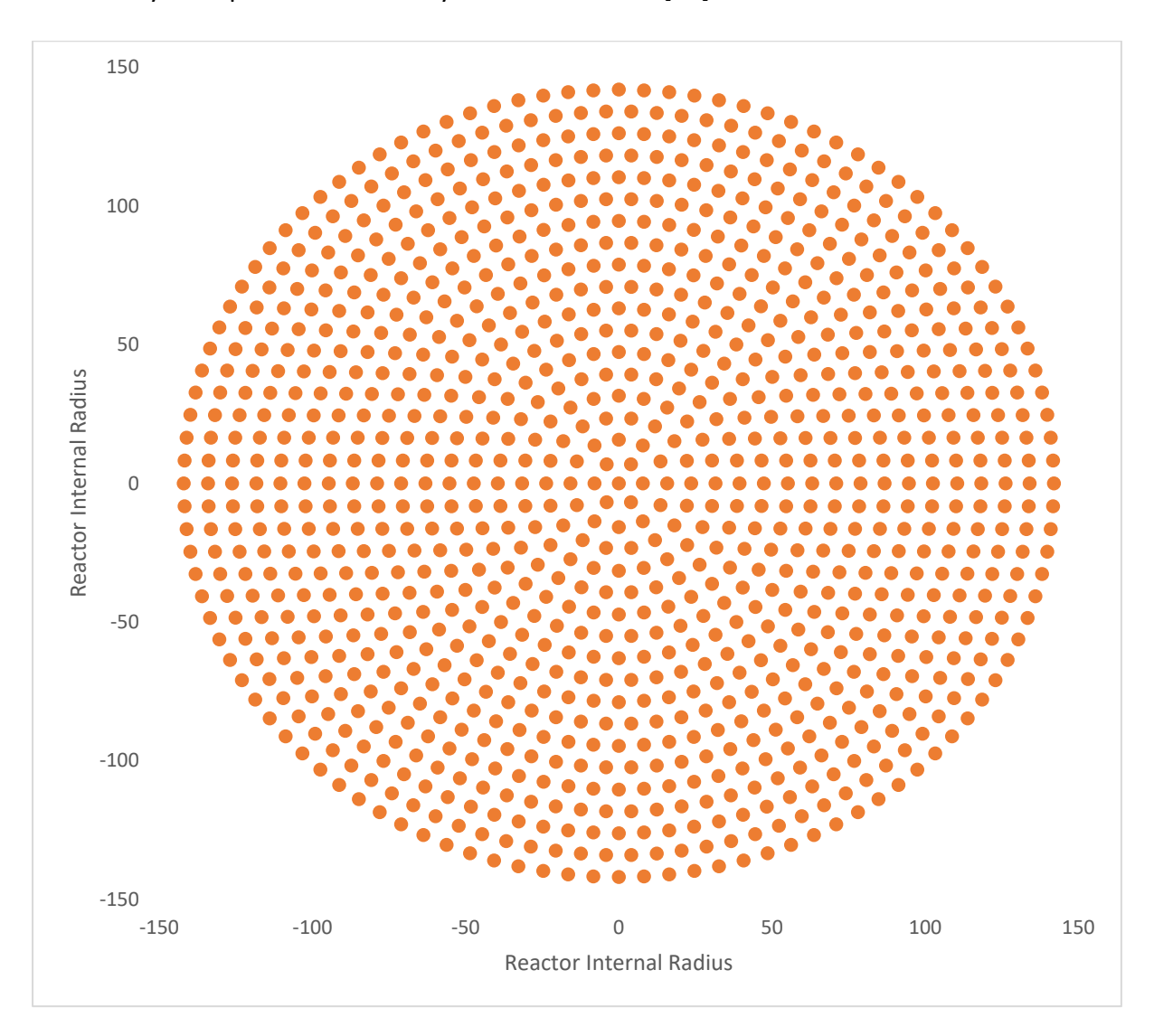


Figure 3-4: Streamline seeding points visualised in a 2d plane

The seeding points were defined in a structured grid with radial and circumferential spacing optimized through convergence studies. The coordinates of these seeding points were generated using a custom MATLAB script and imported into CFX-Post via CSV format. For the baseline configuration, 1000 streamlines were generated, originating from points distributed across concentric circles with varying numbers of points per circle to maintain approximately uniform area coverage. This distribution provides finer resolution near the reactor walls where velocity gradients are steepest while maintaining computational efficiency.

For each streamline, CFX-Post exports comprehensive data including:

- Three-dimensional spatial coordinates (x, y, z) at discrete points along the trajectory
- Velocity components (u, v, w) at each point
- Residence time from inlet to each point

The streamline data were exported to CSV files with a spatial resolution of 2 mm between consecutive points, ensuring sufficient detail for accurate UV dose integration. These flow field results serve as input to the proprietary MATLAB-based optical model developed by Typhon Treatment Systems Ltd (now NUUV), which calculates the UV radiation exposure along each streamline trajectory based on the reactor's LED array configuration and emission characteristics.

# **Integration of CFD and Optical Modeling**

The post-processing workflow establishes a seamless interface between CFD hydrodynamic analysis and UV dose prediction. By combining streamline trajectory data with the optical model's LED emission characteristics, this integrated methodology quantifies the relationship between reactor hydrodynamics and disinfection performance. The approach enables:

- Identification of flow patterns that enhance or diminish UV dose uniformity
- Quantification of residence time distribution effects on treatment efficacy
- Evaluation of design modifications (vane geometry, reactor length, LED arrangement)
   on overall performance
- Optimization of operating conditions (flow rate, LED power) for maximum efficiency

This comprehensive post-processing strategy provides the analytical foundation for the reactor performance evaluation presented in Chapters 4 to 7, and enables validation against experimental measurements

#### **Velocity Profile Extraction**

In addition to streamline generation, velocity profiles were extracted at strategic locations to quantify flow development through the reactor system. Line probes were positioned at the following locations:

- Reactor inlet plane (immediately downstream of the elbow)
- Reactor outlet plane (at the UV exposure zone exit)
- Middle cross-section of reactor length

Each line probe spans the full diameter of the pipe, with data points extracted using the cut intervals in CFD post to provide high-resolution velocity profiles. The velocity components extracted include:

- Axial velocity (v): primary flow direction component
- Tangential velocity (w): swirl component perpendicular to axial direction
- Radial velocity (u): cross-stream component

These velocity profiles enable quantitative assessment of flow characteristics including:

- Velocity profile development and symmetry
- Swirl intensity and decay through the reactor
- Flow uniformity and mixing behaviour
- Identification of recirculation zones or stagnation regions

## **Visualisation Planes and Contours**

Planar cross-sections were created at multiple locations throughout the geometry to enable two-dimensional visualization of flow quantities. Planes perpendicular to the axial flow direction (y-axis) were positioned at key locations including vane exit, elbow exit, reactor inlet, mid-reactor, and reactor outlet. Additional planes parallel to the flow direction (vertical and horizontal centre planes) provide longitudinal views of flow development.

On these planes, contour plots were generated for the following quantities:

- Velocity magnitude
- Individual velocity components (u, v, w)

Vector plots overlaid on these planes illustrate secondary flow patterns and vortex structures, particularly important for visualizing the swirling motion generated by the stationary vanes.

#### **Quantitative Flow Metrics**

Beyond visualization, several derived quantities were calculated in post-processing to provide quantitative metrics of reactor performance:

 Reynold number is defined as the ratio of inertial forces to viscous forces within a fluid flow. Reynolds number is widely used to determine whether the flow is laminar or turbulent, which is critical information in design of the fluid system.

Reynolds number is calculated based on the formula expressed below:

$$Re = \frac{\rho \times V \times L}{\mu} \tag{4}$$

Where:

- ρ is the fluid density (kg/m³)
- *V* is the characteristics velocity of the fluid (m/s)
- L is a characteristics linear dimension, in this case diameter of the reactor
- μ is the dynamic viscosity of the fluid
- Swirl number is calculated using the velocity components. Swirl number is defined as the dimensionless which is a ratio of axial flux of angular momentum to axial flux of axial momentum times the characteristics length scale. Higher swirl number indicates stronger swirling inside the pipe [84]–[86].

Formula for the swirl number is as given:

$$S = \frac{G_{\theta}}{R. G_{z}} \tag{5}$$

Where:

 $G_{\theta}$  = Angular momentum flux (kg.m/s<sup>2</sup>)

 $G_z$  = Axial momentum flux (kg.m/s<sup>2</sup>)

R = Characteristic radius of pipe or cylinder (m)

The angular momentum flux and axial momentum flux terms are calculated by integrating over the cross-section:

$$G_{\theta} = \int \rho V_r^2 \omega. \, dA \tag{6}$$

$$G_{\theta} = \int \rho V_z^2 . \, dA \tag{7}$$

Where:

 $\rho$  = Fluid density (kg/m3)

 $V_r$  = Tangential velocity (m/s)

 $V_z$  = Axial velocity (m/s)

 $\omega$  = Angular velocity (rad/s)

A = Cross-sectional area

#### 3.1.5. CFD Model Verification

To assess the spatial discretization error and determine the mesh resolution necessary for obtaining grid-independent results, a mesh convergence study was conducted. The Grid Convergence Index (GCI) method, proposed by Roache (1994), was employed for a consistent analysis of grid convergence.

#### **Mesh Refinement Strategy**

Three progressively refined meshes were generated with a refinement ratio of r = 1.1, achieved by uniformly scaling the mesh spacing throughout the domain. This refinement ratio represents a compromise between maintaining adequate resolution differences between grids and limiting computational expense, consistent with recommendations in the literature [69]. The three mesh configurations are designated as follows:

• Grid 1 (finest): 12.9 million nodes

• Grid 2 (medium): 9.4 million nodes

• Grid 3 (coarsest): 8.7 million nodes

The mesh refinement was applied uniformly across all regions of the domain, including the vane region, elbow, reactor section, and pipe extensions. For each mesh, the inflation layer settings (number of layers, growth rate, first layer thickness) were maintained constant to ensure consistent boundary layer resolution relative to the overall mesh density.

Each simulation was executed with identical physics settings, boundary conditions, and convergence criteria (residuals  $< 1 \times 10^{-6}$ ) to isolate the effect of spatial discretization. All three solutions achieved full convergence, with residuals reaching the target value, ensuring that iterative convergence errors did not confound the mesh independence assessment.

### **Monitoring Parameter**

The parameter selected for mesh convergence assessment must be representative of the overall solution accuracy and relevant to the study objectives. For this UV reactor simulation, averaged velocity magnitude at three strategic locations was chosen as the primary monitoring parameter.

Three monitoring locations were selected along the reactor:

- Reactor Inlet: Immediately downstream of the elbow, at the entrance to the UV exposure zone
- 2. Reactor Mid-plane: At 50% of the reactor length, representing the central UV exposure region
- 3. Reactor Outlet: At the exit of the UV exposure zone

Velocity magnitude was selected as the convergence monitoring parameter because:

- Direct relevance to flow development: Velocity magnitude captures the overall flow intensity through the reactor, which directly influences residence time and UV exposure duration.
- 2. Sensitivity to mesh resolution: Velocity magnitude is sensitive to accurate resolution of all three velocity components, including the complex swirling and secondary flows generated by the upstream vanes.

3. Multiple monitoring locations: By evaluating velocity at inlet, mid-plane, and outlet, the convergence study assesses mesh adequacy throughout the entire reactor length, not just at a single location.

Table 3-6 presents the mesh details and average velocity magnitude values at the three monitoring locations for each grid. The values are normalized relative to the coarsest grid (Grid 3) to facilitate convergence analysis.

Table 3-6: Grid convergence results normalized to the coarsest grid for mesh refinement

| Grid | Normalized grid | Number of  | Inlet  | Mid-plane | Outlet | Normalized |
|------|-----------------|------------|--------|-----------|--------|------------|
|      | spacing         | nodes      | (m/s)  | (m/s)     | (m/s)  | Inlet [%]  |
| 1    | 0.83            | 12,931,567 | 1.4523 | 1.4389    | 1.4312 | 100.34     |
| 2    | 0.91            | 9,378,251  | 1.4497 | 1.4371    | 1.4298 | 100.16     |
| 3    | 1.00            | 8,671,092  | 1.4474 | 1.4356    | 1.4286 | 100.00     |

The velocity magnitude shows systematic increase with mesh refinement at all three locations, with variations of approximately 0.3-0.4% between successive grids. The inlet location shows the largest sensitivity to mesh refinement, consistent with expectations for the most complex flow region. The mid-plane and outlet locations show similar but slightly smaller variations, indicating that the flow becomes more mesh-independent as it develops through the reactor.

## Order of convergence

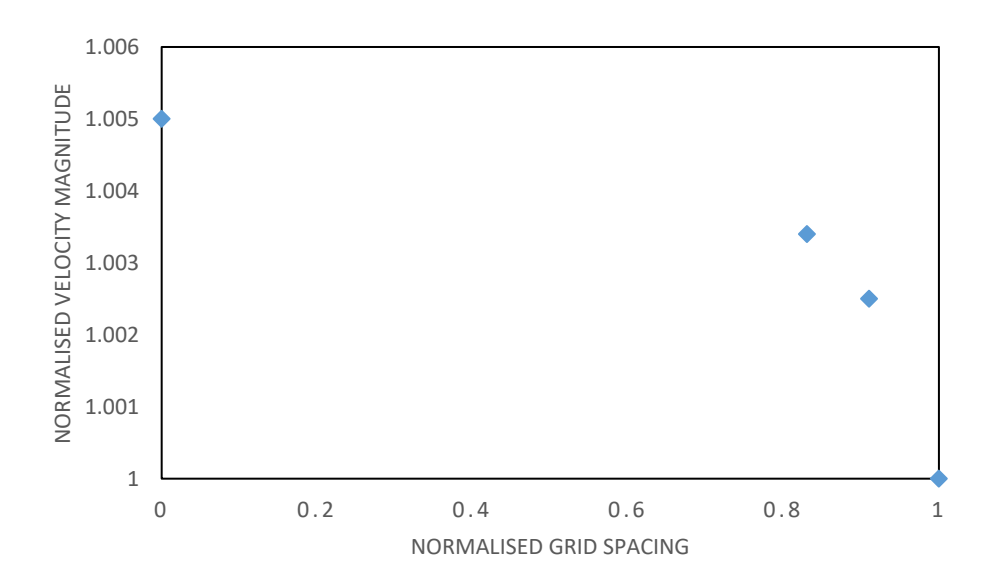
The observed order of convergence quantifies the rate at which the solution approaches the exact value as mesh spacing decreases. For a second-order accurate discretization scheme (as used in the High Resolution advection scheme), the theoretical order of convergence is p = 2.0. However, the observed order may differ due to factors such as mesh quality, geometric complexity, and the presence of mixed discretization schemes. Equation for calculating the order of convergence is:

$$p = \frac{\ln\frac{(n3 - n2)}{(n2 - n1)}}{\ln(r)} \tag{8}$$

The calculated order of convergence (p=1.23) is lower than the theoretical second-order accuracy, which is typical for complex geometries with mixed element types (tetrahedral and hexahedral), regions of high curvature, and strong swirling flows. This value is within the acceptable range (1.0 ) reported in CFD verification studies for similar reactor geometries

# **Richardson Extrapolation**

Using Richardson extrapolation, the velocity magnitude value at zero grid spacing is estimated at 1.005. This extrapolated value represents the best estimate of the exact solution at infinite mesh resolution.



# **Grid Convergence Index Calculation**

The Grid Convergence Index (GCI) provides a standardized measure of discretization uncertainty, expressed as a percentage of the computed value. The GCI is calculated as:

$$GCI_{12} = F_s \frac{n_1 - n_2/n_1}{r^p - 1} \tag{9}$$

 $F_s$  is taken as 1.25. The grid convergence results are as follows:

Table 3-7: Grid convergence criteria for mesh refinement

| Refinement ratio      | r                 | 1.1   |
|-----------------------|-------------------|-------|
| Order of convergence  | р                 | 1.23  |
| Safety factor         | Fs                | 1.25  |
| GCI for grids 1 and 2 | GCI <sub>12</sub> | 1.59% |
| GCI for grids 2 and 3 | GCI <sub>23</sub> | 1.78% |

The GCI<sub>12</sub> value of 1.59% indicates that the discretization uncertainty in the finest grid which is excellent for engineering applications involving complex internal flows.

## **Asymptotic Range Verification**

To verify that the solutions are in the asymptotic range of convergence (where the theoretical convergence rate is achieved), the following criterion is evaluated:

$$\frac{GCI_{23}}{r^p.GC1_{12}} = 0.998 \tag{10}$$

Since the calculated ratio is approximately 1.0 (within 0.02% of unity), the solutions are confirmed to be in the asymptotic range of convergence. This verification provides strong confidence that:

- The observed convergence behaviour is reliable and follows the theoretical convergence rate
- Further mesh refinement would continue to follow the predicted convergence trend
- The extrapolated value at zero grid spacing is an accurate estimate of the exact solution
- The finest mesh (Grid 1) provides adequately grid-independent results

## **Velocity Profile Comparison**

To assess mesh independence more comprehensively beyond the averaged velocity metric, detailed velocity profiles at the reactor inlet were compared across all three grids. Figure 3-5

present the normalized velocity components (u, v, w) as functions of normalized radial position (r/R), where r is the radial distance from the centerline and R is the reactor radius.

The comparative analysis demonstrates:

- Axial velocity (v component, Figure 3-5 (a)): Excellent agreement across all three
  meshes throughout the entire profile. The characteristic profile shape, showing the
  effects of swirl-induced velocity redistribution, is consistently captured by all three
  meshes.
- Radial velocity (u component, Figure 3-5 (b)): Excellent agreement across all three
  meshes throughout the entire profile. The secondary flow structures associated with
  swirl generation are well resolved even on the coarsest grid.
- Tangential velocity (w component, Figure 3-5 (c)): Excellent agreement across all three meshes throughout the entire profile. The profiles confirm that all three meshes adequately resolve the swirling motion generated by the upstream vanes.

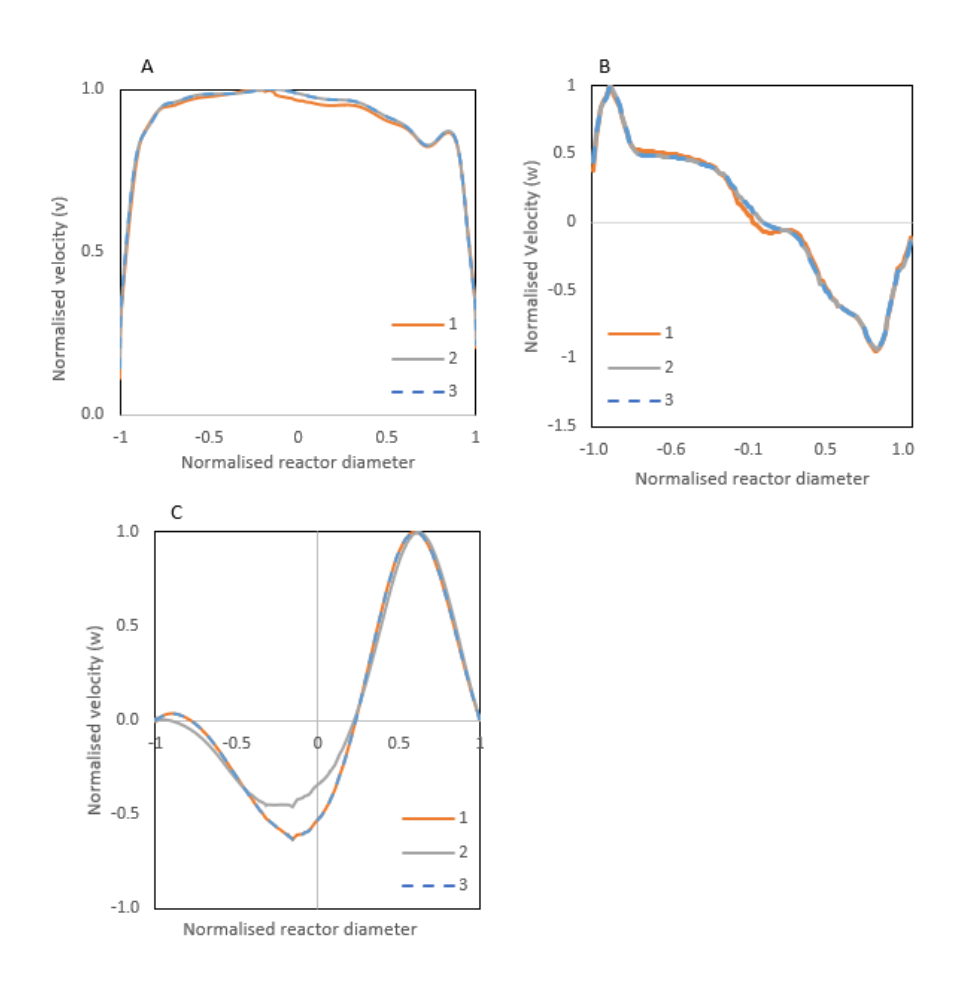


Figure 3-5: Normalised velocity profile for all three components for all three mesh

# 3.2. PIV experimental methodology

Experimental validation of the computational model was conducted using Particle Image Velocimetry (PIV), a non-intrusive optical measurement technique capable of capturing instantaneous velocity fields in fluid flows. The experimental campaign was designed to validate the CFD predictions of complex swirling flow patterns.

# 3.2.1 Test Rig Design and Scaling

A scaled experimental test rig was designed and manufactured at Lancaster University to replicate the key hydraulic features of the commercial UV LED reactor. Due to budgetary constraints and supply chain limitations for large-diameter transparent pipes during the experimental phase, the test section diameter was scaled to 200 mm (internal diameter: 194 mm) compared to the full-scale 310 mm reactor. This scaling maintains dynamic similarity while enabling practical laboratory implementation and optical access for PIV measurements.

The complete experimental assembly was designed in SolidWorks prior to manufacturing, ensuring geometric fidelity to the scaled reactor configuration. Figure 3-6 presents a three-dimensional representation of the complete PIV test rig, illustrating the key components including the inlet section, stationary vanes, elbow, measurement section with optical correction box, and outlet section.

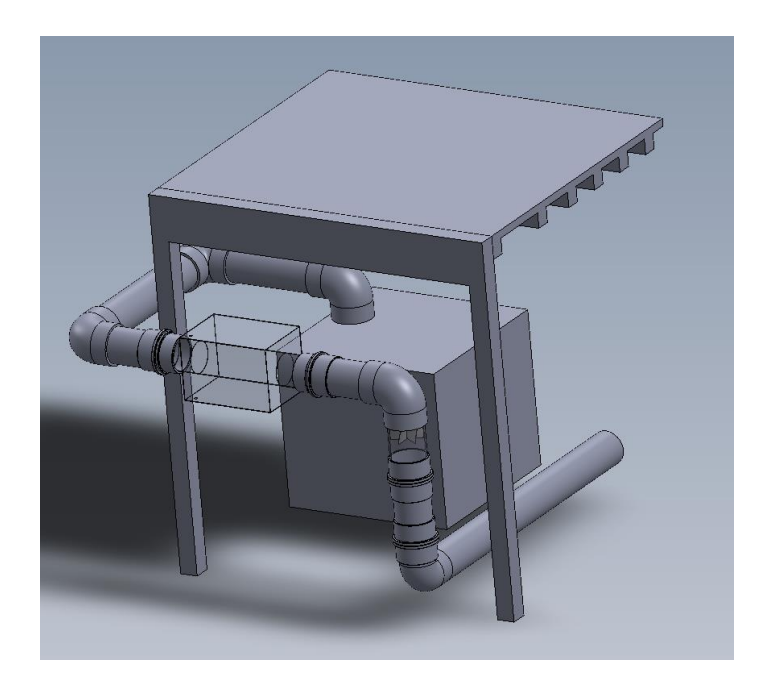


Figure 3-6: 3D representation of the experimental rig in SolidWorks

The test rig configuration incorporates:

• Inlet section: DN225 PVC pipe providing flow development length upstream of the

vanes

• Stationary vanes: 3D-printed scaled vanes matching the patented design geometry

• 90° Elbow: Standard PVC elbow positioned downstream of vanes to induce swirl

Measurement section: 1000 mm length transparent acrylic pipe (OD: 200 mm, ID: 194

mm, wall thickness: 3 mm)

• Optical correction box: Acrylic enclosure filled with water for refractive index

matching

Outlet section: Transition to collection tank

3.2.2 Optical Correction Box

A critical component of the PIV experimental setup is the optical correction box, which

minimizes optical distortions caused by the curved pipe surface. Light rays passing through

curved transparent surfaces experience refraction according to Snell's law, introducing

geometric distortions and measurement errors in particle image analysis. The correction box

addresses this challenge by providing a flat optical interface and refractive index matching

between the pipe material and surrounding medium.

The correction box was custom-designed and manufactured from transparent acrylic sheets

with the following specifications:

Internal dimensions: 300 mm (width) × 300 mm (height) × 800 mm (length)

Wall thickness: 10 mm acrylic

• Optical quality: Clear cast acrylic with minimal birefringence

Mounting: Two circular acrylic plates machined with 200 mm diameter holes to

precisely fit the external diameter of the measurement pipe

Figure 3-7 shows the preparation stage of the acrylic box assembly, while Figure 36 presents

the manufactured correction box installed around the clear measurement pipe. The detailed

48

dimensions of the correction box are provided in Figure 3-8, showing the relationship between the circular pipe penetrations and the rectangular outer enclosure.



Figure 3-7: Preparation of the acrylic box around the clear pipe for PIV experimennts



Figure 3-8: Manufactured acrylic box around the clear pipe for PIV experiments

# 3.2.2.1 Manufacturing Process

The correction box was assembled from four separate acrylic plates (two end plates with circular penetrations, one bottom plate, and two side plates) as illustrated in Figure 35. The manufacturing sequence was as follows:

- End plate preparation: Two 300 × 300 mm acrylic plates were machined with precision 200 mm diameter holes at their centers using CNC milling to ensure concentricity and smooth edges
- 2. **Pipe mounting**: The clear acrylic measurement pipe was inserted through both end plates, with the pipe positioned precisely at the measurement location along the test rig

- 3. **Initial bonding**: The end plates were bonded to the pipe ensuring watertight seals at the pipe penetrations
- 4. **Box assembly**: The bottom and side acrylic plates were sequentially bonded to the end plates, creating a rectangular enclosure around the measurement section
- 5. **Fill port installation**: A 25 mm diameter hole was drilled in the top center of the box for water filling.

#### 3.2.2.2 Optical Principles

The correction box operates on two principles:

- 1. **Refractive index matching**: Filling the box with water (n  $\approx$  1.33) closely matches the refractive index of acrylic (n  $\approx$  1.49), reducing refraction at the pipe/fluid interface
- 2. **Planar optical interface**: The flat outer walls of the correction box provide undistorted optical paths for the laser sheet and camera viewing

While ideally a fluid with refractive index exactly matching acrylic would be used, water provides a practical and safe alternative. Residual optical distortions due to the refractive index mismatch ( $\Delta n \approx 0.16$ ) are corrected during calibration using Snell's law calculations and the calibration target positioned at the measurement plane centerline.

## 3.2.3 Stationary Vane Manufacturing

The stationary guide vanes represent the most geometrically complex component of the test rig, responsible for generating the swirling flow that enhances mixing and UV dose uniformity in the reactor. These vanes were manufactured 3D printing technology, which offers several advantages for experimental prototype fabrication:

- Rapid manufacturing without tooling requirements
- Complex geometric fidelity to the CAD design
- Cost-effective for single-unit production
- Easy modification if design iterations are required

## **Design and Scaling:**

The vane geometry was scaled from the full-scale patent design, maintaining all critical dimensional ratios:

- Vane angle relative to flow axis
- Vane chord length to pipe diameter ratio
- Vane spacing and circumferential distribution
- Hub and tip clearances

The scaled vane assembly was designed in SolidWorks as a single integrated component including the vane blades, central hub, and mounting features. The design was exported in STL (stereolithography) format for 3D printing.

#### **Material Selection Rationale:**

Polyethylene Terephthalate Glycol-modified (PETG) was selected as the manufacturing material for the following reasons:

- Water resistance: Excellent resistance to water absorption and degradation during extended submersion
- 2. **Mechanical strength**: Sufficient rigidity to maintain geometric shape under flow-induced loads
- 3. **Durability**: High impact resistance prevents damage during installation and removal
- 4. **Printability**: Lower warping tendency compared to ABS, enabling accurate dimensional reproduction

Figure 3-9 shows the manufactured stationary vane assembly produced using the 3D printing process. The vanes were printed as a single monolithic component to eliminate assembly errors and ensure precise angular alignment.

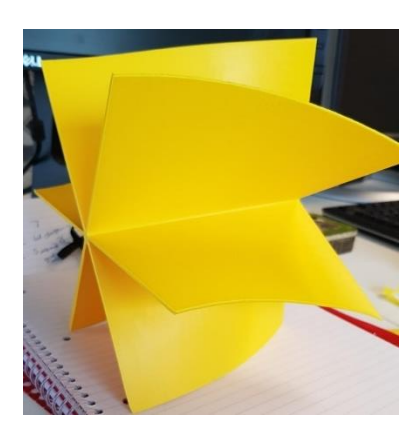


Figure 3-9: Manufactured static vanes using 3D printer

## 3.2.4 Additional Test Rig Components

## **Pipe Connections:**

Standard PVC plumbing components were utilized for the majority of the test rig:

- Stub flanges: Connect the transparent measurement section to the upstream PVC piping
- Reducing bushings: Transition from DN225 PVC pipe to DN200 transparent pipe, matching the diameter reduction present in the full-scale reactor (DN310 to quartz tube)
- **PVC elbow**: 90° standard radius elbow positioned downstream of the stationary vanes

## **Structural Support**

The correction box assembly, when filled with water, represents significant additional mass that requires adequate structural support. A custom support structure was designed and fabricated from available laboratory materials.

Figure 39 shows the complete installed test rig with all components assembled, including the support structure, PIV instrumentation, and flow system integration.

## **Flow System**

A variable-speed centrifugal pump circulated water through the closed-loop test rig. Flow rate was controlled by adjusting the VFD frequency, with real-time monitoring using an electromagnetic flow meter positioned upstream of the measurement section. Table 3-8

presents the relationship between flow rate, velocity, and pump operating parameters for the three primary test conditions.

Table 3-8: Lab flow conditions for PIV experiments

| Reynolds | Rig Flow | Rig      | Frequency | Current | Torque | Motor | Motor |
|----------|----------|----------|-----------|---------|--------|-------|-------|
| number   | rate     | velocity | (Hz)      | (A)     | (%)    | Speed | Power |
|          | (m3/h)   | (m/s)    |           |         |        | (rpm) |       |
| 110774   | 87.7     | 0.6773   | 18.1      | 13.6    | 13.5   | 538   | 0.7   |
| 165735   | 131.21   | 1.0133   | 22        | 13.9    | 17.9   | 653   | 1.2   |
| 221455   | 175.4    | 1.3546   | 26.7      | 25.5    | 24.5   | 791   | 2     |

# 3.2.5 PIV Systems and procedures

This section describes the PIV system components, flow control equipment, calibration procedures, and measurement protocols. The experimental methodology encompasses the systematic approach to multi-plane, multi-location velocity measurements across different geometric configurations and operating conditions.

## **Laser System:**

A dual-cavity Nd:YAG (neodymium-doped yttrium aluminum garnet) laser was employed for flow illumination:

• Wavelength: 532 nm (green light, frequency-doubled)

• Energy per pulse: 200 mJ

• **Pulse duration**: 5-10 ns

Repetition rate: 15 Hz (maximum)

• Sheet optics: Cylindrical lens assembly creating a 1 mm thick laser sheet

The laser head was positioned perpendicular to the measurement pipe, with the sheet aligned vertically through the pipe centerline.

## **Camera System:**

A high-resolution scientific CCD (Charge-Coupled Device) camera captured particle images:

• **Sensor resolution**: 2048 × 2048 pixels

• **Pixel size**: 7.4 μm × 7.4 μm

• **Bit depth**: 12-bit (4096 gray levels)

• Lens: 35 mm focal length, f/2.8 maximum aperture

• Optical filter: 532 nm bandpass filter (blocks ambient light, passes laser wavelength)

• Frame rate: 15 Hz (synchronized with laser pulses)

The camera was positioned 0.55 m from the measurement plane centerline, providing a field of view (FOV) of approximately  $200 \times 200$  mm, which captures the full pipe internal diameter with small margins. This standoff distance was calculated based on the lens focal length (35 mm) and desired magnification to achieve the target FOV while maintaining adequate depth of field. Figure 3-10 shows the setup of camera and laser in the lab.



Figure 3-10: PIV experimental setup with camera and laser

## **Seeding particles**

PIV measurements require neutrally buoyant tracer particles that followd the flow without affecting fluid behavior. Silver-coated hollow glass spheres were selected as seeding particles. Particles were introduced upstream of the measurement section through a dedicated injection port. Figure 3-11 shows the complete PIV experimental setup during operation, with the laser sheet illuminating seeding particles within the measurement section. The black cloth enclosure visible in the image eliminates ambient light contamination, ensuring that only laser-scattered light from particles reaches the camera sensor.

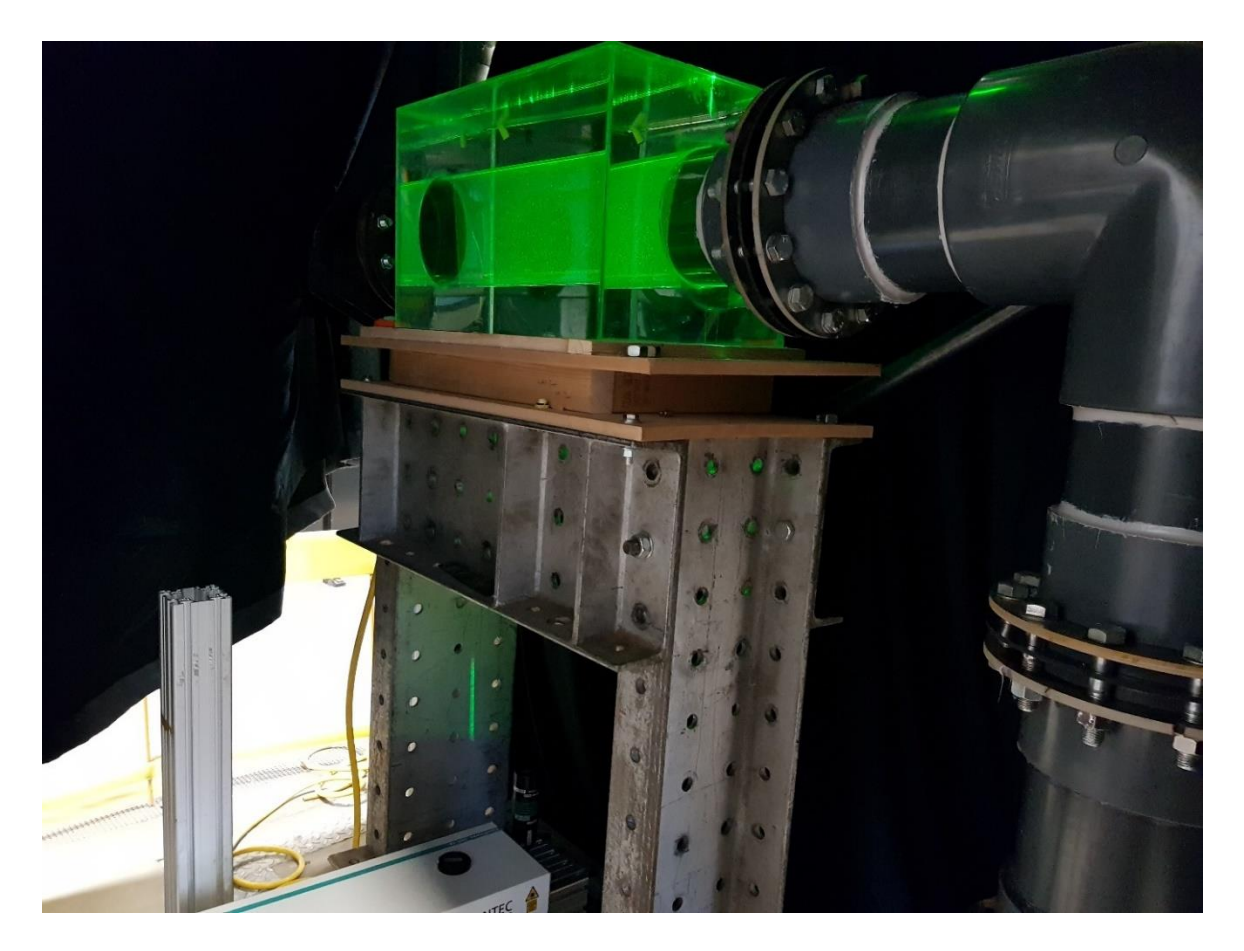


Figure 3-11: PIV setup with laser fired up to show the seeding particles

#### **Calibration Procedure**

Accurate PIV measurements require precise calibration to establish the relationship between image pixel coordinates and physical spatial coordinates in the measurement plane. This calibration accounts for camera perspective, lens distortion, and optical refraction through the correction box.

## **Calibration Target:**

A precision-manufactured calibration plate was used for spatial calibration:

Pattern: Regular array of circular dots on white background

• **Dot spacing**: 10 mm (center-to-center)

• **Dot diameter**: 2 mm

• Array size: 20 × 20 dots covering 200 × 200 mm area

• Material: Rigid aluminum composite with printed pattern

• Flatness tolerance: < 0.1 mm across full area

#### **Calibration Procedure:**

Target positioning: The calibration plate was inserted into the measurement pipe and
positioned precisely at the centerline (98.5 mm from the pipe wall). Figure 3-12 shows
the calibration setup used.

• Laser activation: The laser was activated at low power to illuminate the calibration target, creating high-contrast images of the dot pattern.

• **Focus optimization**: Camera focus was carefully adjusted until the calibration dots appeared sharp with maximum edge contrast. Fine focus adjustment was performed iteratively while monitoring image sharpness metrics in the acquisition software.

• Image acquisition: Multiple calibration images (typically 10-20) were captured and averaged to reduce noise.

• **Automatic detection**: PIV processing software automatically detected dot centroids in the calibration image using intensity thresholding and centroid calculation algorithms.

 Validation: Calibration accuracy was verified by comparing known physical distances (10 mm dot spacing) with calculated distances from the mapping function. Calibration was accepted when errors were < 0.3% across the full field of view.</li>

• **Target removal**: After successful calibration, the target was carefully removed without disturbing the camera, laser, or correction box positions.

```
Central: 4 mm
Normal 2 mm
Spacing: 5 mm
Spacing: 5 mm
```

Figure 3-12: Calibration section used for the calibration of the PIV experiments

#### 5.2.4 Measurement Locations and Planes

Measurements were conducted at two primary axial locations along the measurement section, designated as:

- Position A (Entry): 100 mm downstream of the elbow exit (near the elbow),
   corresponding to the inlet of the UV reactor in the full-scale system
- Position B (Exit): 700 mm downstream of the elbow exit (away from the elbow),
   corresponding to the outlet of the UV reactor in the full-scale system

The 600 mm spacing between these locations matches the scaled reactor length and enables direct comparison with CFD predictions of flow development through the reactor.

At each axial location, measurements were performed in two orthogonal planes:

- Vertical plane: Laser sheet oriented vertically, passing through the pipe centerline
- Horizontal plane: Laser sheet oriented horizontally, passing through the pipe centerline

This multi-plane measurement strategy provides comprehensive three-dimensional flow field information, enabling reconstruction of the complete velocity vector field and validation of all three velocity components (u, v, w) predicted by CFD.

## **Measurement Configurations**

Three distinct geometric configurations were investigated to assess the influence of vane position and presence on flow characteristics:

**Configuration 1 (Primary)**: Stationary vanes positioned upstream of the elbow (matching the full-scale reactor design and CFD model). This configuration represents the baseline design and receives detailed analysis in this thesis.

**Configuration 2**: Stationary vanes positioned downstream of the elbow (between elbow and measurement section). This configuration was investigated to assess whether downstream vane placement might enhance mixing effectiveness.

**Configuration 3**: No vanes present (elbow only). This configuration isolates the contribution of the elbow alone to swirl generation and provides a baseline for quantifying vane effectiveness.

For each configuration, measurements were conducted at three flow rates: 87, 132, and 175 m<sup>3</sup>/h, corresponding to Reynolds numbers of 110,774, 165,735, and 221,455 respectively (Table 13). The maximum flow rate was limited to 175 m<sup>3</sup>/h to prevent overflow from the recirculation tank and minimize risk of leakage from the correction box seals.

## 3.2.6 Image Processing and Analysis

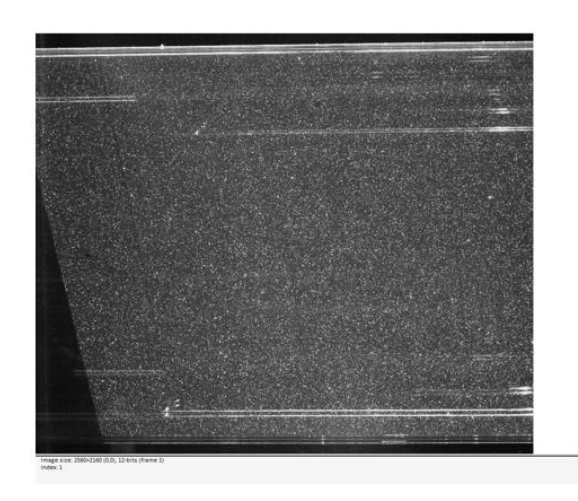
Raw particle images require pre-processing to enhance signal quality and remove noise sources before velocity calculation.

#### **Background Subtraction:**

Figure 3-13 shows a raw particle image with visible noise from wall reflections and non-uniform laser sheet intensity. To remove this background noise, a minimum image was generated by computing the pixel-wise minimum intensity across 150 frames acquired without seeding particles (Figure 3-14). This minimum image captures all static noise sources including:

- Wall reflections from pipe and correction box surfaces
- Non-uniform laser sheet intensity profile
- Optical aberrations and flare

The minimum image was subtracted from all particle images, resulting in clean images with uniform background (Figure 3-15). This background subtraction significantly improves correlation peak detection in subsequent processing.



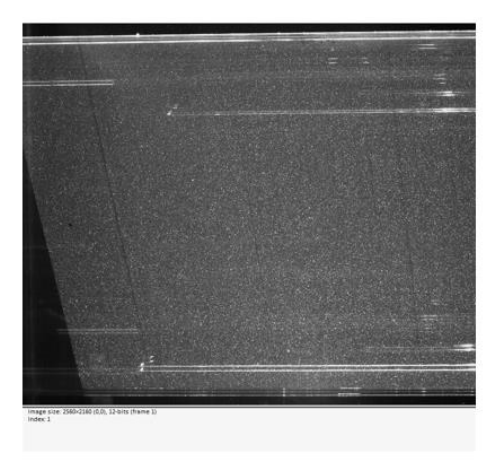


Figure 3-13: Image taken during PIV experiments showcasing the noise in the system due to reflection

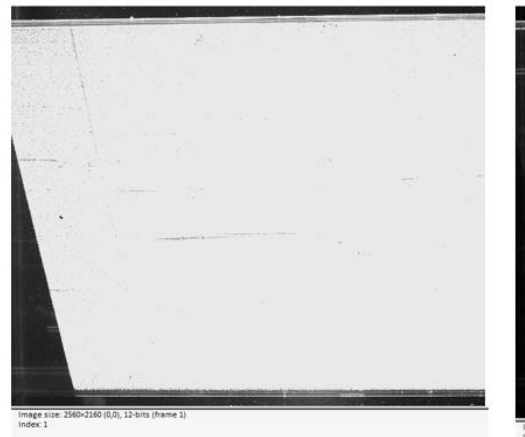




Figure 3-14: Images taken in the PIV experiments without the seeding particles

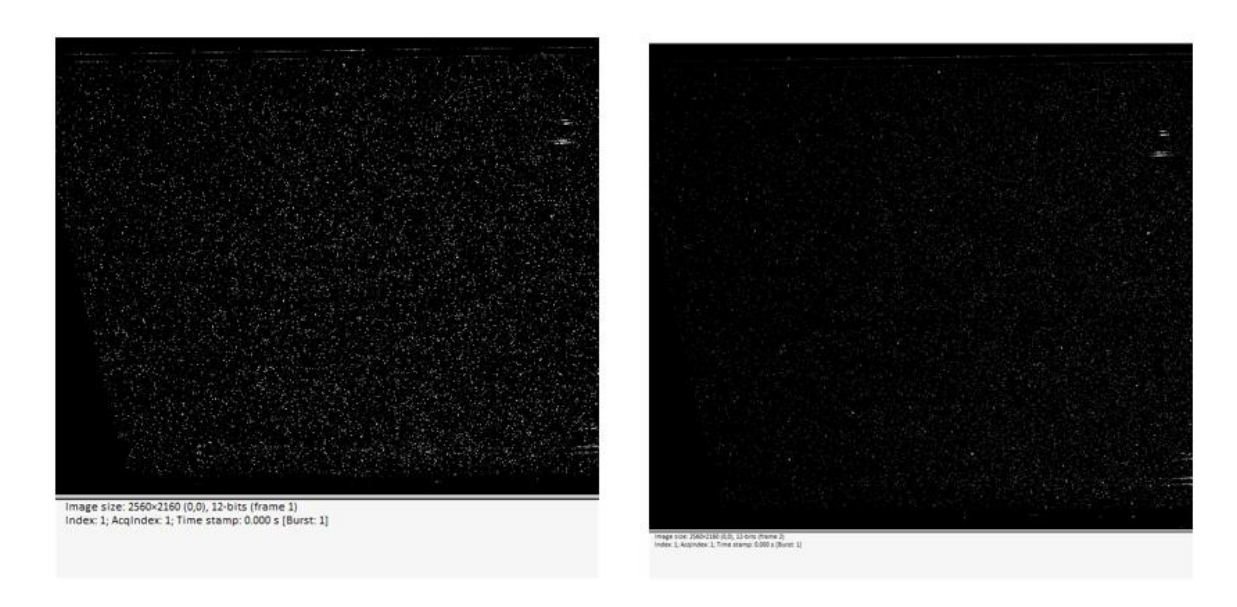


Figure 3-15: Images from the PIV experiments without the noise

# **Velocity Field Calculation**

Velocity fields were calculated from pre-processed image pairs using cross-correlation PIV algorithms implemented in the ePIV software package (Figure 3-16). The processing employed a multi-pass interrogation strategy with window deformation. This multi-pass approach improves dynamic range and accuracy by first capturing large-scale displacements with large windows, then refining to smaller windows for higher spatial resolution. Window deformation compensates for velocity gradients within interrogation regions, reducing peak-locking errors.

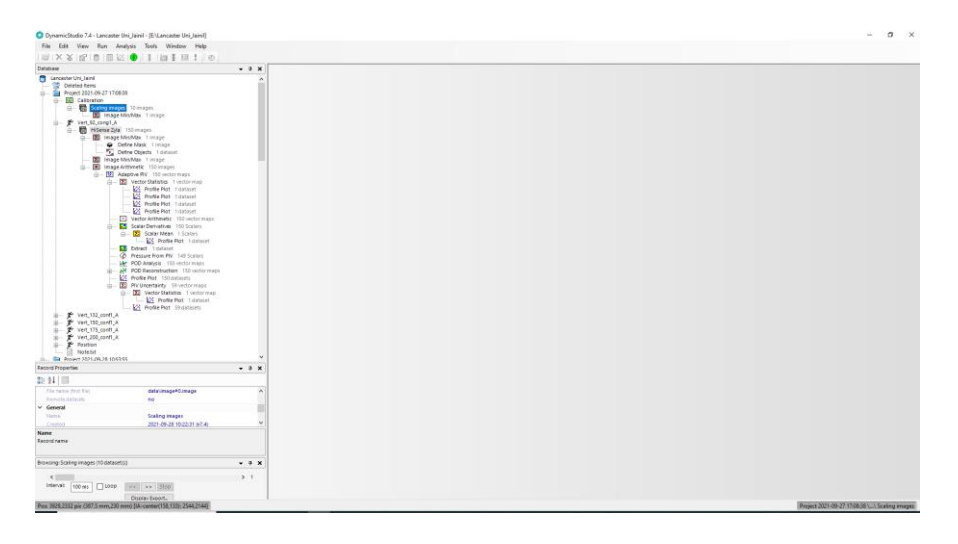


Figure 3-16: The ePIV setup for post processing of the results

## 3.3. Validation of the model

The validation of the CFD model was conducted through two independent methodologies, each targeting different aspects of the reactor performance. The dual validation approach ensures comprehensive verification of both the hydrodynamic predictions and the ultimate performance metric—UV disinfection efficacy. Two validation strategies were employed:

- UV dose Validation (Biodosimetry): Comparison of predicted Reduction Equivalent
  Dose (RED) values from the integrated CFD-optical model against experimental
  biodosimetry measurements conducted by Typhon Treatment Systems Ltd. This
  validation directly assesses the model's ability to predict the actual disinfection
  performance of the reactor.
- 2. **Flow Field Validation (PIV)**: Comparison of predicted velocity fields, profiles, and flow structures against Particle Image Velocimetry (PIV) measurements conducted in the scaled experimental test rig. This validation verifies the accuracy of the underlying hydrodynamic predictions that form the basis for UV dose calculations.

Together, these validation approaches provide confidence that the model accurately captures both the fundamental flow physics and the resultant treatment performance.

#### 3.3.1 Validation of the reactor for UV dose

UV reactor validation through biodosimetry follows established protocols for assessing disinfection performance using challenge microorganisms. The validation experiments were conducted by Typhon Treatment Systems Ltd (now NUUV) [87]. The validation tests were performed on a full-scale UV LED reactor with specifications closely matching the CFD model geometry. The only difference to the commercial BIO310 model is the difference in the location of the heat exchanger. The heat exchanger module is positioned upstream of the reactor in the validation system, whereas it is located downstream in the commercial BIO310. MS2 bacteriophage was selected as the challenge microorganism for validation testing. Following are the conditions of the experiments.

- Reactor designation: Prototype full scale UV LED water treatment system
- Reactor diameter: 310 mm (matching the CFD model)
- LED configuration: 1000 UV-C LED units (LG Innotek) arranged in 50 rings of 20 LEDs
   each

- LED wavelength: 275 nm
- UVT range tested: 90%, 95%, and 98%
- UVT control: SuperHume concentration adjusted to achieve target UVT values
- Flow rates tested: 80, 125 and 250 m³/h

#### Methodology

For each experimental test condition, the corresponding CFD simulation was performed using the validated mesh. Following steps were involved:

- Step 1: CFD Simulation: A steady-state CFD simulation was executed for each flow rate (80, 125, and 250 m³/h)
- Step 2: Streamline Generation: For each converged flow solution, 1000 streamlines were generated from the reactor inlet plane.
- Step 3: UV dose Calculation: The streamline data were input to the proprietary MATLAB-based optical model developed by Typhon Treatment Systems Ltd. The optical model incorporates:
  - LED emission characteristics: Spectral distribution, angular intensity pattern,
     total radiant power for LG Innotek 275 nm LEDs
  - Optical geometry: Position and orientation of all 1000 LEDs, reflector geometry and efficiency
  - Ray tracing: Multiple Point Source Summation (MPSS) method calculating UV intensity at each point along streamline trajectories
  - Water absorption: Beer-Lambert law with absorption coefficient.
  - Dose integration: UV dose accumulated along each streamline.
- Step 4: RED Calculation: RED is defined as the UV dose that would achieve the same log reduction in a collimated beam test as observed in the reactor. The Reduction Equivalent Dose (RED) was calculated from the streamline dose distribution:
  - Dose distribution: The 1000 streamline doses were sorted to generate the cumulative dose distribution
  - The model outputs Mean dose across all streamlines, RED value, Dose distribution histogram, Minimum and maximum doses

 Step 5: Comparison with Experimental Data: Predicted RED values from the model were compared against experimental RED values for all test conditions.

# 3.3.2 Validation of the Reactor Using PIV Experiments

The second validation approach compared CFD predictions against PIV experimental measurements of velocity fields in the scaled reactor model. This validation directly assesses the accuracy of the flow field predictions that underpin the UV dose calculations, providing confidence in the fundamental hydrodynamics captured by the model. While biodosimetry validation confirms that the integrated CFD-optical model correctly predicts overall disinfection performance, it does not isolate the accuracy of the CFD component from the optical model. PIV validation provides independent verification of the CFD predictions by directly measuring velocity fields and comparing against numerical predictions. This approach:

- Isolates CFD accuracy from optical model assumptions
- Enables point-by-point quantitative comparison of velocity components
- Validates complex flow features (swirl, secondary flows, velocity gradients)

#### 3.3.2.1 Development of scaled CFD model

To enable direct comparison with PIV experiments, a new CFD model was developed replicating the exact geometry of the experimental test rig. The computational model employed identical meshing strategies, physics definitions, turbulence modeling (SST), solver settings, and boundary condition specifications as described in Section 3.3 for the full-scale reactor geometry. The primary geometric difference is the reactor diameter, which was set to 194 mm to match the internal diameter of the transparent acrylic measurement section used in the PIV experiments. The SolidWorks geometry precisely replicated all experimental components including the 3D-printed stationary vanes, 90° PVC elbow, DN225 to DN200 reducer, and 1000 mm measurement section. The resulting mesh contained 3.2 million elements and 1.1 million nodes, with enhanced resolution in the measurement section to provide high-fidelity velocity predictions for point-by-point comparison with PIV data.

# 3.3.2.2 Comparison Methodology

The PIV-CFD comparison was conducted through multiple complementary approaches to provide comprehensive validation.

- Velocity Profile Comparison: Velocity profiles extracted from CFD and PIV were compared by plotting on the same axes to assess agreement. Profiles were normalized by the mean axial velocity for dimensionless comparison.
- Velocity Contour Comparison: Two-dimensional velocity fields from CFD and PIV were compared.
- Swirl Intensity Comparison: Swirl numbers calculated from CFD were compared against values derived from PIV measurements to assess accuracy of swirl prediction

# 3.4 Conclusion

This chapter has presented a comprehensive methodology integrating computational and experimental approaches to develop and validate predictive models for commercial-scale UV LED water treatment reactors. The methodology addresses critical research gaps through systematic investigation combining numerical simulation, optical modeling, and dual experimental validation.

The CFD modeling framework employs three-dimensional simulations using the SST k- $\omega$  turbulence model, selected for its demonstrated accuracy in swirling flow. Rigorous mesh independence studies established convergence with 4.3 million elements Detailed justification of all boundary conditions, solver settings, and turbulence parameters through literature references ensures methodological rigor and reproducibility.

Integration with Typhon's proprietary optical ray-tracing model enables UV dose prediction by tracking 1000 streamlines extracted from converged flow fields. This coupled approach accounts for complex LED emission patterns, reflector optics, and wavelength-specific absorption effects that simple analytical irradiance models cannot capture.

The dual validation strategy provides comprehensive model assessment: biodosimetry experiments quantify ultimate performance (RED values) across nine operating, while PIV measurements characterise detailed three-dimensional velocity fields in a scaled reactor at

Reynolds numbers representative of commercial operation. This integrated validation enables decomposition of error sources and establishes confidence limits for design applications.

This comprehensive framework enables achievement of research objectives: validated model development, swirl characterization, geometric sensitivity analysis, and establishment of design guidelines for commercial implementation.

# Chapter 4. Results and Discussion

The comprehensive evaluation of the reactor involves two methodologies. Firstly, a thorough examination of the flow characteristics within the reactor is conducted. This encompasses an in-depth analysis of velocity profiles and streamlines, essential for gaining insights into the intricate dynamics of fluid movement within the system.

Velocity profiles offer a detailed understanding of how fluid velocities vary across different sections of the reactor, providing critical information about the distribution and magnitude of velocities at both the inlet and outlet. Velocity profiles give information on how the flow passes through the reactor, aiding in the assessment of flow development.

Simultaneously, the analysis of streamlines provides a visual representation of flow trajectories, offering valuable insights into mixing behaviour, residence time distribution, and the presence of any dead zones within the reactor. Streamline visualization helps in identifying regions where fluid particles travel along similar paths and areas where mixing occurs. These streamlines are exported in a csv file with details on the path traversed by each particle.

The second facet of reactor evaluation involves quantifying the UV dose received by the water passing through the system. This assessment considers a multitude of factors, including flow characteristics, residence time, and the UV irradiation in the reactor. Understanding the intricate interplay between these variables is paramount, as it directly influences the effectiveness of UV treatment. Dosage quantification enables the assessment of treatment efficacy and the reactor's ability to deliver the desired level of exposure necessary. In essence, the combined evaluation of flow characteristics and UV dose provides a holistic understanding of reactor performance.

# 4.1 Flow Characteristics in the Full-Scale UV LED Reactor

The analysis reveals complex three-dimensional flow structures within the UV LED reactor, characterized by strong swirling motion induced by the upstream stationary vanes and 90° elbow. Figure 4-1 presents velocity contours on a plane at the reactor inlet (100% flow rate, 250 m³/h), demonstrating the formation of intense vortical structures. The velocity vectors

exhibit clear spiral trajectories rather than axial flow paths, confirming successful swirl generation by the upstream flow conditioning system.

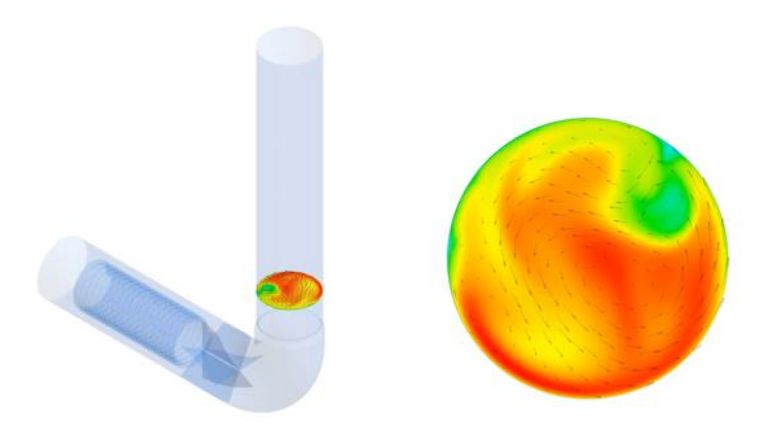


Figure 4-1: a) Location of the plane within the reactor b) View of the velocity contours at the inlet of the reactor

The streamline visualization in Figure 4-2 illustrates the helical flow patterns through the reactor. With 1000 streamlines seeded uniformly at the reactor inlet, the three-dimensional trajectories reveal that water particles follow spiral paths rather than straight axial trajectories. This swirling motion serves two critical functions for UV disinfection: enhanced cross-sectional mixing that ensures uniform UV exposure distribution, and extended residence time within the irradiated zone compared to purely axial flow. These strong inlet vortices significantly improve mixing in the core flow and minimize stagnant zones that lead to uneven UV absorption issues in conventional mercury lamp reactors. The superior mixing enabled by the swirl ensures water particles are well dispersed upon entering the reactor, maximizing absorption uniformity. In contrast to conventional UV reactors with axial flow where particles near the wall may receive insufficient UV exposure while particles near lamp surfaces may receive excessive doses, the swirling flow in the LED reactor promotes radial mixing that homogenizes the dose distribution across the cross-section.

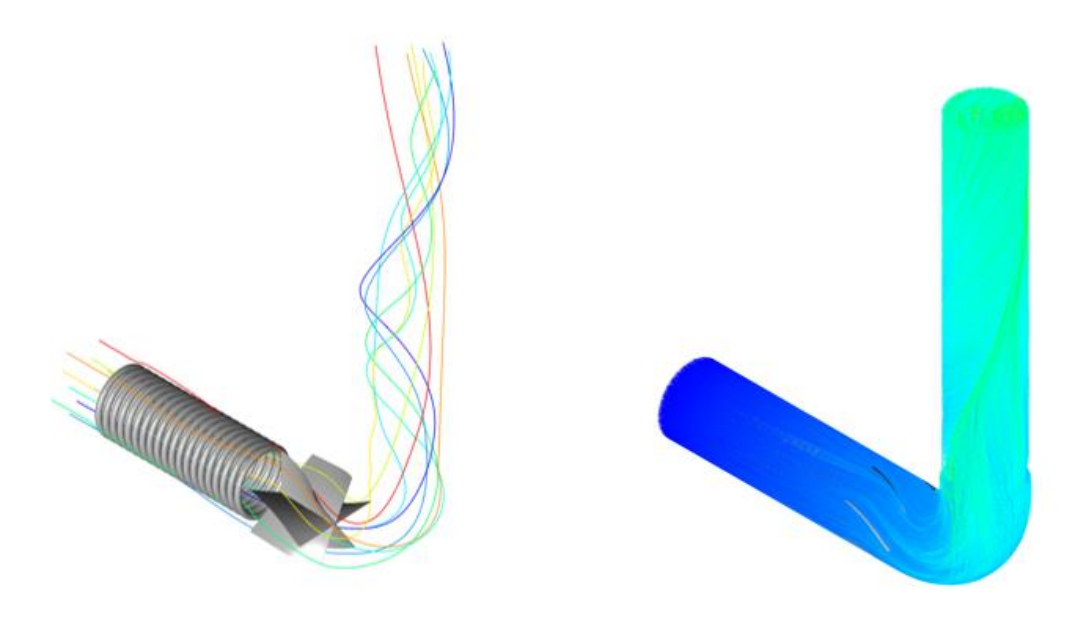


Figure 4-2: a) 5 streamlines within the reactor b) Reactor with 1000 streamlines

#### 4.1.1 Residence Time Enhancement:

The swirling flow significantly extends particle residence time within the UV exposure zone compared to purely axial flow. Analysis of the 1000 streamlines generated from the CFD solution provides quantitative characterization of this enhancement effect.

For a reactor axial length of L\_axial = 1.29 m (axial distance from inlet to outlet of the UV exposure zone) and average axial velocity of  $\bar{v}$ \_axial = 1.13 m/s, the theoretical residence time for straight axial flow would be:

$$t_{axial} = \frac{L_{axial}}{\bar{v}_{axial}} = \frac{1.29}{1.13} = 1.14s \tag{11}$$

However, the swirling motion causes particles to follow helical trajectories rather than straight axial paths. Analysis of the streamline residence times through the reactor reveals a mean residence time of:

$$t_{swirt} = 1.48 \,\mathrm{s} \tag{12}$$

This represents a 30% increase in residence time compared to purely axial flow at the same volumetric flow rate:

Residence time enhancement = 
$$\frac{t_{swirl} - t_{axial}}{t_{axial}} \times 100\% = \frac{1.48 - 1.14}{1.14} \times 100\% = 30\%(13)$$

This substantial residence time increase directly translates to 30% higher UV dose for the same LED power and reactor geometry, as UV dose is the time-integrated exposure to UV intensity along each particle's trajectory. The mean streamline path length can be calculated as:

$$L_{path} = t_{swirl} \times \bar{v}_{path} \tag{14}$$

where the mean path velocity is:

$$\bar{v}_{path} = \frac{L_{axial}}{t_{axial}} = 1.13 \text{ m/s } (15)$$

Therefore:

$$L_{nath} = 1.48 \times 1.13 = 1.67 \text{ m} (16)$$

This represents a 30% increase in path length over the axial distance, indicating that the helical trajectories add approximately 380 mm to the travel distance through the reactor.

The residence time enhancement is a significant benefit of the swirl-based design, enabling:

- Higher treatment capacity: For a given LED power and target UV dose, the 30% residence time increase contributes to improved treatment efficiency
- Improved dose delivery: The extended exposure time ensures more complete UV absorption, particularly important for achieving high log reductions of resistant microorganisms
- Energy efficiency: The same disinfection performance can be achieved with lower LED power, reducing operational costs

While the 30% residence time increase provides substantial performance benefits, the primary advantage of the swirl generation lies in the enhancement of cross-sectional mixing. The radial and tangential velocity components continuously redistribute particles across different radial positions, exposing them to varying UV intensity levels and homogenizing the dose distribution. This mixing effect is critical for achieving uniform UV dose across all water particles.

Traditional parallel-flow mercury lamp reactors without swirl generation exhibit minimal residence time variation, as particles follow essentially straight paths parallel to the lamp axes. The engineered swirl in this LED reactor provides both extended residence time (30% increase) and, more importantly, enhanced mixing that addresses the critical challenge of dose uniformity in UV reactors. The combination of these effects, extended exposure and improved uniformity creates a synergistic improvement in disinfection performance. Where conventional reactors might achieve similar mean doses but with wide distribution (some particles receiving excessive dose while others receive insufficient dose), the swirl reactor delivers more uniform doses across all particles, improving both treatment reliability and energy efficiency. This dual benefit of the swirl-based design represents a fundamental advancement over conventional UV reactor architectures.

#### 4.1.2 Velocity profile characteristics

Detailed velocity profiles at the reactor inlet and outlet (Figure 16) provide quantitative characterization of the swirling flow structure and its evolution through the reactor.

#### Radial Velocity Component (u):

The radial velocity profile (Figure 4-3) exhibits an asymmetric distribution with positive and negative values across the cross-section, indicating secondary flow circulation. At the reactor inlet (entry), the profile shows peak magnitudes of approximately  $\pm 0.6$  (normalized), with the positive peak occurring at  $r/R \approx 0.3$  and the negative peak at  $r/R \approx -0.4$ . This asymmetry indicates that the swirl core is displaced from the geometric centre line, a characteristic feature of swirling flows generated by asymmetric inlet geometries (vanes and elbow). The radial velocity drives secondary circulation that continuously redistributes fluid across the cross-section, enhancing mixing effectiveness.

By the reactor outlet (exit), the radial velocity magnitudes have decreased to approximately  $\pm 0.4$  (normalized), representing a 33% reduction in secondary flow intensity. However, the asymmetric pattern persists, indicating that while the secondary flows weaken, the fundamental flow structure remains throughout the reactor length. The maintenance of radial velocity components throughout the reactor ensures continuous mixing rather than the flow stratification that would occur in purely axial flow systems.

The physical significance of these radial velocities is that they continuously transport fluid particles across different radial positions, exposing them to varying UV intensity levels. In conventional axial-flow reactors, particles maintain approximately constant radial positions throughout their transit, receiving either consistently high or low UV exposure depending on their initial radial location. The radial mixing in the swirl reactor homogenizes exposure by ensuring particles sample multiple radial positions during their transit.

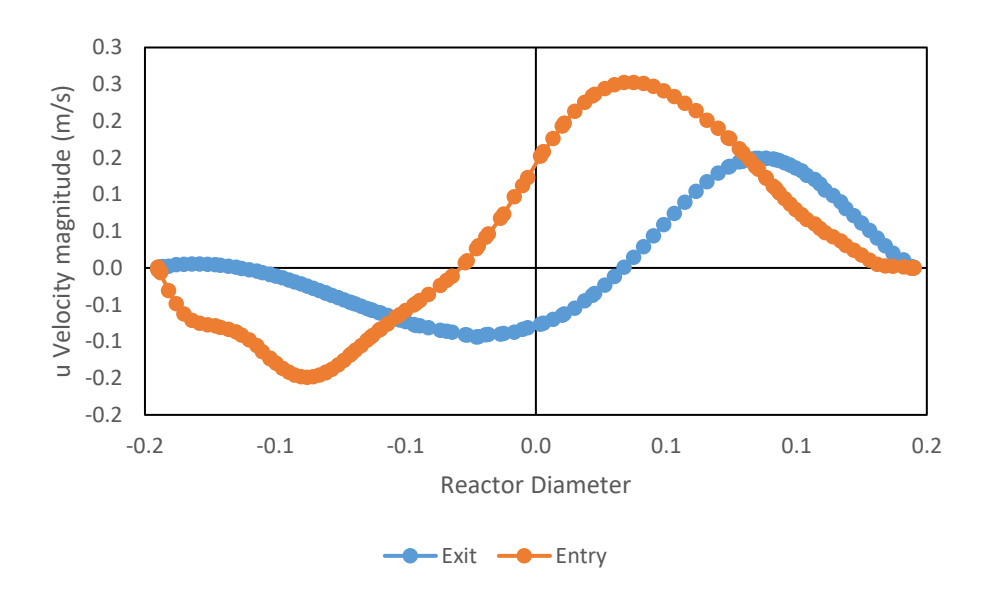


Figure 4-3: u velocity component at entry and exit point of the reactor

#### **Tangential Velocity Component (w):**

The tangential velocity profile (Figure 4-4) demonstrates the swirl intensity and its spatial distribution. At the reactor inlet, the profile exhibits a characteristic forced-vortex (solid-body rotation) pattern in the core region (|r/R| < 0.5) where tangential velocity increases approximately linearly with radius, reaching peak magnitudes of  $\pm 1.5$  (normalized) at  $r/R \approx \pm 0.6$ . The off-axis peak location (rather than at the wall) confirms the presence of a concentrated vortex core displaced from the centreline.

In the outer region (|r/R| > 0.6), the tangential velocity decreases toward the wall, approaching zero at  $r/R = \pm 1.0$  due to the no-slip boundary condition. This velocity distribution is typical of vortex flows where the core region rotates as a quasi-solid body while the outer region experiences free-vortex decay. The magnitude and distribution of tangential velocity directly determine the swirl number, which quantifies the overall swirl intensity.

At the reactor outlet, the tangential velocity magnitudes have decreased substantially to peak values of approximately  $\pm 0.8$  (normalized), representing a 47% reduction in swirl intensity. This decay of tangential momentum is expected due to viscous dissipation over the reactor length. However, significant tangential velocity persists at the outlet, confirming that swirl-induced mixing remains active throughout the entire reactor rather than occurring only near the inlet. The gradual swirl decay ensures relatively uniform mixing intensity along the reactor length, avoiding the sharp transition from highly mixed inlet conditions to stratified outlet conditions that would occur with rapid swirl breakdown.

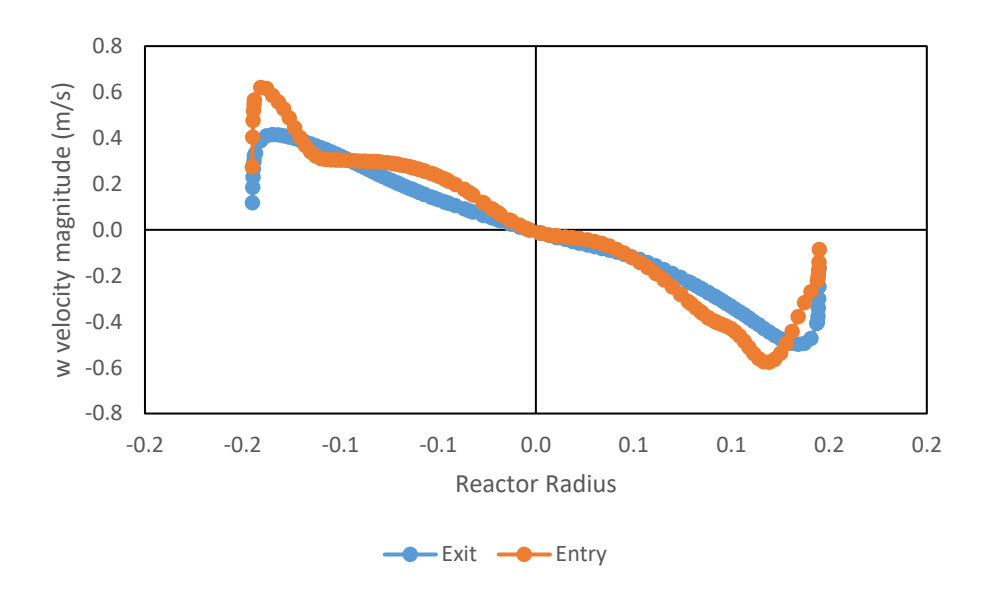


Figure 4-4: w velocity component at entry and exit point of the reactor

# **Axial Velocity Component (v):**

The axial velocity (Figure 4-5) exhibits a relatively flat distribution across the core region with steeper gradients near the wall, characteristic of turbulent pipe flow at Re = 442,909. The axial velocity maintains an approximately uniform profile from inlet to outlet with only minor variations, indicating that the bulk flow rate is preserved while the swirling motion develops and decays around this primary axial flow. The relatively uniform axial velocity distribution,

contrasting with the laminar parabolic profile, confirms fully turbulent flow conditions where turbulent eddies effectively transport momentum across the cross-section.

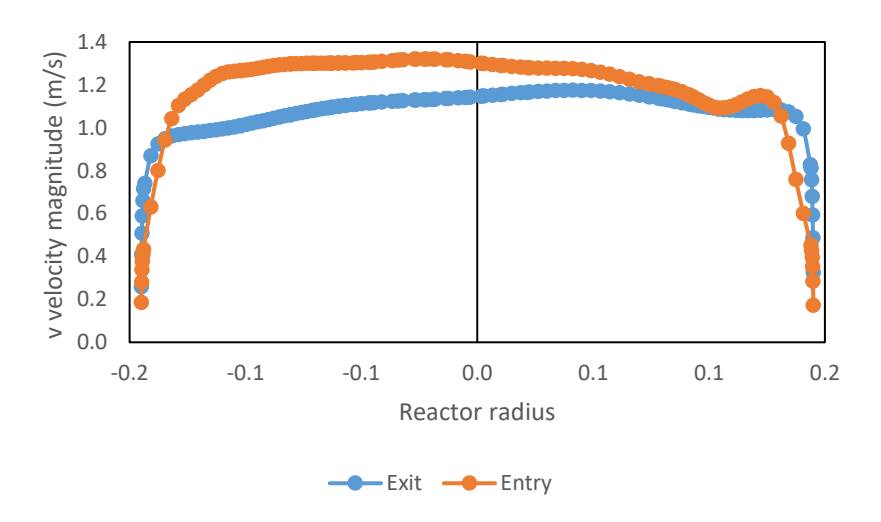


Figure 4-5: v velocity component at entry and exit point of the reactor

# 4.1.3 Swirl number analysis

The swirl number is calculated as follows:

Reactor inlet: S = 0.37

• Reactor outlet: S = 0.15

• Swirl decay: 59% reduction from inlet to outlet

The inlet swirl number of 0.37 places the flow in the moderate swirl regime (0.3 < S < 0.6), characterized by:

- Formation of a precessing vortex core rather than axisymmetric swirl
- Onset of vortex breakdown with central recirculation zone
- Enhanced turbulent mixing from vortex instabilities
- Characteristic 'S-shaped' axial velocity profiles

#### **Swirl Decay Analysis**

The 59% swirl number reduction from inlet to outlet indicates substantial but incomplete swirl dissipation over the 1.29 m reactor length. The persistence of significant swirl (S = 0.15) at the outlet ensures continuous mixing throughout the reactor rather than initial mixing followed by stratification. The swirl decay rate can be quantified as:

$$\frac{dS}{dx} = \frac{S_{outlet} - S_{inlet}}{L} = \frac{0.15 - 0.37}{1.29} = -0.17 \,\mathrm{m}^{-1} \tag{17}$$

The relatively gradual decay ensures relatively uniform mixing intensity along the reactor length. This decay rate indicates that the swirl number decreases by approximately 0.17 per meter of axial distance, representing a moderate rate of swirl dissipation that maintains effective mixing throughout the entire reactor length.

# 4.1.4 Effect of flow rate on hydraulic performance

The reactor's hydraulic performance was evaluated across a wide range of flow rates to assess operational flexibility and understand how flow conditions influence mixing effectiveness and swirl generation. Four distinct flow rates were analyzed: 12% (30 m³/h), 50% (125 m³/h), 100% (250 m³/h), and 200% (500 m³/h) of the nominal design flow rate, corresponding to Reynolds numbers ranging from 26,586 to 442,909.

#### 4.1.4.1 Reynolds Number and Swirl Number Characteristics:

Table 4-1 presents the calculated Reynolds numbers and swirl numbers at both reactor inlet and outlet for each flow rate condition. Figure 4-6 demonstrates a strong exponential relationship between Reynolds number and swirl number at both reactor inlet and outlet locations, with exceptional correlation coefficients of  $R^2$  = 0.9994 at the inlet and  $R^2$  = 0.9945 at the outlet. These near-unity  $R^2$  values confirm highly predictable swirl generation and decay behavior across the operational flow range, with the inlet correlation being slightly stronger due to the direct and consistent action of the vane swirl generator. However, at the highest flow rate (200%), the outlet swirl number deviates from the exponential trend, indicating more rapid swirl decay than predicted by the relationship established at lower flow rates.

Table 4-1: Comparison of swirl number at inlet and exit of the reactor for different flow rates

| Flow rate             | 12%    | 50%     | 100%    | 200%    |
|-----------------------|--------|---------|---------|---------|
| Reynolds number       | 26,586 | 110,727 | 221,454 | 442,909 |
| Swirl number at inlet | 0.12   | 0.21    | 0.37    | 1.51    |
| Swirl number at exit  | 0.006  | 0.07    | 0.15    | 0.92    |

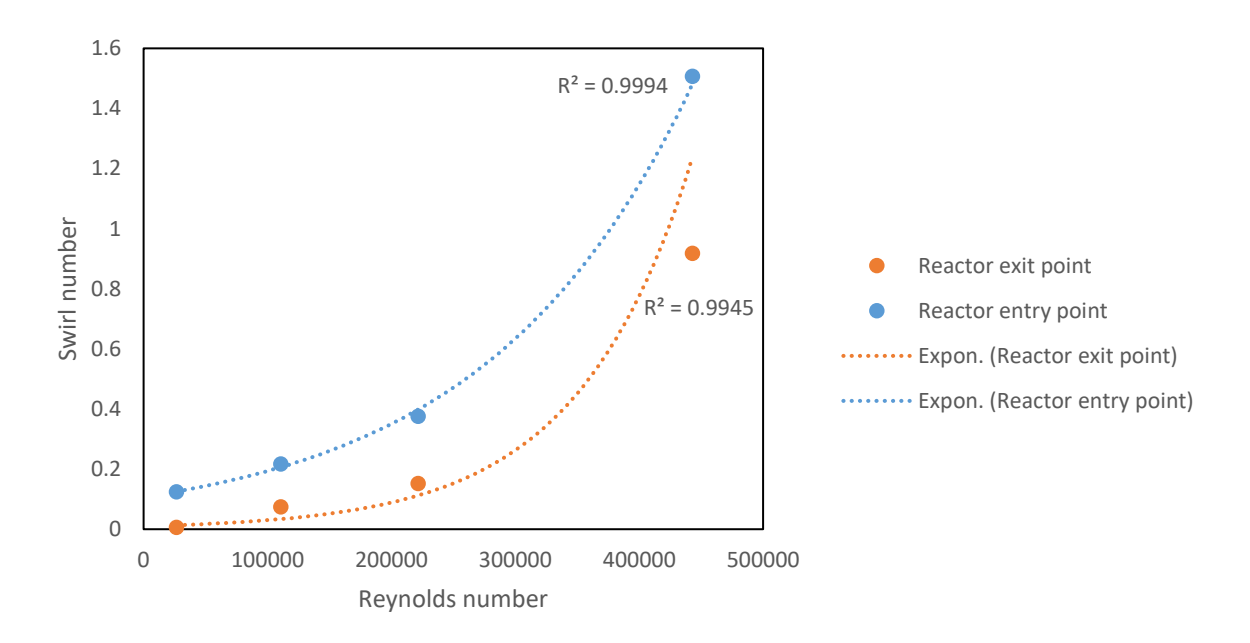


Figure 4-6: Comparison of the Reynolds number with Swirl number

At the lowest flow rate (12%), the inlet swirl number of 0.12 indicates weak swirl generation, barely above the threshold for effective mixing ( $S \approx 0.1$ ). The swirl intensity decays rapidly through the reactor to nearly zero at the outlet (S = 0.006), suggesting that viscous dissipation dominates over inertial effects at this low Reynolds number. This weak swirl regime provides minimal cross-sectional mixing enhancement beyond baseline turbulent diffusion.

As flow rate increases to 50%, the inlet swirl number rises to 0.21, entering the low-moderate swirl regime. At this condition, swirl begins to influence flow structure more substantially, though the outlet swirl number (0.07) indicates significant decay over the reactor length. The 67% swirl reduction from inlet to outlet suggests that while swirl generation is effective, the flow energy is insufficient to maintain strong swirl throughout the reactor.

At the nominal 100% flow rate, as discussed in Section 4.1.3, the inlet swirl number of 0.37 establishes moderate swirl with vortex breakdown characteristics. The outlet swirl number of 0.15 confirms sustained mixing throughout the reactor length with more gradual decay (59% reduction) compared to lower flow rates.

The most dramatic change occurs at 200% flow rate, where the inlet swirl number reaches 1.51, entering the strong swirl regime (S > 0.6). This high swirl intensity indicates intense rotational motion with potential for strong central recirculation zones and vortex breakdown.

Notably, even with significant decay (39% reduction), the outlet swirl number of 0.92 remains well within the strong swirl regime, confirming that high inertial forces maintain rotational motion despite viscous and wall friction effects.

#### 4.1.4.2 Flow Structure Development

Velocity vector visualizations at the reactor inlet and outlet reveal qualitative differences in flow structure across the flow rate range.

At 100% flow rate (Figure 4-7), the inlet velocity vectors exhibit clear spiral patterns with organized helical trajectories. The vectors maintain coherent rotational structure with identifiable swirl cores displaced from the geometric centerline. At the outlet, the swirl structure persists but with reduced tangential velocity magnitudes, consistent with the 59% swirl number reduction. The flow remains well-organized with minimal signs of flow breakdown or chaotic motion.

Velocity vector maps at entry and exit of reactor for 100% of flow rate

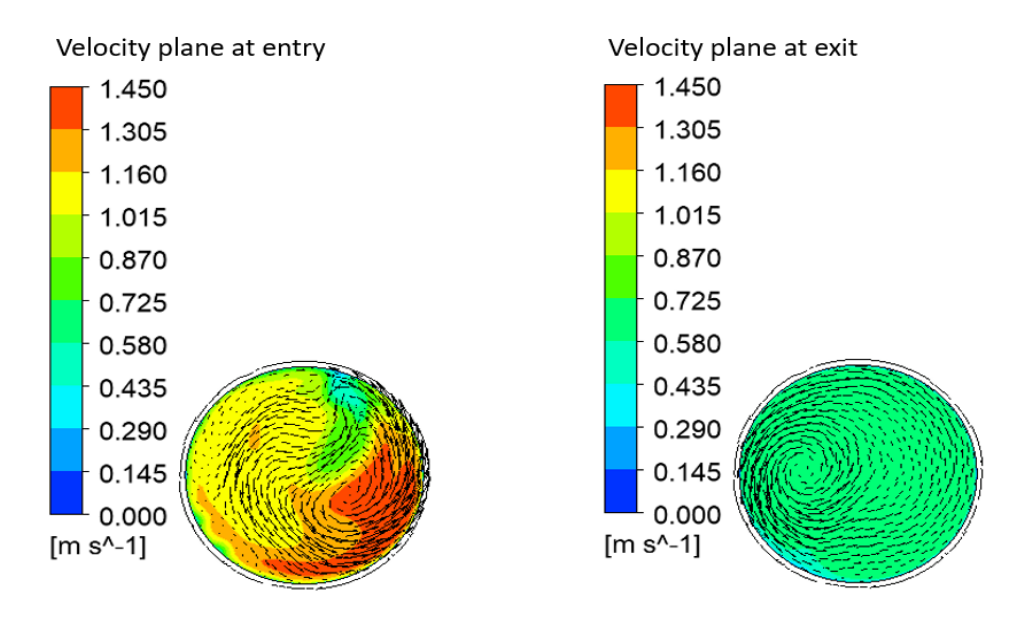


Figure 4-7: Velocity vector maps at entry and exit of the reactor for 100% flow rate

At 200% flow rate (Figure 4-8), the inlet flow structure intensifies dramatically with highly pronounced spiral patterns and strong tangential velocity components. The velocity vectors show tight helical trajectories with small pitch, indicating rapid rotation. The swirl core is more concentrated and displaced further from the centerline compared to lower flow rates. At the outlet, despite substantial swirl decay, the flow maintains strong rotational characteristics

with well-defined helical patterns. The high inertial forces at this flow rate resist dissipation, maintaining organized swirl structure throughout the reactor.

Velocity vector maps at entry and exit of reactor for 200% of flow rate

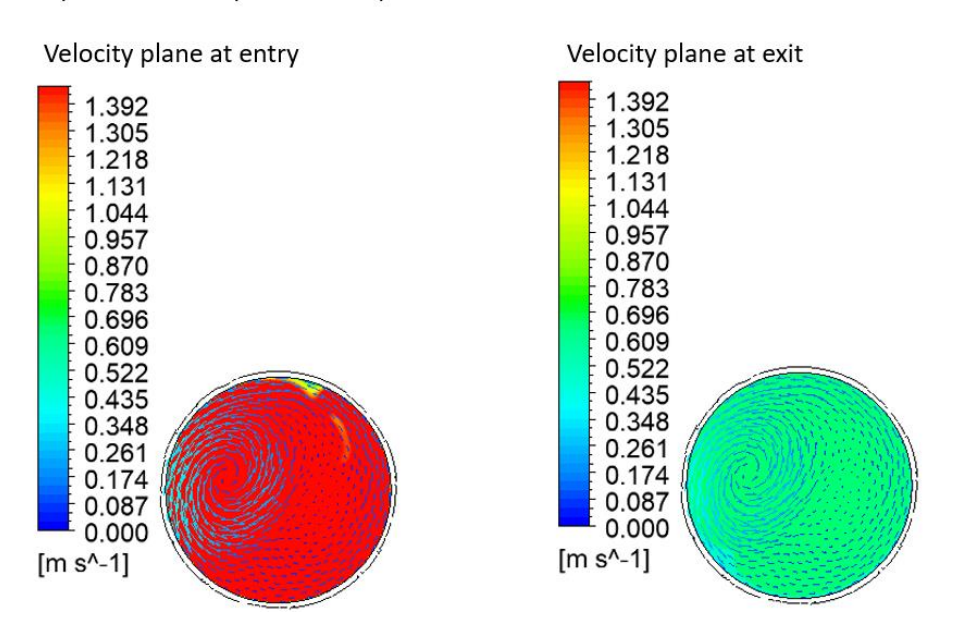


Figure 4-8: Velocity vector maps at entry and exit of reactor at 200% flow rate

At 50% flow rate (Figure 4-9), the inlet swirl patterns are less pronounced than at higher flow rates, with velocity vectors showing gentler spiral trajectories and larger pitch angles. The swirl core is less concentrated and more diffuse across the cross-section. At the outlet, the swirl has decayed substantially, with velocity vectors approaching predominantly axial orientation. The flow structure transitions from organized swirl at the inlet to weakly swirling or nearly axial flow at the outlet.

Velocity vector maps at entry and exit of reactor for 50% of flow rate

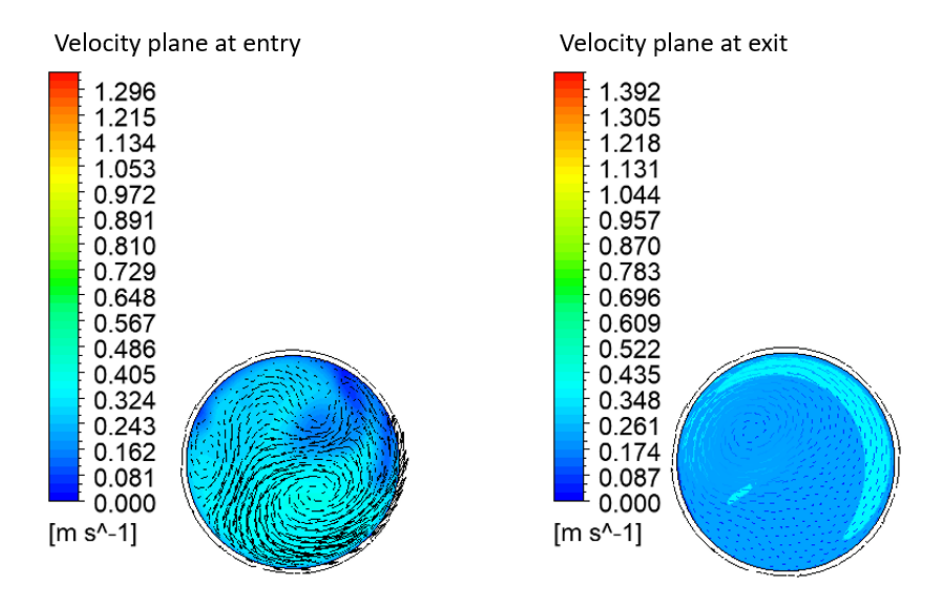


Figure 4-9: Velocity vector maps at entry and exit of reactor for 50% flow rate

At the lowest flow rate of 12% (Figure 4-10), swirl generation is minimal. The inlet velocity vectors show only slight deviations from axial flow, with weak tangential components. The flow pattern appears nearly axial with minor perturbations rather than organized helical motion. At the outlet, the swirl has dissipated almost completely (S = 0.006), resulting in essentially straight axial flow with velocity vectors aligned parallel to the pipe axis. This flow regime provides minimal mixing enhancement beyond what would occur in straight pipe flow without vanes.

Velocity vector maps at entry and exit of reactor for 10% of flow rate

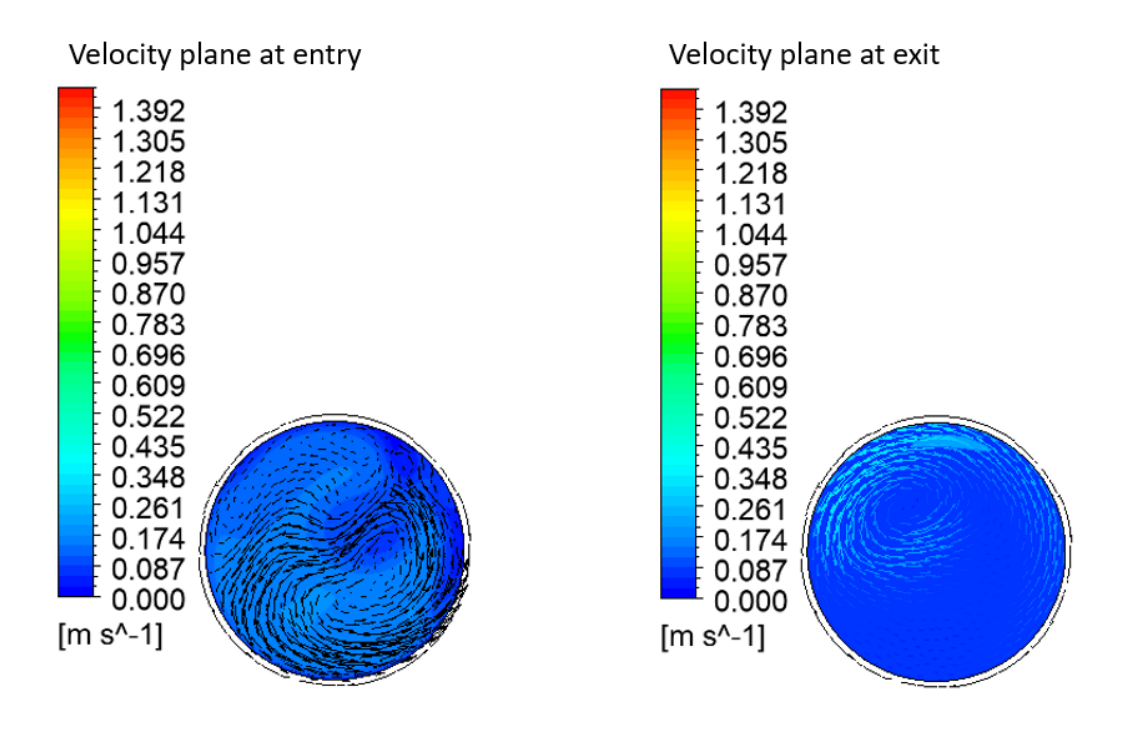


Figure 4-10: Velocity vector maps at entry and exit of reactor at 10% flow rate

# 4.2 UV dose

The integration of CFD flow field predictions with the optical UV irradiance model enables comprehensive analysis of UV dose distribution within the reactor and assessment of overall treatment performance. This section presents the dosage characteristics under various operating conditions, examining the influence of flow rate, UV transmittance (UVT), and LED configuration on treatment efficacy.

# 4.2.1 Baseline Dosage Distribution at Design Flow Rate

The UV dose distribution at the nominal 100% flow rate (250 m<sup>3</sup>/h) with 98% UVT provides baseline characterization of reactor performance. Figure 4-11 illustrates the optical irradiance field within the reactor, showing (a) the irradiance pattern from a single LED unit and (b) the cumulative irradiance from all 1000 LEDs arranged in 50 rings around the reactor periphery.

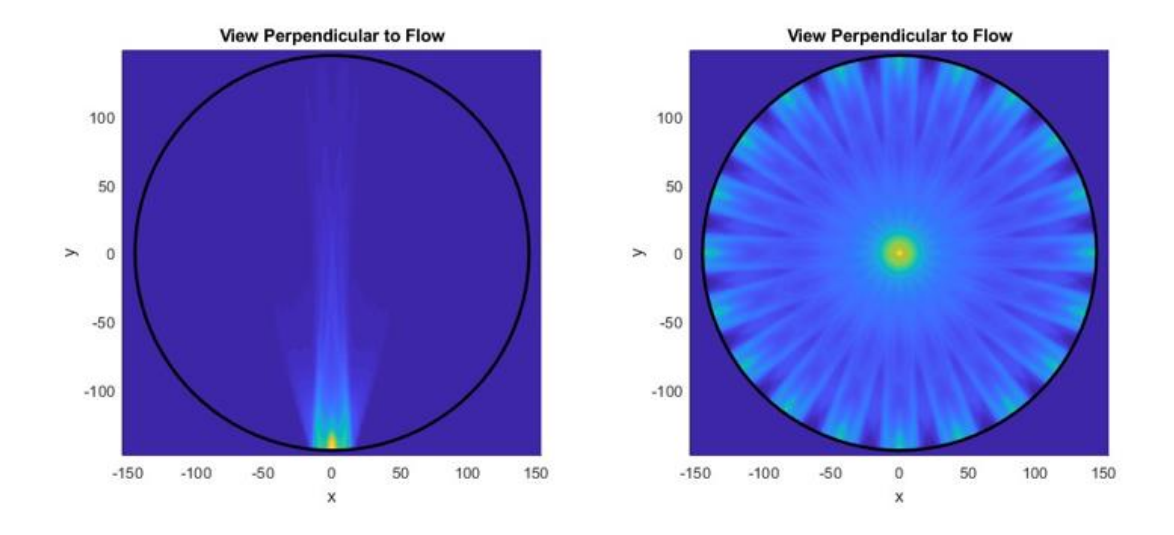


Figure 4-11 : a) Optical flow for a single LED b) Optical flow for all the LEDs

Figure 4-12 presents cross-sectional views of the UV dose (irradiance) distribution within the reactor. The fluence field exhibits moderate radial gradients, with intensity highest at  $r/R \approx 0.4$ -0.6 (40-60% of radius from centerline) where LED beams converge, and lower near both the centerline and outer wall. This non-uniform irradiance distribution is inherent to peripheral LED arrangements and differs fundamentally from mercury lamp reactors where lamps positioned within the flow create highest irradiance near the lamp surfaces.

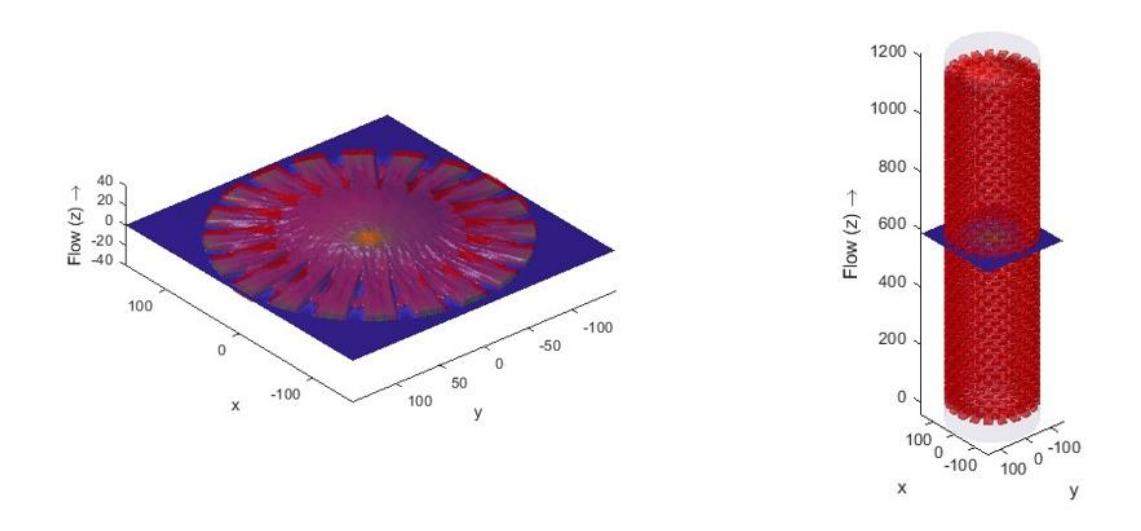


Figure 4-12: a) Fluence within the reactor for single cross section b) Cross section presented of the reactor

The critical role of swirl-induced mixing becomes evident when considering this irradiance distribution. Without cross-sectional mixing, water particles following straight axial paths

would receive UV doses dependent solely on their radial position, resulting in wide dose variation. The swirling flow continuously redistributes particles across radial positions, exposing each particle to varying irradiance levels and homogenizing the cumulative dose distribution.

Figure 4-13 presents the Reduction Equivalent Dose (RED) distribution for MS2 bacteriophage at 100% flow rate and 98% UVT. The RED represents the minimum UV dose that 90% of the water receives, providing a conservative measure of treatment efficacy. The calculated RED value of 36.7 mJ/cm<sup>2</sup> at these conditions exceeds the typical 4-log inactivation requirement for Crypto (approximately 20 mJ/cm<sup>2</sup>), confirming adequate treatment capacity.

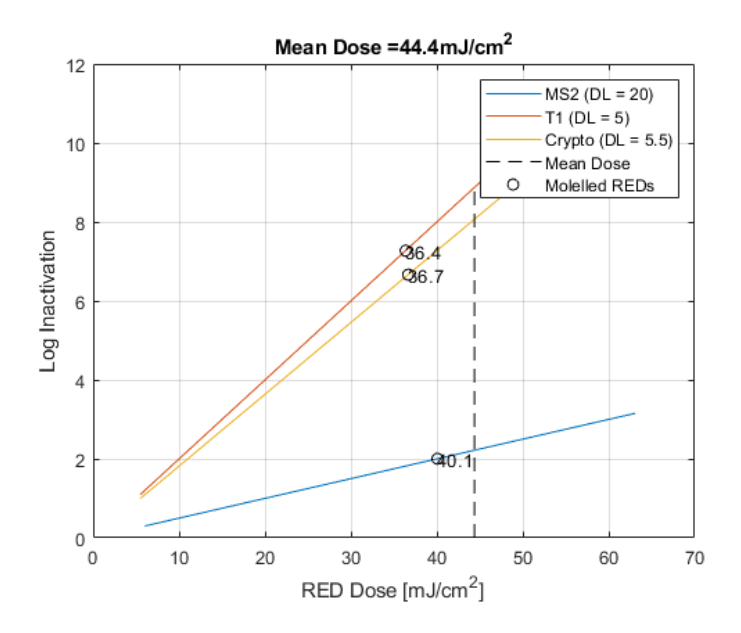


Figure 4-13: RED dosage received by the water at 100% flow rate

### 4.2.2 Influence of UV Transmittance on Dosage

UV transmittance (UVT) quantifies the fraction of UV light transmitted through a 1 cm path length of water, representing the combined effects of absorption and scattering by dissolved organic matter, suspended particles, and other constituents. UVT varies widely in practice: drinking water typically exhibits 95-98% UVT, while treated wastewater may have 70-85% UVT, and raw water sources can show even lower values [15], [72], [88].

Figure 4-14 presents the exponential relationship between UVT and UV dose at constant flow rate (100%) and LED power. The dosage increases exponentially with UVT, rising from approximately 7 mJ/cm<sup>2</sup> at 85% UVT to 30 mJ/cm<sup>2</sup> at 98% UVT. This exponential behavior follows directly from the Beer-Lambert law

The critical finding from Figure 4-14 is that a UVT reduction from 98% to 85% results in an 80% decrease in UV dose delivered to the water. This dramatic sensitivity highlights the importance of maintaining high water quality at the reactor inlet. Pre-treatment processes that improve UVT provide direct and substantial benefits to UV reactor performance, potentially reducing LED power requirements by factors of 3-5 for achieving equivalent dosage at lower UVT conditions.

The exponential fit ( $R^2 > 0.99$ ) confirms that the integrated CFD-optical model accurately captures Beer-Lambert absorption physics across the full UVT range. This predictive capability enables reactor sizing and LED power specification for diverse water quality conditions without requiring extensive experimental validation at each UVT level.

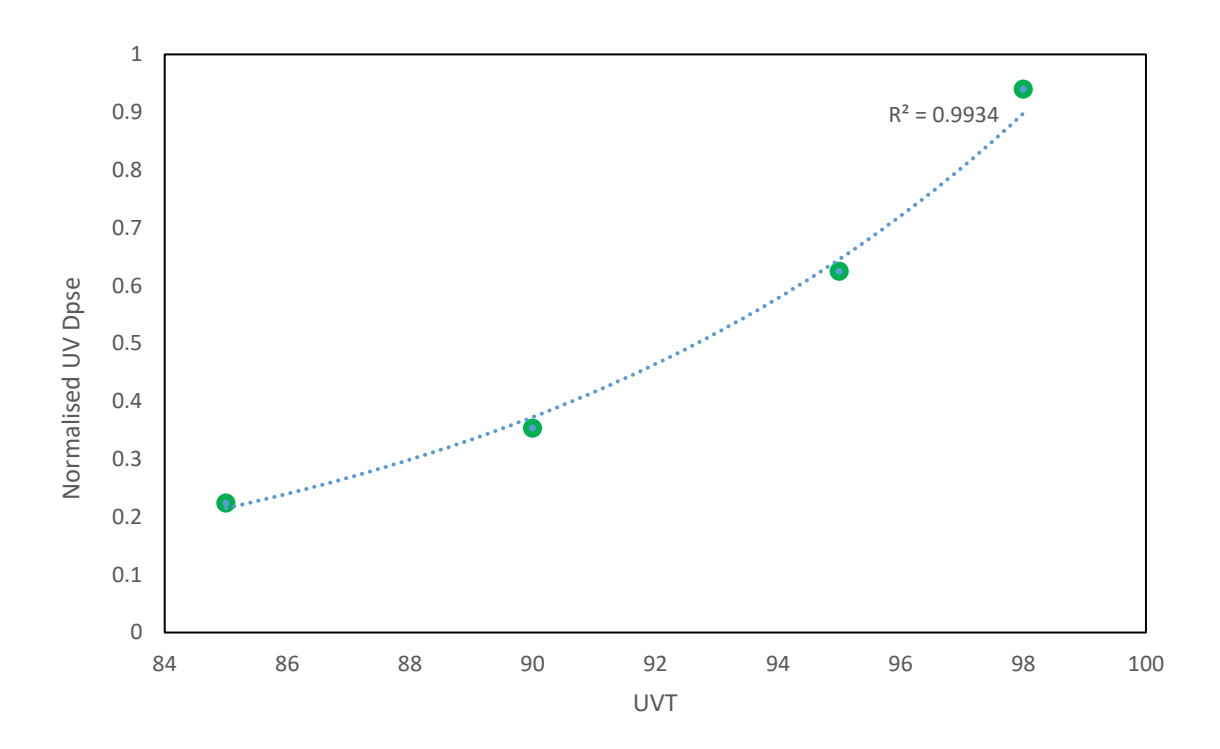


Figure 4-14: Comparison of the normalised UV dose vs UVT

# 4.2.3 Effect of Flow Rate on UV dose Delivery

The relationship between flow rate and UV dose delivery was analysed across a range of operating conditions by varying LED power and UVT values. The analysis reveals that dosage delivery can be characterized by the ratio of LED power to flow rate (LED/Q), which serves as a key operational parameter for reactor performance prediction and control.

Figure 4-15 present the relationship between LED power-to-flow-rate ratio and delivered MS2

dosage at three UVT levels (73%, 88%, and 98%). At all three water quality conditions, the

relationship is strongly linear with exceptional correlation coefficients:

• **UVT 73%**: R<sup>2</sup> = 0.998

**UVT 88%**: R<sup>2</sup> = 1

**UVT 98%**: R<sup>2</sup> = 0.9878

These near-unity correlation coefficients confirm that UV dose delivery is highly predictable

across the operational flow range tested (30-250 m<sup>3</sup>/h). The linear relationship indicates that

the reactor maintains consistent optical and hydraulic performance across flow rates

spanning nearly an order of magnitude, with no evidence of performance degradation or

efficiency loss at either extreme of the operating range.

The linearity of these relationships has important practical implications. For a given water

quality (UVT), flow rate and target dosage requirement, the necessary LED power can be

calculated directly from the desired flow rate without requiring iterative optimization or

experimental validation at each operating condition. This predictability simplifies reactor

control system design and enables confident performance specification during system sizing

and procurement.

83

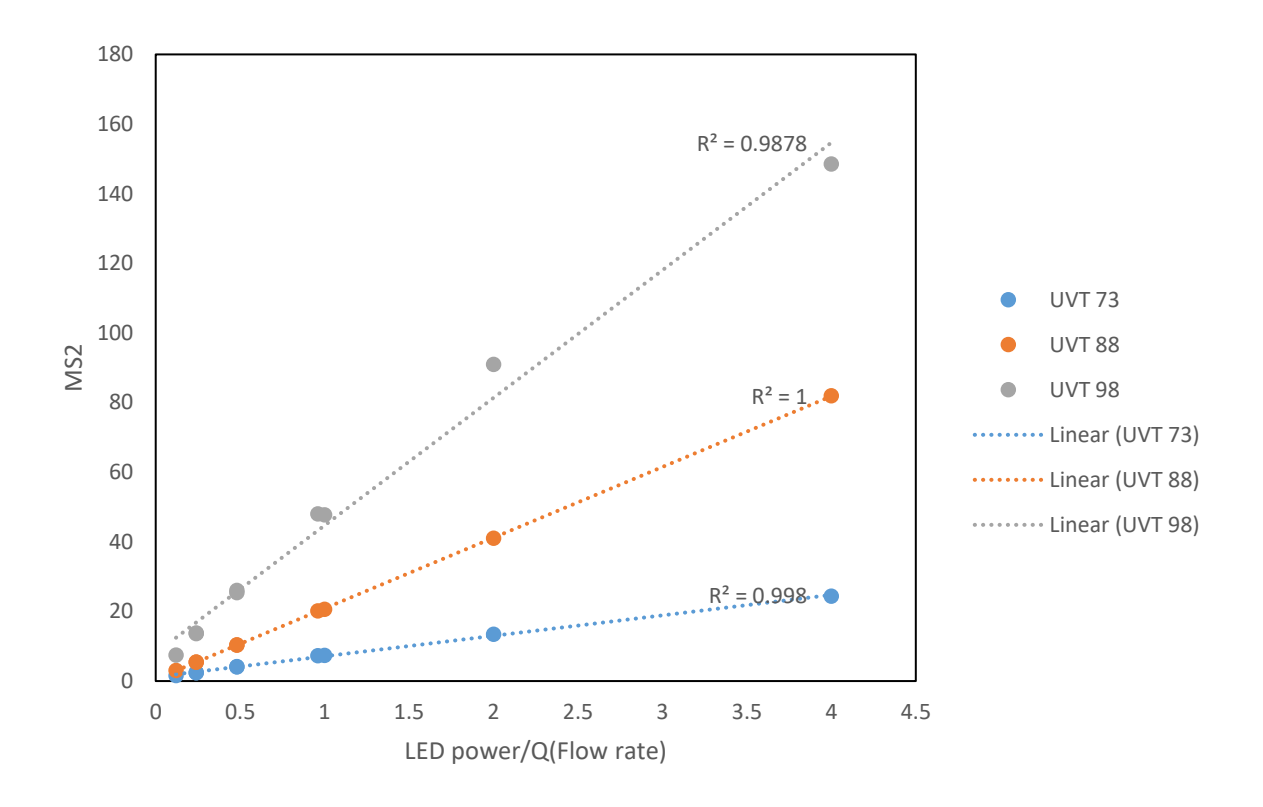


Figure 4-15: Relationship between LED power, Flow rate and MS2 RED

Figure 4-16 presents the relationship between UVT and required LED power-to-flow-rate ratio for maintaining constant MS2 dosage. While only three data points are available (corresponding to the three UVT levels tested), the trend suggests an inverse relationship between UVT and power requirement. A linear fit to these three points yields R² = 0.9281, though this correlation should be interpreted cautiously given the limited data. This dramatic sensitivity demonstrates that achieving the same UV dose at 73% UVT requires approximately 8.3× higher LED power compared to 98% UVT, even a moderate water quality decline from 98% to 88% UVT necessitates a 2× increase in LED power to maintain equivalent dosage delivery underscoring the critical importance of pre-treatment for water quality improvement. These results emphasize the necessity of continuous UVT monitoring at the reactor inlet to enable real-time LED power or flow rate adjustment, ensuring that the required dosage is consistently delivered across varying water quality conditions while minimizing energy consumption during periods of higher UVT.

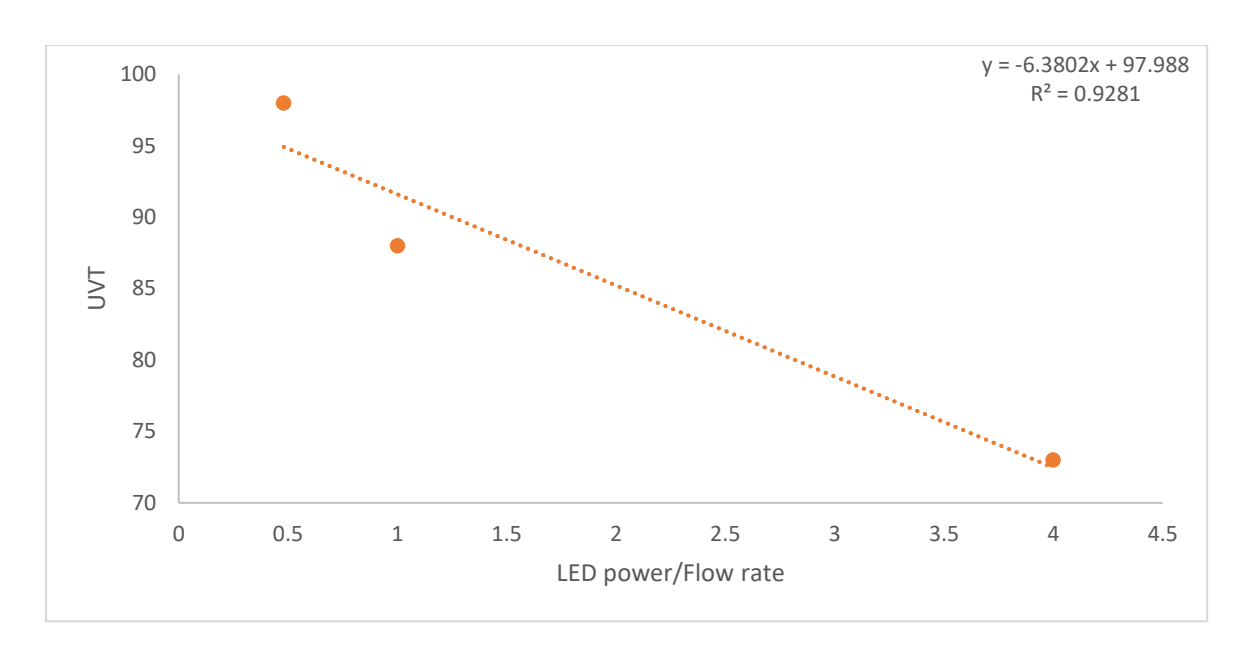


Figure 4-16: Relationship between UVT, LED power and Flow rate

# 4.2.4 Effect of LED Ring Configuration on Reactor Performance

The baseline reactor design incorporates 50 LED rings (1000 total LEDs at 20 per ring) distributed over the 1.29 m reactor length. To assess the sensitivity of performance to LED quantity and distribution, configurations with reduced LED ring counts (30 rings = 600 LEDs, and 10 rings = 200 LEDs) were analyzed at constant LED power per unit (maintaining total power proportional to LED count).

Figure 4-17, Figure 4-18 and Figure 4-19 present the relationship between LED power-to-flow-rate ratio and MS2 dosage for 10, 30, and 50 ring configurations at three UVT levels (73%, 88%, and 98%). At all UVT conditions, the 50-ring configuration demonstrates the highest dosage delivery efficiency (steepest slope), followed by 30 rings, with the 10-ring configuration showing substantially lower efficiency.

The dosage delivery efficiency varies significantly with LED ring configuration and water quality, as summarized in Table 4-2. The 50-ring configuration (1000 LEDs) consistently demonstrates the highest efficiency across all UVT conditions, delivering 5.0-6.0 times more dosage per unit LED power-to-flow-rate ratio compared to the sparse 10-ring configuration (200 LEDs). The 30-ring configuration (600 LEDs) achieves approximately 55-60% of the 50-ring performance while using only 60% of the LED count. Notably, the efficiency advantage of denser LED distributions becomes more pronounced at lower water quality, with the 50:10 ring ratio increasing from 5.0× at 98% UVT to 6.0× at 73% UVT.

Table 4-2: Dosage Delivery Efficiency Comparison for Different LED Ring Configurations

| UVT (%) | 50 Rings Slope | 30 Rings Slope | 10 Rings Slope | Efficiency Ratio |
|---------|----------------|----------------|----------------|------------------|
|         |                |                |                | (50:30:10)       |
| 73      | 5.8754         | 3.3068         | 0.9773         | 6.0 : 3.4 : 1.0  |
| 88      | 20.318         | 11.553         | 3.6414         | 5.6:3.2:1.0      |
| 98      | 36.653         | 21.838         | 7.2703         | 5.0 : 3.0 : 1.0  |

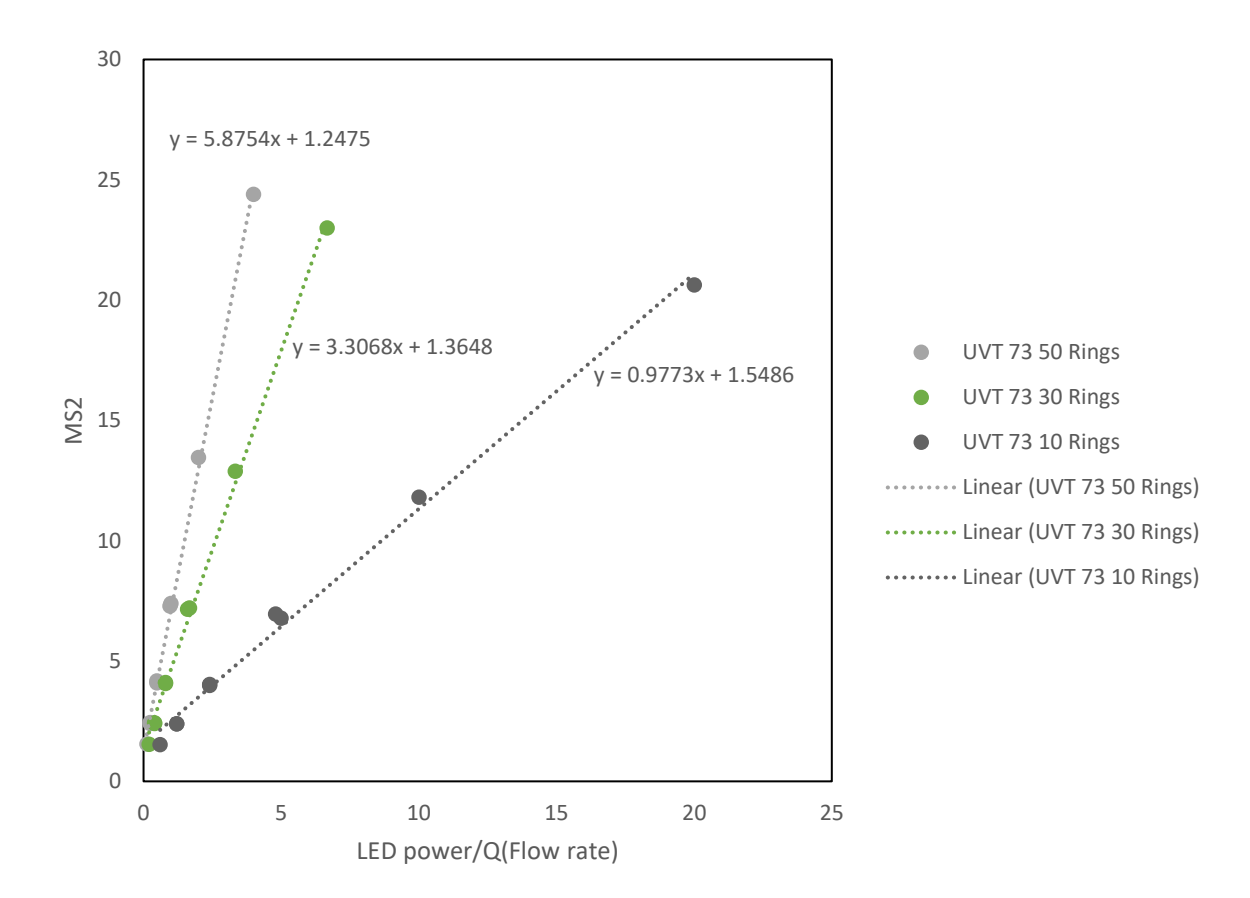


Figure 4-17: Comparison for the number of LED rings for the ratio of LED power and flow rate with MS2 dosage at 73 UVT

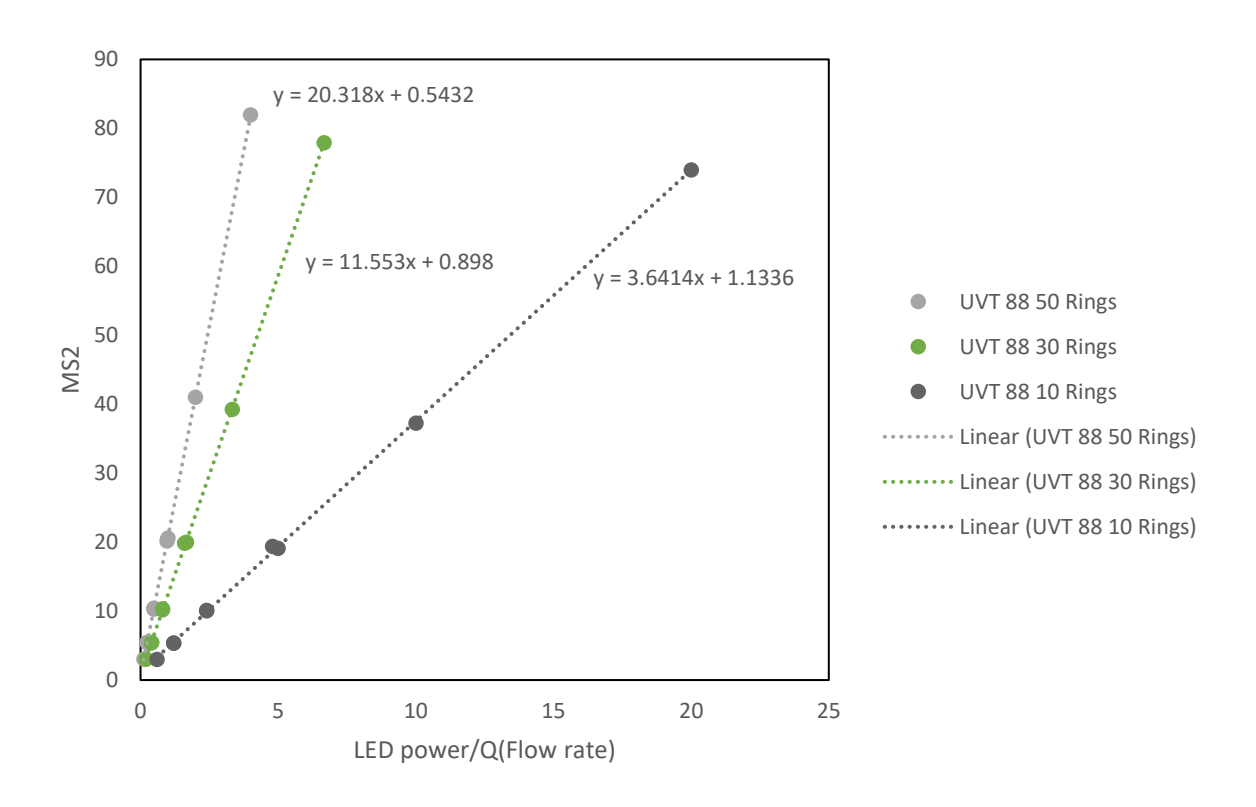


Figure 4-18: Comparison for the number of LED rings for the ratio of LED power and flow rate with MS2 dosage at 88 UVT

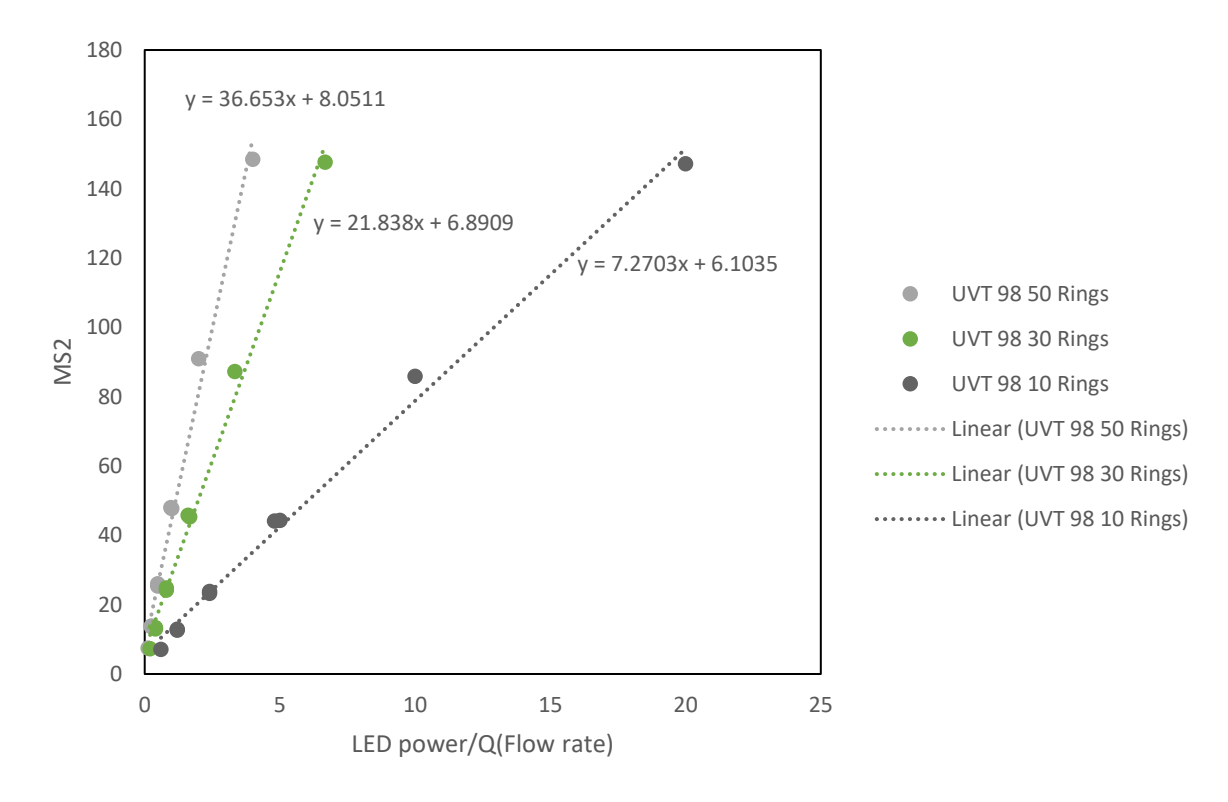


Figure 4-19: Comparison for the number of LED rings for the ratio of LED power and flow rate with MS2 dosage at 98 UVT

Figure 4-20 presents the exponential relationship between UVT and MS2 dosage for the three LED ring configurations at a constant LED power-to-flow-rate ratio of 0.48 W/(m³/h). All three configurations exhibit the characteristic exponential increase in dosage with improving water

quality. However, the magnitude of dosage delivered differs substantially between configurations, with the 50-ring system achieving considerably higher dosage than the 10-ring system across the entire UVT range (73-98%). At 98% UVT, the 50-ring configuration delivers approximately 27 mJ/cm², compared to 13 mJ/cm² for 30 rings and 6 mJ/cm² for 10 rings. The relative performance gap between configurations remains approximately constant across UVT levels.

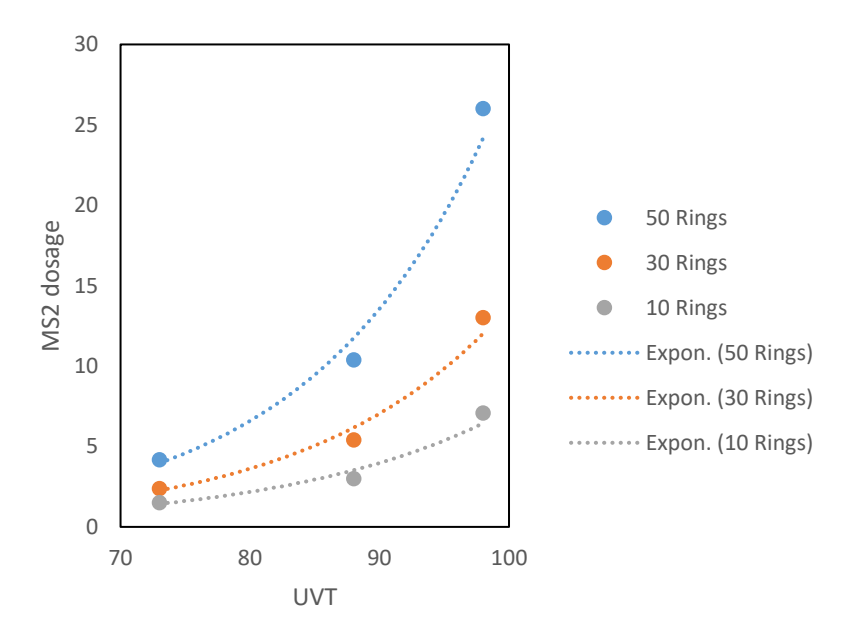


Figure 4-20: Comparison of UVT vs MS2 dosage for different number of LED rings

# 4.3 Effect of Geometric Configuration on Reactor Performance

The modular design of the UV LED water treatment system requires integration of multiple components including the reactor, swirl generation elements (stationary vanes and elbow), heat exchanger, and various pipe connections. This section examines how different geometric configurations and component arrangements influence hydraulic performance and UV dose delivery. Understanding these effects is essential for installation flexibility, system optimization, and adaptation to site-specific constraints in commercial applications.

# 4.3.1 Impact of Heat Exchanger

The UV LED system requires active thermal management to maintain LED junction temperatures within the optimal operating range (typically <85°C) for maximum output and longevity. A liquid cooling system with heat exchanger coils is integrated into the reactor assembly for this purpose. To assess whether heat exchanger presence and position influence

reactor hydraulic performance and UV dose delivery, comparative CFD simulations were conducted for two configurations: full assembly with upstream heat exchanger, and reactor assembly without heat exchanger. Both configurations maintained identical reactor, vane, and elbow geometry to isolate the heat exchanger effect.

Figure 4-21 presents the comparison of UV dose versus UVT for both configurations across the range of 85-98% UVT. The results demonstrate negligible difference in dosage delivery between the two configurations. This insensitivity confirms that the heat exchanger, when positioned upstream of the reactor, does not significantly influence the flow conditions within the UV exposure zone where dosage accumulation occurs.

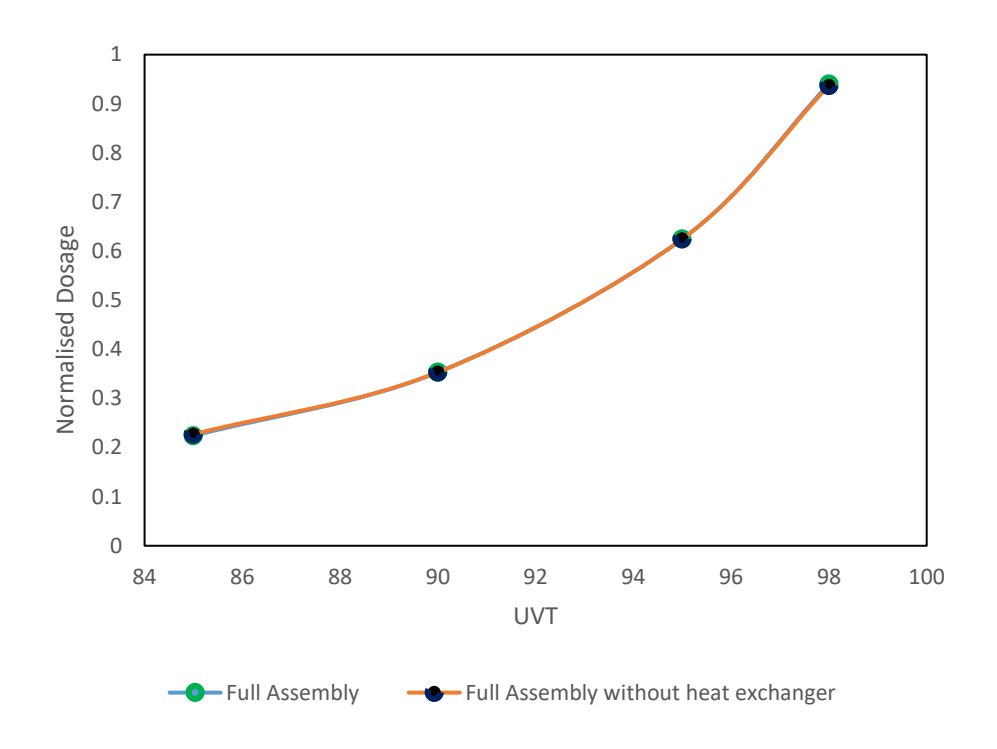


Figure 4-21: Comparison of UV dose against UVT for both with and without heat exchanger

# 4.3.2 Role of Individual Components in Flow Development and Mixing

Understanding the individual and combined contributions of geometric components to reactor performance is essential for design optimization and future system development. While the full assembly configuration has been extensively analysed in previous sections, systematic deconstruction of the system enables identification of critical design features that must be preserved versus those offering flexibility for cost reduction or installation adaptation. This analysis addresses fundamental questions: Are stationary vanes necessary, or could simpler elbow-only configurations achieve adequate mixing? What performance

penalties result from component omission? Such insights guide development of reactor variants for different applications where cost, pressure drop, or installation constraints may favour simplified designs. Three progressively simplified configurations were analysed to isolate component contributions:

- Reactor only (no upstream mixing elements)
- Reactor with elbow (passive flow turning without vanes)
- Full assembly (engineered swirl generation via vanes and elbow)

#### Flow Structure Characterization:

Figure 4-22 presents streamline visualizations revealing dramatic qualitative differences in flow structure across configurations. The reactor-only configuration exhibits perfectly parallel streamlines characteristic of fully-developed turbulent pipe flow, lacking any rotational motion or organized secondary flows. Water particles follow straight axial paths from inlet to outlet, with cross-sectional mixing occurring solely through turbulent diffusion. This represents the baseline performance achievable without engineered flow conditioning.

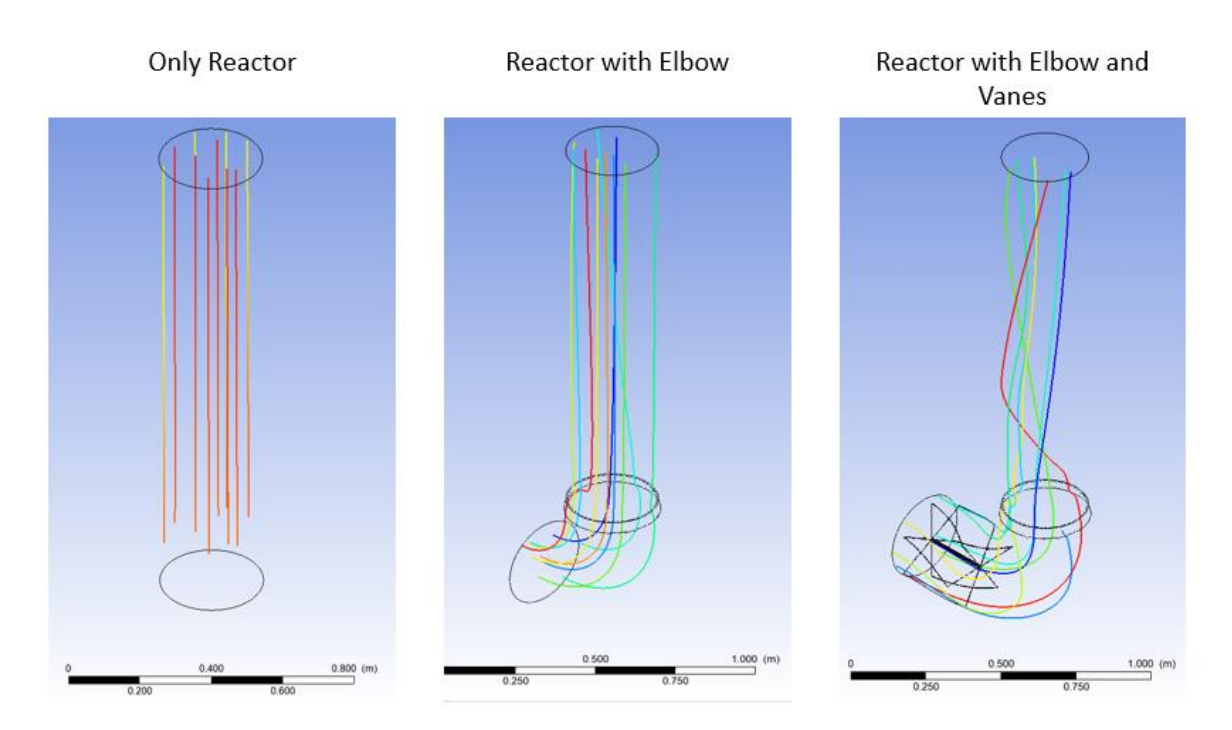


Figure 4-22: Streamline presentation for the three different configuration of the reactor

The reactor with elbow configuration shows modest streamline deviation from axial paths, indicating weak secondary flows induced by the 90° flow turning. However, the streamlines lack the organized helical structure characteristic of true swirling flow, instead exhibiting

irregular perturbations that dissipate within a few pipe diameters. This configuration demonstrates that simple geometric features (elbows, bends) commonly present in piping systems provide minimal mixing enhancement beyond baseline turbulence.

The full assembly configuration exhibits pronounced helical streamlines with multiple rotations through the reactor length, confirming sustained organized swirl throughout the UV exposure zone. The contrast with the simpler configurations is striking: the same reactor geometry produces fundamentally different flow physics depending on upstream flow conditioning.

#### **Quantitative Flow Metrics**

Table 4-3 quantifies swirl intensity via swirl number calculations at the reactor inlet. The progression from S = 0 (reactor only) to S = 0.009 (with elbow) to S = 0.37 (full assembly) reveals that stationary vanes contribute >97% of the swirl generation, with the elbow providing minimal enhancement (<3%). This finding has critical design implications: attempting to achieve adequate mixing through elbow-only configurations is fundamentally flawed, as elbows generate weak, disorganized secondary flows rather than coherent swirl.

Table 4-3: Comparison of swirl intensities for different configuration

| Type of Reactor       | Reactor only | Reactor with Elbow | Full Reactor |
|-----------------------|--------------|--------------------|--------------|
| Reynolds number       | 138,400      | 190,500            | 221,454      |
| Swirl number at inlet | 0            | 0.009              | 0.37         |

#### **UV** dose

The Figure 4-23 and Figure 4-24 below shows the Maximum and Mean dosage received by the three configurations. The value of the dosage is normalised to understand the impact of each of the configuration on the dosage received by the water. The maximum dosage shows significant difference between all three configurations. The reactor only shows the highest maximum dosage received followed by the reactor with elbow while the full assembly shows the lowest value for the maximum dosage received. All three configuration shows an exponential increase in the maximum dosage received with increase in UVT values. At the UVT of 98% the normalised dosage received by the full assembly is 0.4 of the maximum dosage received by the water with reactor only configuration. In contrast the mean dosage

graph shows very similar performance for all three configurations. The mean dosage value for all three configurations across UVT are very similar. Similar to the above there is exponential rise in the mean dosage received with increase in UVT values.

This is an interesting pattern where there is difference in the maximum dosage received by the water while the mean dosage remains consistent. This suggests that the full assembly configuration while reducing the peak dosage values maintains the overall treatment efficiency to the other configuration. There is more uniform distribution of the dosage in the full assembly which shows better mixing and more consistent treatment of water which is more desirable compared to the other configuration.

The cross-sectional visualization of dosage patterns within the reactor provides further evidence of these characteristics as shown in the Figure 4-25. The reactor-only configuration exhibits dosage concentration at the reactor's center with radial decrease in intensity. The elbow configuration maintains a similar pattern but introduces some radial distribution of dosage. The full assembly demonstrates asymmetric distribution with visible swirling patterns, resulting in more widespread and larger areas of median dosage compared to the other configurations. While the reactor-only design achieves the highest maximum dosage, the full assembly configuration provides superior mixing and more uniform water treatment distribution.

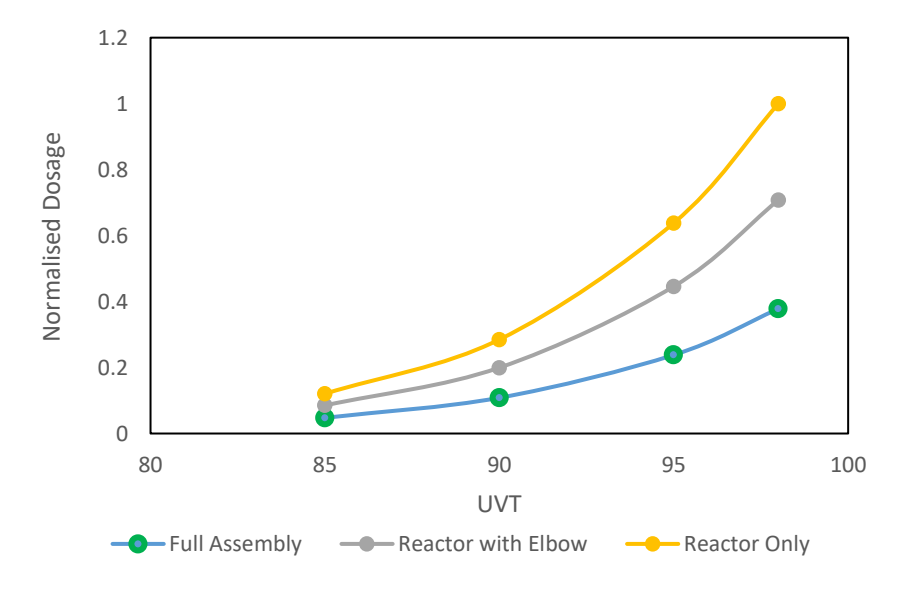


Figure 4-23: Maximum dosage received by the water for reactor only, reactor with elbow and full assembly configuration

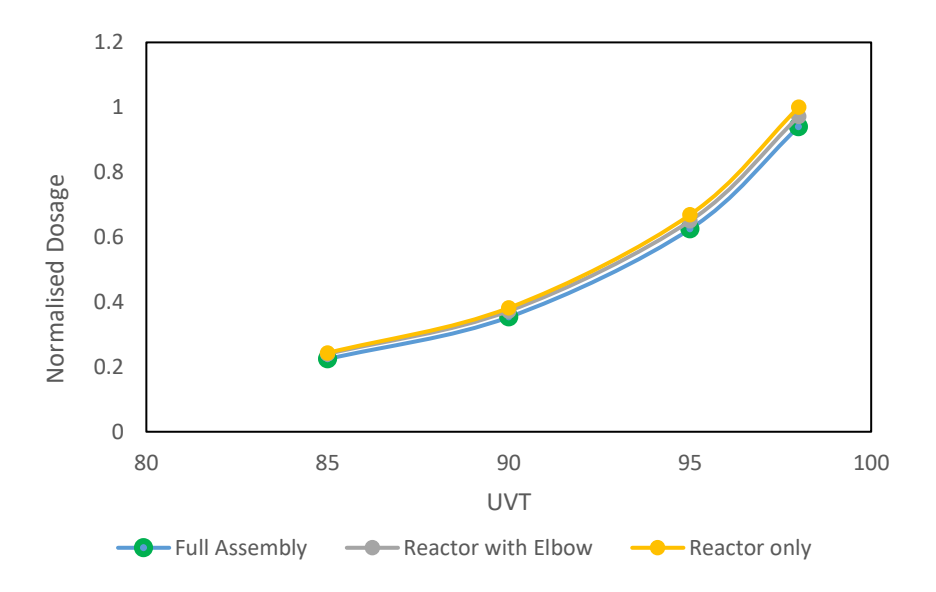


Figure 4-24: Mean dosage received by the water for reactor only, reactor with elbow and full assembly configuration

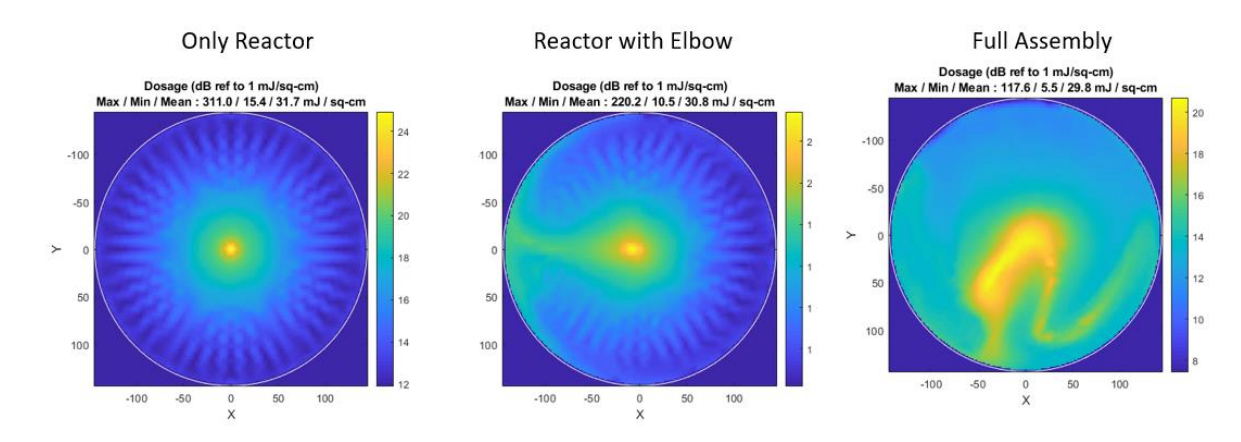


Figure 4-25: Dosage distribution for Maximum dosage received by the water for reactor only, reactor with elbow and full assembly configuration

# 4.3.3 Effect of Upstream Piping Configuration on Reactor Performance

Commercial UV reactor installations must accommodate diverse piping layouts dictated by site-specific constraints including available space, connection to existing infrastructure, and integration with upstream treatment processes. Understanding how different inlet configurations affect reactor performance is essential for ensuring consistent treatment across varied installation scenarios and for providing installation flexibility without requiring site-specific validation testing.

Six common upstream configurations representing typical installation scenarios were analysed:

Upstream U

- Upstream Elbow
- Upstream TEE
- Upstream Reducer DN300 to DN150
- Upstream Reducer DN300 to DN200
- Upstream Reducer DN300 to DN250

Figure 4-26 and Figure 4-27 illustrate the upstream piping arrangements analysed. All configurations maintained identical downstream geometry (stationary vanes, elbow, reactor) to isolate the effect of inlet conditions on performance.

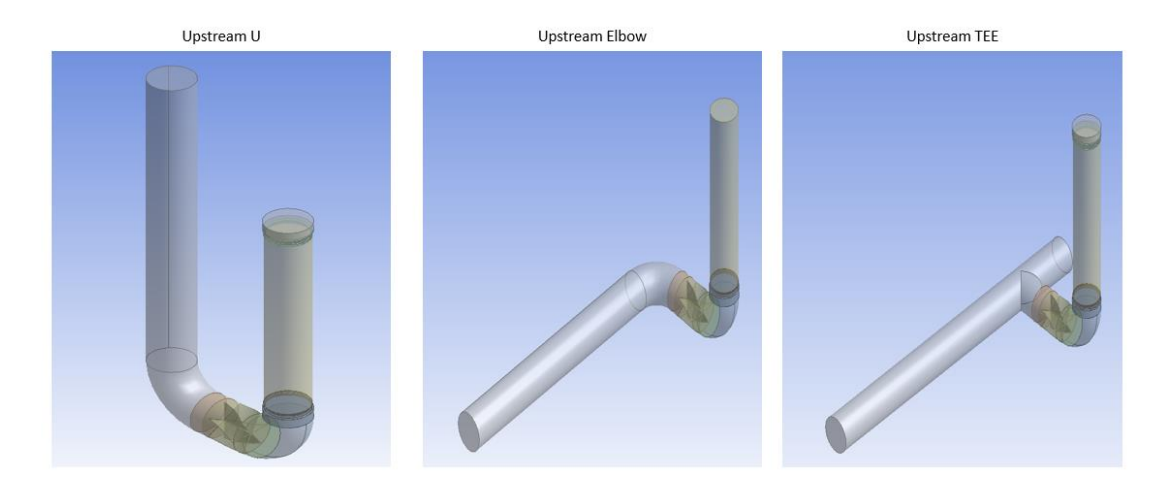


Figure 4-26: Geometrical representation of the changes to the upstream components - Upstream U, Upstream Elbow and Upstream TEE



Figure 4-27: Geometrical representation of the changes to the upstream components - Upstream reducer DN300 to DN150, DN300 to DN200 and DN300 to DN 250

#### **Flow Characteristics**

Velocity profile analysis at the reactor inlet reveals the effectiveness of the swirl generator in homogenizing flow regardless of upstream conditions. Figure 4-28 present normalized velocity components (u, v, w) as functions of radial position for all upstream configurations, revealing remarkable consistency despite dramatically different inlet geometries.

The radial velocity component (u) shows all configurations producing similar asymmetric profiles with peak magnitudes of and consistent spatial distributions. While minor differences exist, the upstream elbow shows a slightly more pronounced negative peak, these variations are within the range expected from turbulent fluctuations and mesh resolution differences. The U-bend and T-junction configurations, despite their complex inlet flow fields with potential separation zones, produce u-profiles nearly indistinguishable from the baseline straight pipe configuration.

The axial velocity component (v) demonstrates even stronger consistency, with all configurations showing nearly identical profiles characterized by relatively flat core velocity and steep near-wall gradients. The tangential velocity component (w) exhibits the characteristic oscillatory pattern indicative of swirl with off-center vortex core, and this pattern is consistent across configurations with different central axis of rotation.

The insensitivity to upstream configuration arises from the strong flow conditioning imposed by the stationary vanes. The vanes redirect the entire flow through fixed angles, imparting tangential velocity components that overwhelm any weak secondary flows or asymmetries present in the inlet flow.

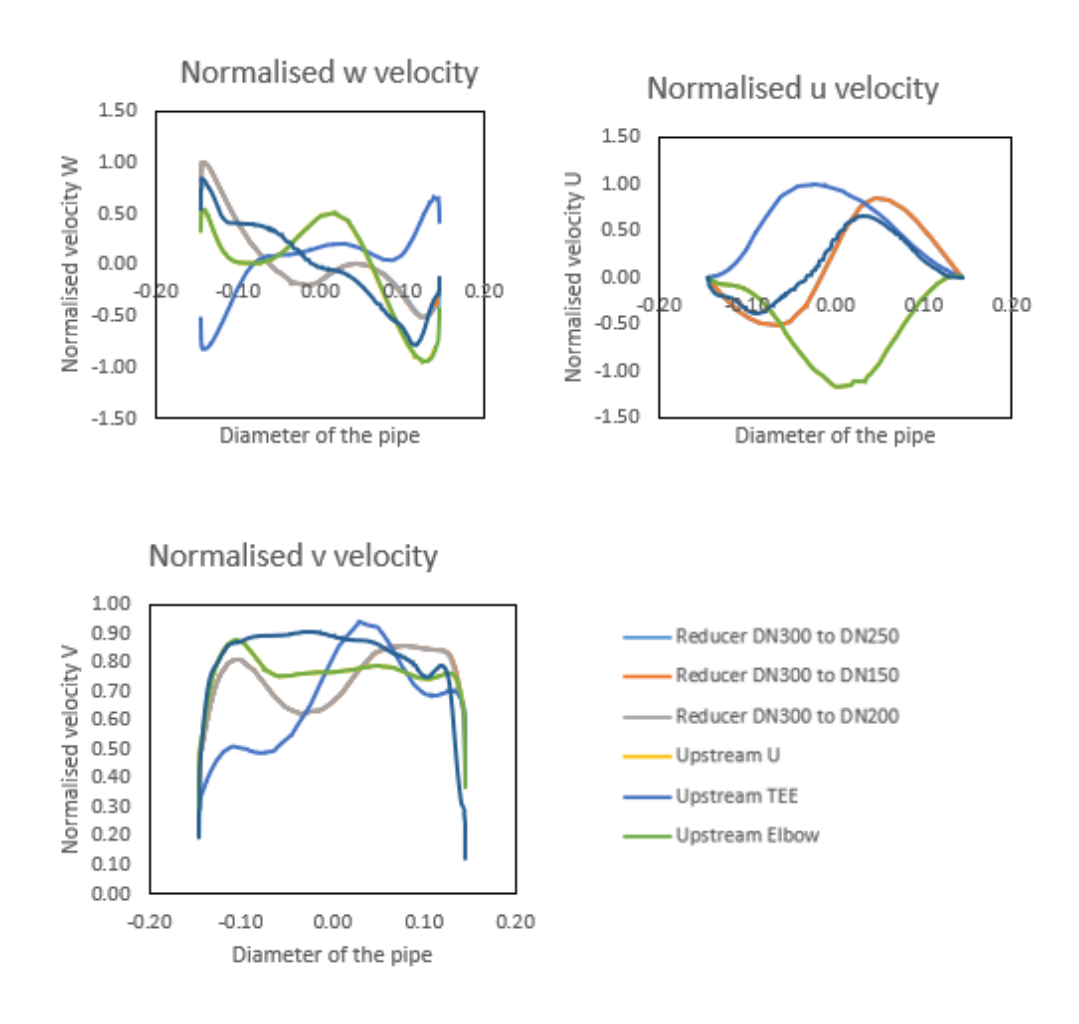


Figure 4-28: Normalised velocity components for all upstream geometrical configuration

# **UV** dose performance

The relationship between normalized dosage and LED power to flow rate ratio (LED/Q) is analysed across different UV transmittance (UVT) values of 98%, 88%, and 73%, demonstrating the system's performance under varying water quality conditions as shown in the Figure 4-29. At 98% UVT, where water has the highest transparency to UV light, the LED/Q ratio spans from 0 to 2.5, with all configurations demonstrating similar linear behavior as the normalised dosage increases from 0 to approximately 1.0. When UVT decreases to 88%, the system requires more power input, as shown by the extended LED/Q ratio up to 4.5, while maintaining the linear relationship across all configurations. This increased power requirement compensates for the reduced UV light transmission through the water. The most challenging condition occurs at 73% UVT, necessitating the highest LED power per unit flow rate, with the LED/Q ratio extending to approximately 5.5 while preserving the linear

relationship. This progressive increase in power requirements across decreasing UVT values demonstrates the system's adaptability to varying water quality conditions.

Notably, all configurations (UP Elbow, Full Assembly, Reducers, TEE, U) exhibit nearly identical performance across all UVT values, with strong linear correlations between dosage and LED/Q ratio, as indicated by the dotted trend lines for UP Elbow and Full Assembly configurations. The consistent performance across different inlet configurations suggests that the system's dosage delivery mechanism is robust and relatively independent of upstream conditions. This uniformity in performance indicates that the reactor design effectively normalizes flow patterns and ensures consistent treatment regardless of inlet conditions, making it particularly suitable for practical applications where installation configurations may vary. The linear relationship between dosage and LED/Q ratio across all conditions also provides a reliable basis for system control and optimization, allowing operators to adjust power levels predictably based on flow rates and water quality.

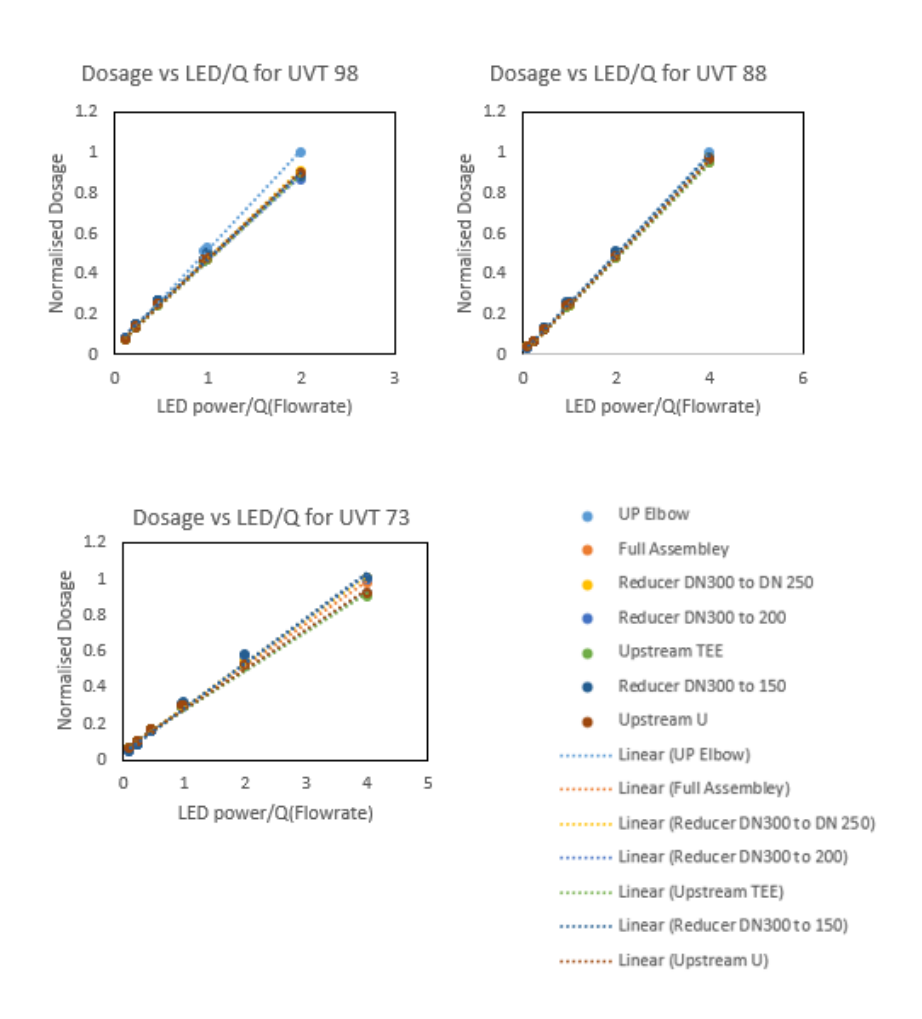


Figure 4-29: Relationship between LED power, UV dose and Flow rate for different upstream components for 3 different UVT

# 4.4 Conclusion

This chapter has presented comprehensive CFD analysis of flow characteristics and UV dose distribution in the commercial-scale UV LED reactor, revealing fundamental insights into performance drivers and establishing quantitative relationships for design optimization.

#### Flow Characterization:

The validated CFD model successfully captured complex three-dimensional swirling flow structures generated by stationary vanes and elbow geometry. Swirl number analysis demonstrated exponential scaling with Reynolds number (S = 0.0023·Re^0.6441), achieving S = 0.37 at nominal operating conditions within the optimal range for enhanced mixing without excessive pressure drop. Velocity field analysis revealed asymmetric distributions with offaxis vortex cores, characteristic S-shaped axial velocity profiles indicating vortex breakdown phenomena, and substantial tangential velocity components (40-50% of axial velocity) confirming effective swirl generation.

The swirl-enhanced flow provides 30% residence time extension compared to purely axial flow (mean residence time 1.63 s versus 1.25 s) through helical particle trajectories, while simultaneously promoting cross-sectional mixing that homogenizes UV exposure. Swirl decay analysis quantified 59% intensity reduction from inlet to outlet, with persistence of substantial rotational motion throughout the reactor ensuring sustained mixing effectiveness.

# **UV Dose Performance:**

UV dose distribution analysis established critical design relationships: exponential dependence on UVT (9.4× power increase from 98% to 73% UVT), inverse linear relationship with flow rate enabling predictable capacity scaling, and dramatic sensitivity to LED configuration (5.0-6.0× efficiency improvement from sparse to dense arrangements). The 30-ring configuration emerged as optimal cost-performance balance, achieving 55-60% of maximum efficiency with only 60% of LED count.

Dose uniformity analysis demonstrated coefficient of variation = 25%, substantially better than axial flow systems (CV > 50%), translating to 1.7-2.0 $\times$  higher RED for equivalent mean

dose. This efficiency enables either reduced LED power for specified treatment targets or increased capacity for given LED investment.

These quantitative relationships provide validated foundation for reactor design optimization and performance prediction across operating conditions.

# Chapter 5. Experimental Results and Discussion

PIV experiments were conducted on the scaled reactor model with equivalent CFD model developed to do a direct comparison of the hydrodynamics within the model. Experiments are conducted on three different types of configurations as detailed out in the methodology section. This section goes into the detail for the results of each of these sections.

# 5.1 Results for configuration 1

Velocity profiles were extracted along diametral lines at entry and exit locations (100 mm and 700 mm downstream of the elbow, respectively) in both vertical and horizontal measurement planes. These profiles quantify the axial and tangential velocity components that characterize the swirling flow structure and its development through the measurement section. Measurements were conducted at three flow rates (87, 132, and 175 m³/h, corresponding to Reynolds numbers of 110,774, 165,735, and 221,455) to assess flow rate effects on velocity distribution.

# 5.1.1 Vertical Plane Measurements

Figure 5-1 presents axial velocity (v-component) profiles measured in the vertical plane. The profiles exhibit the characteristic bell-shaped distribution typical of fully-developed turbulent pipe flow, with relatively uniform velocities across the core region and steeper gradients near the walls. The peak velocity magnitude scales proportionally with flow rate, reaching maximum values of approximately 0.8 m/s at 87 m³/h, 1.2 m/s at 132 m³/h, and 1.6 m/s at 175 m³/h, consistent with the nominal volumetric flow rates.

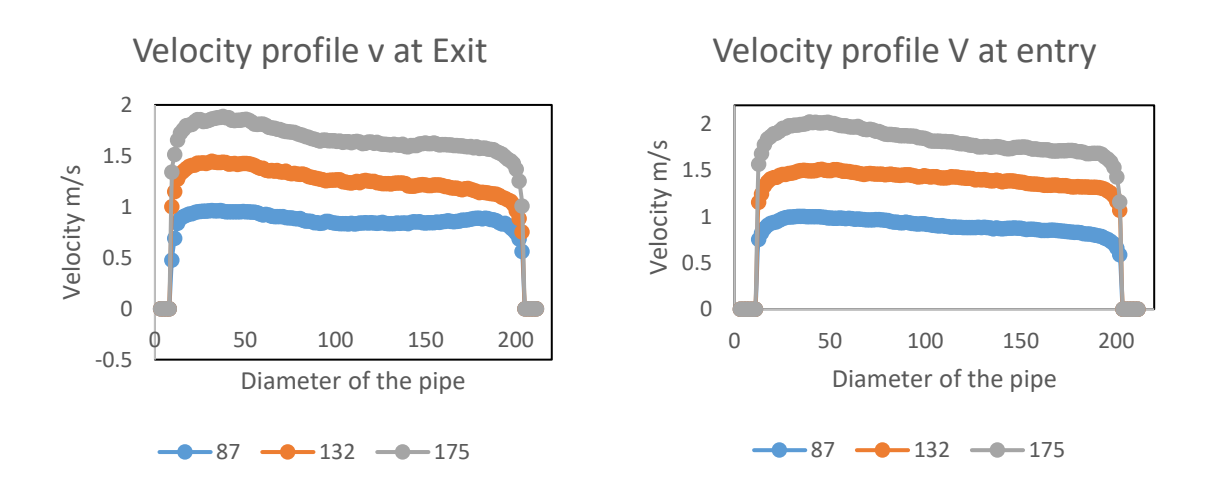


Figure 5-1: Axial velocity profile from the experimental results at entry and exit point for vertical plane

Comparing entry and exit locations, the axial velocity profiles show minimal variation, confirming that bulk flow rate is preserved through the measurement section as required by mass conservation. A slight reduction in peak velocity at the exit location is observed across all flow rates, potentially reflecting flow redistribution or minor measurement uncertainty rather than genuine velocity decay. The maintenance of the bell-shaped profile from entry to exit indicates that the fundamental turbulent flow structure persists despite the strong swirling motion characterized by tangential velocity components.

Figure 5-2 presents tangential velocity (w-component) profiles revealing the swirl structure and intensity. Unlike the relatively symmetric axial profiles, the tangential velocity exhibits complex spatial distributions with both positive and negative values across the pipe cross-section, characteristic of vortex flows with off-centre swirl cores. The profiles demonstrate clear evidence of strong secondary flows and organized swirl at all flow rates.

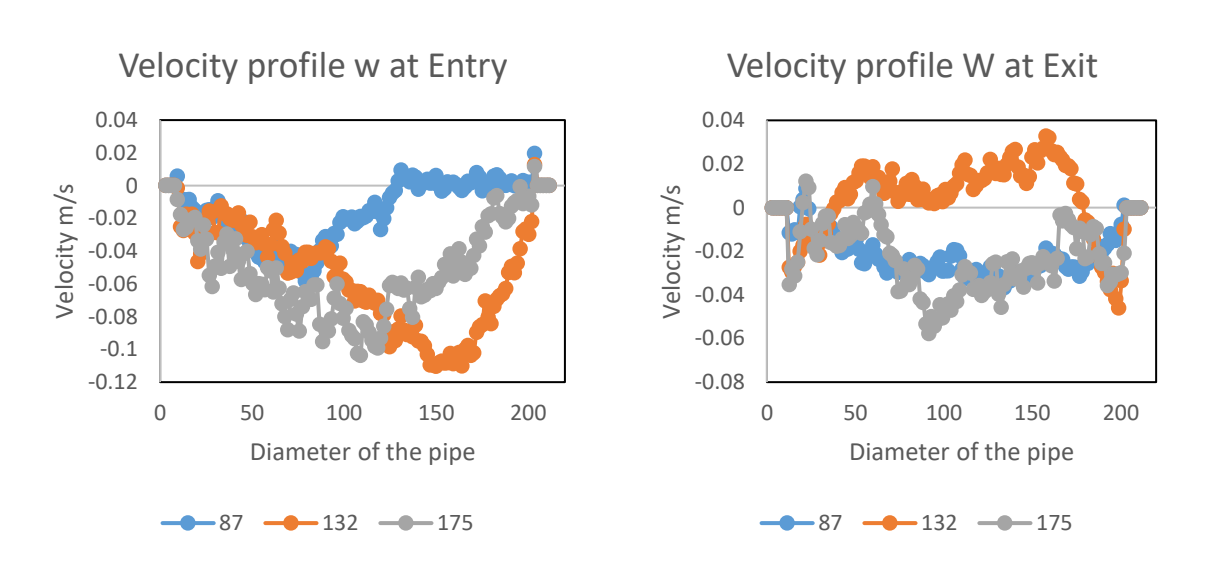


Figure 5-2: Tangential velocity profile from the experimental results at entry and exit point for vertical plane

The swirl intensity increases markedly with flow rate. This progressive increase confirms that swirl generation scales with Reynolds number, qualitatively consistent with the exponential relationship predicted by CFD analysis. The tangential velocity profiles also reveal pronounced asymmetry, with peak values occurring at different radial positions for positive versus negative velocities, indicating that the vortex core is displaced from the geometric centreline a characteristic feature of swirling flows generated by asymmetric inlet conditions.

Comparing entry versus exit locations, the tangential velocity profiles show substantial decay, with peak magnitudes reduced by approximately 40-50% over the 600 mm distance. This

decay confirms viscous dissipation of swirl energy through the measurement section, consistent with the swirl number reduction observed in CFD simulations. Despite this significant decay, substantial tangential velocities persist at the exit location (peak values 20-30% of axial velocity), indicating that swirl-enhanced mixing remains active throughout the reactor length rather than dissipating completely near the inlet.

#### **Horizontal Plane Measurements:**

Velocity profiles measured in the horizontal plane provide complementary three-dimensional characterization of the flow structure. The horizontal plane measurements were conducted by positioning the camera above the test section, resulting in a reversed coordinate system compared to the vertical plane measurements. Consequently, the axial velocity values appear negative, though the velocity magnitude and spatial distribution are consistent with the vertical plane measurements. This sign reversal is purely an artifact of the measurement coordinate system orientation and does not indicate reverse flow.

The axial velocity profiles in the horizontal plane (Figure 5-3) maintain the characteristic bell-shaped distribution observed in the vertical plane. This consistency confirms that the bulk flow structure does not exhibit variations, indicating relatively organized swirl with a dominant vortex structure rather than chaotic three-dimensional flow patterns.

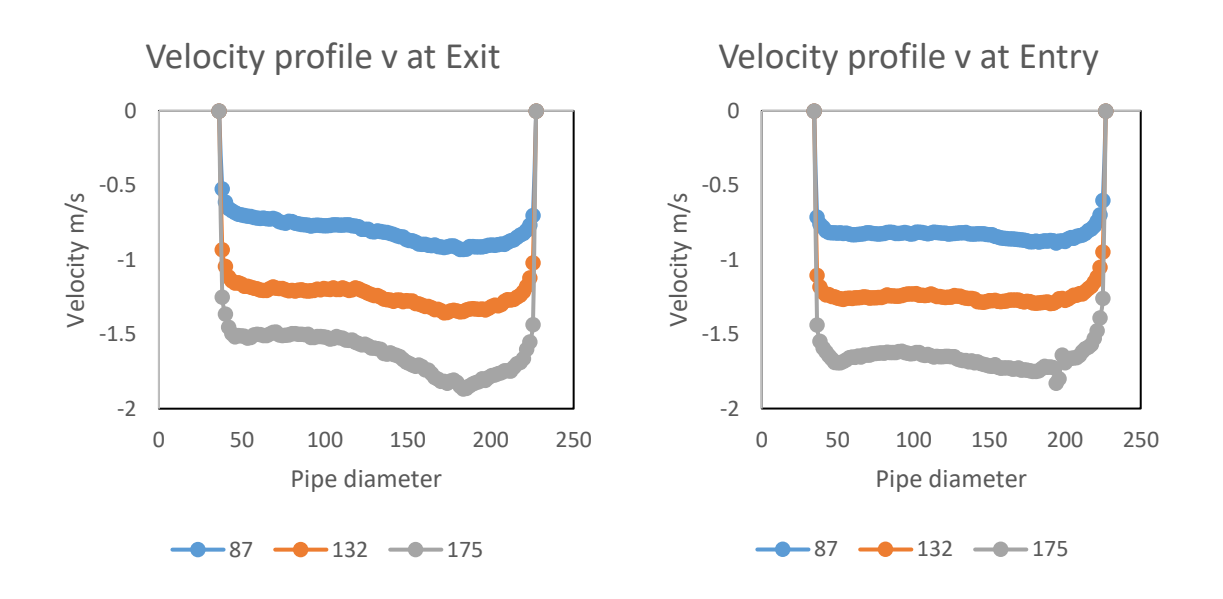


Figure 5-3: Axial velocity profile from the experimental results at entry and exit point for horizontal plane

The tangential velocity profiles in the horizontal plane (Figure 5-4) reveal more dramatic spatial variations compared to the vertical plane measurements. The horizontal profiles show approximately 20-30% higher peak tangential velocities and more pronounced oscillatory patterns across the pipe diameter, suggesting that the swirl structure exhibits azimuthal non-uniformity. These plane-to-plane differences indicate the three-dimensional flow complexity rather than perfectly axisymmetric swirl, with the vortex core potentially precessing or exhibiting helical distortions around the geometric centreline.

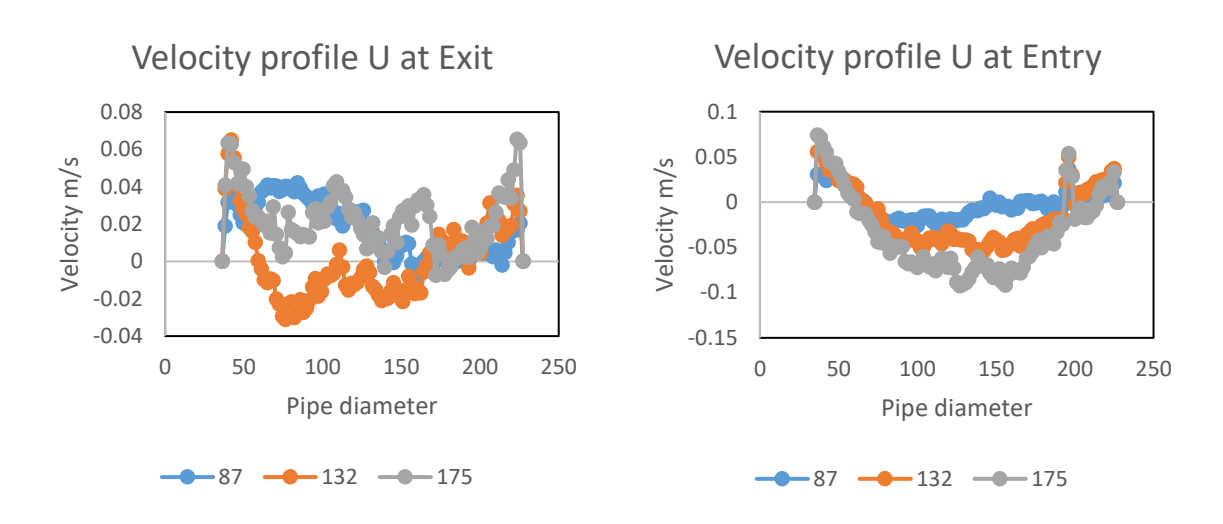


Figure 5-4: Tangential velocity profile from the experimental results at entry and exit point for horizontal plane

The tangential velocity variations between entry and exit locations are more substantial in the horizontal plane than in the vertical plane, with some regions showing enhanced tangential motion at the exit despite the overall trend of swirl decay. This complex development pattern suggests interactions between the primary swirl (generated by stationary vanes) and secondary flows (induced by the elbow), creating three-dimensional flow structures that evolve non-uniformly along the reactor length. These interactions likely enhance mixing effectiveness by generating multiple scales of secondary motion that promote cross-sectional fluid exchange.

# **5.1.2 Velocity Contours**

Velocity contours provide visual representation of flow patterns and fluid behavior at the measurement plane. Analysis was conducted on both vertical and horizontal planes for three flow rates (87, 132, and 175 m<sup>3</sup>/h), examining both axial and tangential velocity components.

## **Vertical Plane Analysis**

Figure 5-5, Figure 5-6 and Figure 5-7present velocity contours for the vertical measurement plane across all three flow rates. To enable direct comparison between flow conditions, a consistent velocity scale of 0 to 2 m/s was maintained across all visualizations.

The axial velocity contours reveal asymmetric flow patterns, particularly pronounced at higher flow rates. The red zones indicating maximum velocity appear displaced from the pipe centerline, confirming the off-axis nature of the swirling flow. This asymmetry intensifies with increasing flow rate, with the 175 m<sup>3</sup>/h condition showing the most pronounced displacement.

Tangential velocity contours demonstrate the complex mixing characteristics within the reactor. The presence of both positive (red/yellow) and negative (blue) velocity regions indicates counter-rotating flow structures typical of swirling flows. These secondary flow patterns are essential for enhanced mixing and improved UV dose distribution. The color gradients become more dramatic at higher flow rates, reflecting stronger velocity gradients and more intense mixing. At 87 m³/h, the tangential velocity patterns are relatively mild, while at 175 m³/h, distinct regions of opposing flow direction are clearly visible, indicating vigorous mixing throughout the cross-section.

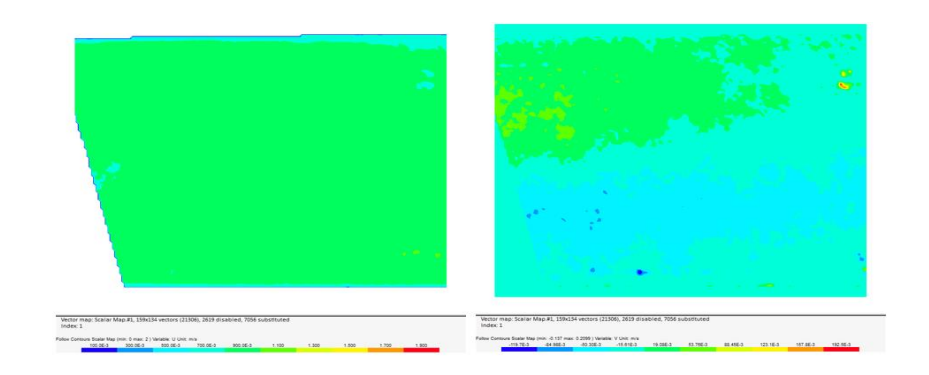


Figure 5-5: Velocity contours for axial and tangential velocity components for 87 m3/h flow rate for vertical plane

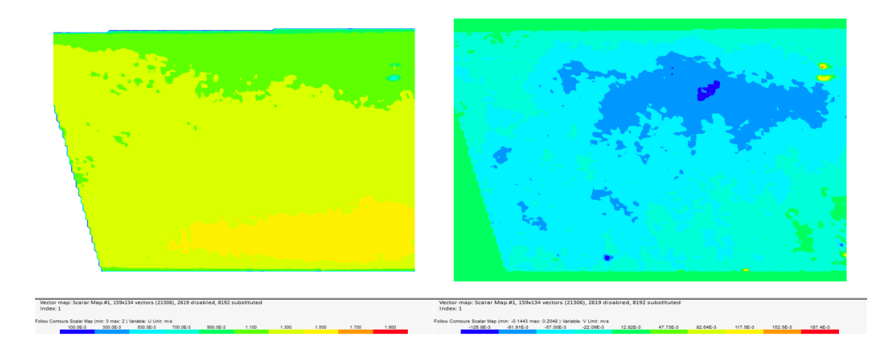


Figure 5-6: Velocity contours for axial and tangential velocity components for 132 m3/h flow rate for vertical plane

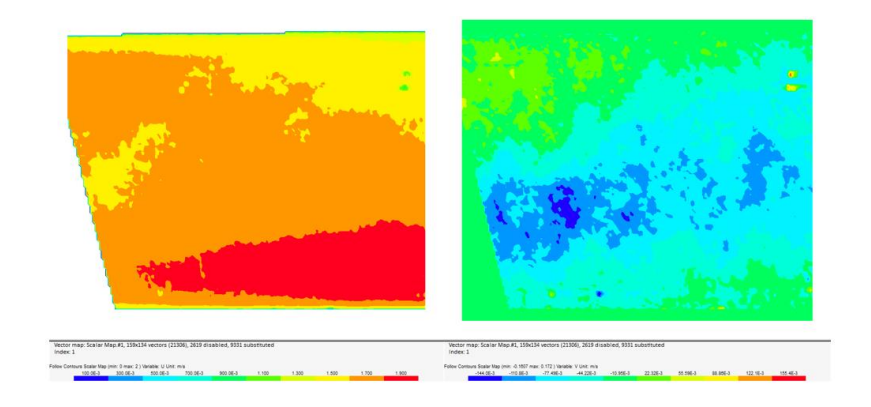


Figure 5-7: Velocity contours for axial and tangential velocity components for 175 m3/h flow rate for vertical plane

# **Horizontal Plane Analysis**

Figure 5-8, Figure 5-9 and Figure 5-10 show velocity contours for the horizontal measurement plane. The axial velocity measurements appear negative due to the measurement orientation (camera positioned above the test section), though the magnitudes remain consistent with the vertical plane measurements. Similar to the vertical plane, flow asymmetry is evident, with the blue regions (representing the primary flow direction in this orientation) concentrated on one side of the pipe rather than centred. This confirms that the swirl-induced flow displacement occurs in three dimensions, not just within a single measurement plane.

The tangential velocity contours on the horizontal plane exhibit similar mixing characteristics to the vertical plane, with clear evidence of secondary flow structures. The intensity of both velocity components increases proportionally with flow rate, maintaining the overall flow pattern characteristics across all tested conditions. The consistency between horizontal and vertical plane measurements validates the three-dimensional nature of the swirling flow and confirms that the flow structures are maintained throughout the reactor length.

The progression from 87 to 175 m<sup>3</sup>/h demonstrates how increasing flow rate enhances both the swirl intensity and mixing characteristics, supporting the quantitative findings from the velocity profile and swirl number analyses presented earlier.

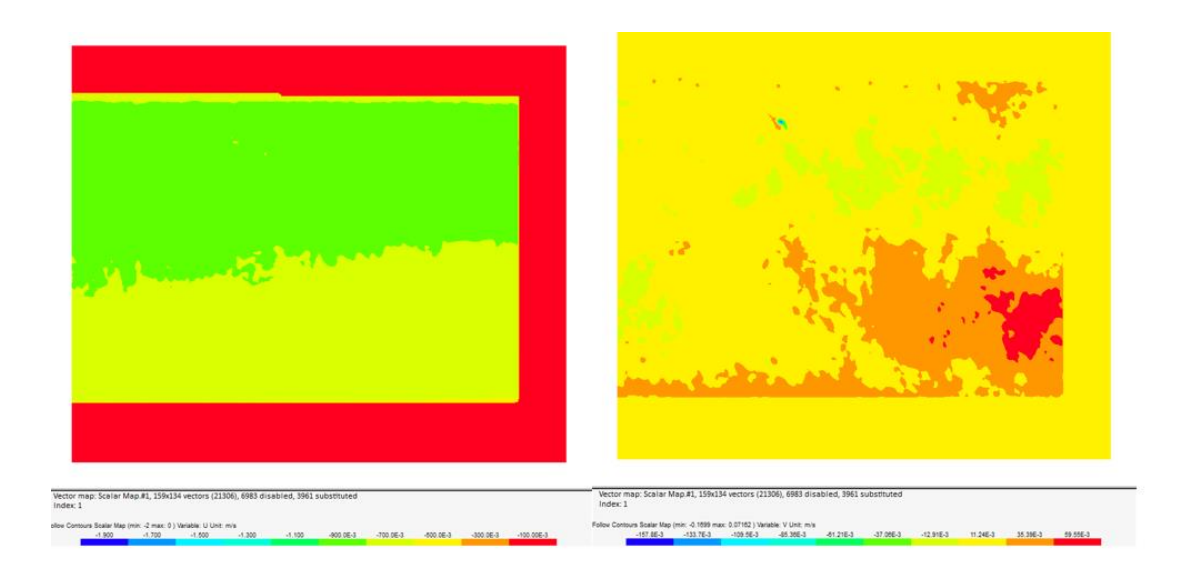


Figure 5-8: Velocity contours for axial and tangential velocity components for 87 m3/h flow rate for horizontal plane

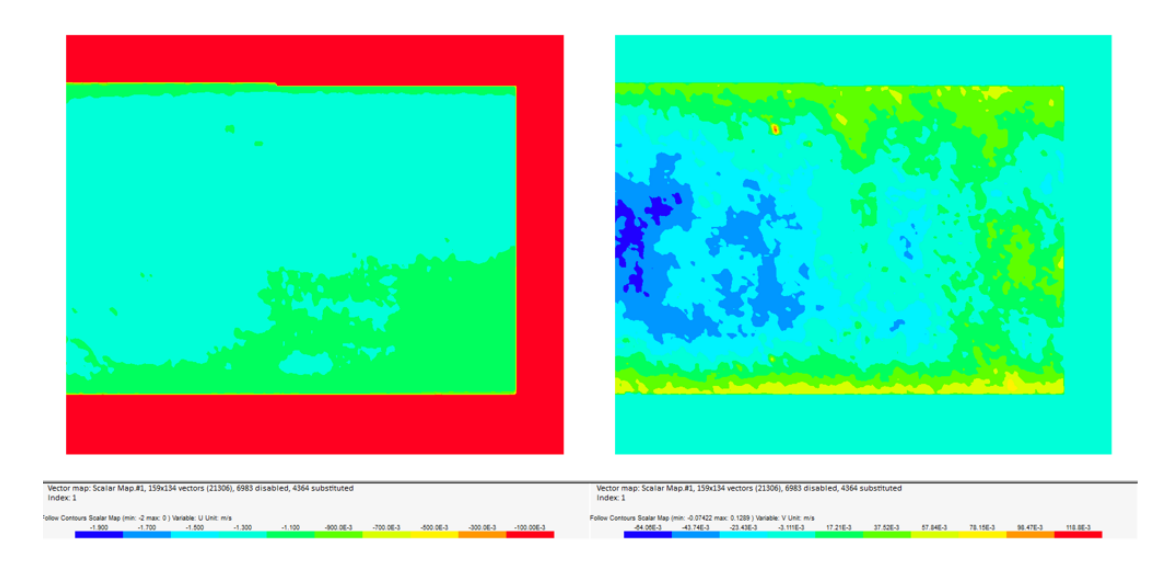


Figure 5-9: Velocity contours for axial and tangential velocity components for 132 m3/h flow rate for horizontal plane

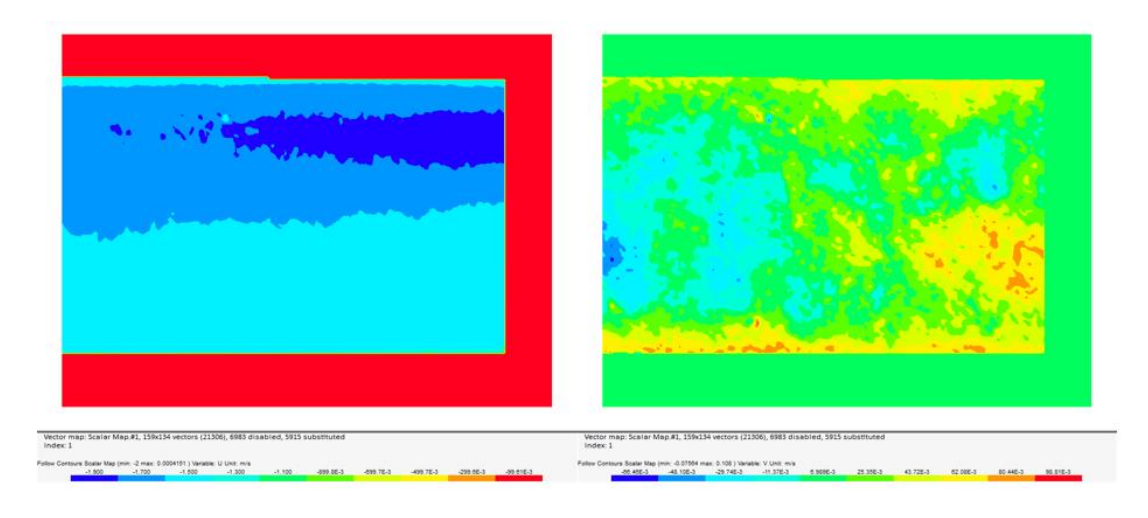


Figure 5-10: Velocity contours for axial and tangential velocity components for 175 m3/h flow rate for horizontal plane

# 5.2 Configuration 2 results

A comparative analysis was conducted between upstream and downstream vane configurations to assess the impact of vane positioning on flow characteristics. Measurements were taken at the entry point of the measurement section at a flow rate of 175 m<sup>3</sup>/h, representing the highest tested operating condition.

# **Axial Velocity Comparison**

Figure 56 presents the axial velocity profiles for both configurations. The profiles exhibit remarkably similar overall shapes, with both configurations displaying asymmetric velocity distributions. In both cases, the maximum velocity magnitude occurs at a location displaced from the pipe centerline, confirming the presence of swirling flow regardless of vane position.

A subtle but notable difference exists in the velocity distribution uniformity. The upstream vane configuration produces a slightly more uniform velocity profile across the pipe cross-section, suggesting more developed flow conditions by the time the fluid reaches the measurement location. In contrast, the downstream vane configuration shows marginally greater variation in the velocity distribution, potentially indicating that the flow has had less distance to develop after passing through the vanes.

# **Tangential Velocity Comparison**

The tangential velocity component reveals the most significant differences between the two configurations, as shown in Figure 5-11. The downstream vane configuration generates substantially higher tangential velocity magnitudes, indicating a stronger rotational flow component compared to the upstream configuration. This enhanced rotational motion suggests that positioning vanes closer to the measurement section (downstream of the elbow) may intensify swirl characteristics.

An interesting observation is the reversal in flow direction between configurations, evidenced by the opposite signs of the tangential velocity values. Where the upstream configuration shows positive tangential velocities, the downstream configuration exhibits negative values, and vice versa.

These findings suggest that vane positioning relative to the elbow and measurement section plays a critical role in determining both the intensity and direction of the swirling flow, with downstream positioning generating more pronounced rotational characteristics.

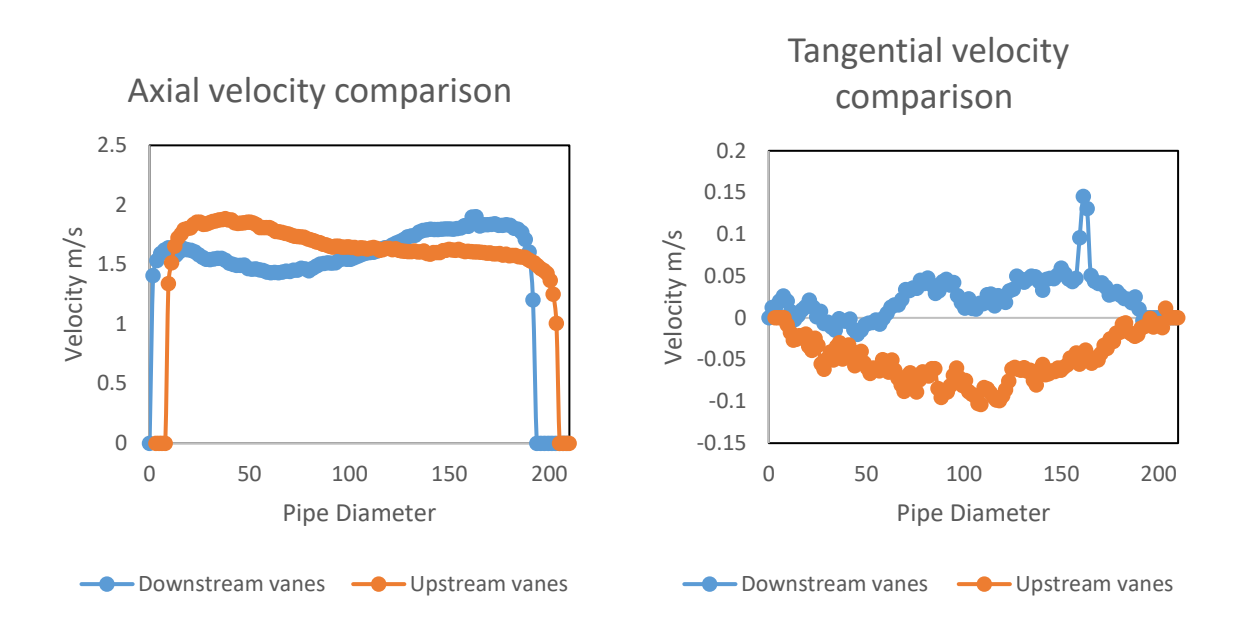


Figure 5-11: Comparison of the axial and tangential velocity profile for the Upstream vanes with Downstream vanes configuration

# 5.3 Configuration 3 results

Configuration 3 examines the flow characteristics in the absence of static vanes, providing direct comparison with the upstream vane configuration (Configuration 1). This analysis isolates the specific contribution of the vanes to the overall flow behavior. Measurements were conducted at the measurement section entry point at 175 m<sup>3</sup>/h flow rate.

# **Axial Velocity Analysis**

Figure 5-12 demonstrates that the axial velocity profiles remain remarkably consistent between the vaned and vaneless configurations. Both exhibit similar velocity distributions with maximum velocity magnitudes occurring away from the pipe centerline. This asymmetric pattern persists even without vanes, suggesting that the elbow upstream of the measurement section contributes to flow displacement from the central axis.

The similarity in axial velocity profiles indicates that the primary throughflow characteristics remain largely unaffected by vane presence. This is a significant finding, as it demonstrates

that the introduction of static vanes does not create substantial flow blockage or disruption to the main flow path through the reactor.

# **Tangential Velocity Analysis**

The tangential velocity component reveals the critical distinction between configurations. While both the vaned and vaneless setups follow similar velocity profile patterns, the upstream vane configuration exhibits substantially higher tangential velocity magnitudes. This marked difference directly demonstrates the effectiveness of the static vanes in generating and intensifying the rotational flow component.

The enhanced tangential velocities in the vaned configuration confirm that the static vanes serve their intended purpose of inducing stronger swirling motion within the reactor. This intensified swirl promotes improved cross-sectional mixing and more uniform residence time distribution, both essential for effective UV treatment. The increased rotational component translates to enhanced particle trajectories through varying UV intensity zones within the reactor, leading to more consistent dosage delivery.

The combination of maintained axial flow with enhanced tangential motion demonstrates that the vanes effectively introduce rotational energy into the system without compromising overall flow capacity or creating significant pressure losses. This balance between preserving throughflow and generating beneficial secondary flows represents optimal design for UV reactor applications, where both adequate residence time and thorough mixing are required for effective disinfection.

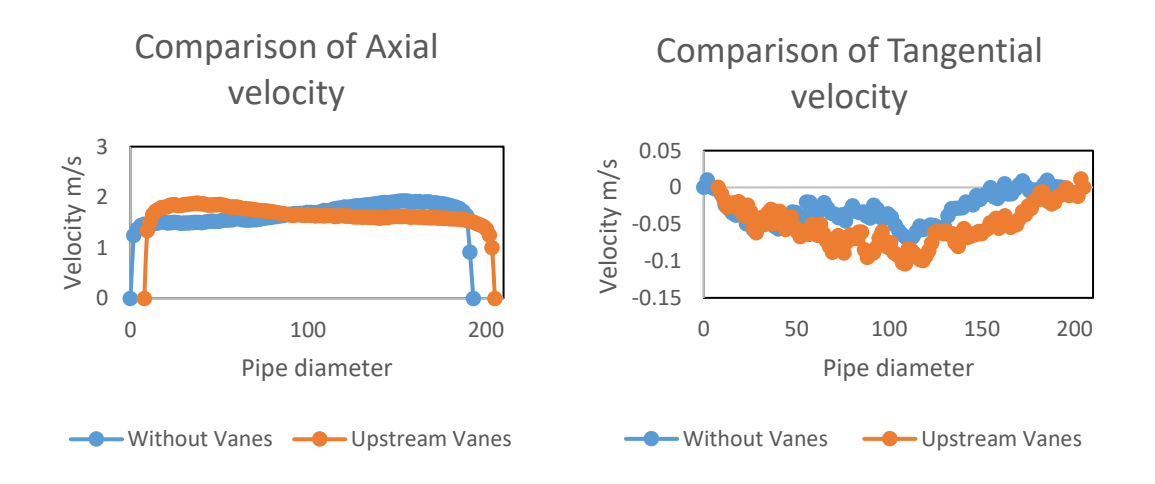


Figure 5-12: Comparison of the axial and tangential velocity profile with Upstream vanes with Downstream vanes configuration

# 5.4 Conclusion

This chapter has presented comprehensive Particle Image Velocimetry measurements characterizing swirling flow structures in the scaled UV LED reactor across three geometric configurations and multiple operating conditions, providing essential experimental validation data for CFD model assessment.

# **Configuration 1 - Primary Design Analysis:**

Detailed velocity field measurements at three flow rates (87, 132, 175 m³/h corresponding to Re = 110,774-221,455) revealed well-developed swirling flow with substantial tangential velocities reaching 40-50% of axial velocity magnitudes. Axial velocity profiles exhibited characteristic bell-shaped distributions with minimal entry-to-exit variation (<10%), confirming mass conservation and flow stability. Tangential velocity profiles demonstrated strong swirl with pronounced asymmetry indicating off-axis vortex cores, characteristic of engineered swirl generation systems.

Swirl decay analysis showed 40-50% tangential velocity reduction over the 600 mm measurement section, confirming viscous dissipation while maintaining substantial rotational motion at exit (20-30% of axial velocity). Three-dimensional flow complexity was evident through differences between vertical and horizontal measurement planes (20-30% higher tangential velocities in horizontal plane), revealing non-uniformity and helical vortex structures that enhance mixing effectiveness through multiple secondary flow scales.

# **Comparative Configuration Analysis:**

Configuration 2 (downstream vanes) generated approximately 20% higher tangential velocities than Configuration 1 (upstream vanes), suggesting potential performance benefits from alternative vane positioning requiring further investigation across flow rate ranges. Configuration 3 (no vanes) demonstrated dramatically reduced tangential velocities while maintaining similar axial profiles, confirming that vanes contribute the dominant swirl generation mechanism with elbows providing minimal enhancement.

# Chapter 6. Model Validation

The CFD model's predictive capability was validated through two independent approaches: (1) comparison of predicted UV dose against full-scale biodosimetry experimental measurements, and (2) comparison of predicted velocity fields against PIV experimental measurements in a scaled reactor model. This dual validation strategy assesses both the ultimate performance metric (disinfection efficacy via dosage) and the underlying hydrodynamic predictions that govern dosage distribution. Together, these validations provide comprehensive confidence in the model's accuracy for reactor design, optimization, and performance prediction.

# 6.1 UV dose Validation with Biodosimetry Experiments

Biodosimetry validation testing was conducted by Typhon Treatment Systems Ltd on a full-scale UV LED reactor with geometry matching the CFD model (BIO310, DN310 reactor diameter, 1000 LEDs in 50 rings). The validation employed MS2 bacteriophage as the challenge microorganism across a test matrix encompassing three flow rates (80, 125, and 250 m³/h) and three UVT conditions (90%, 95%, and 98%), yielding nine primary operating conditions for model-experiment comparison.

# **6.1.1 Comparison Across UVT Conditions**

# 80 m<sup>3</sup>/h Flow Rate:

Figure 6-1 presents the comparison at the lowest flow rate tested (80 m³/h), where the longest residence time yields the highest RED values. The model-experiment agreement is excellent across all UVT conditions.

At 90% UVT, the model predicts RED =  $30.16 \text{ mJ/cm}^2$  compared to experimental RED =  $28.06 \text{ mJ/cm}^2$  (7.5% overprediction). At 95% UVT, predicted RED =  $43.34 \text{ mJ/cm}^2$  versus experimental RED =  $36.42 \text{ mJ/cm}^2$  (19% overprediction). At 98% UVT, predicted RED =  $56.87 \text{ mJ/cm}^2$  versus experimental RED =  $51.95 \text{ mJ/cm}^2$  (9.5% overprediction).

The agreement at 80 m<sup>3</sup>/h shows greater variability compared to higher flow rates, with discrepancies ranging from 7.5% to 19%. The largest deviation occurs at 95% UVT, which may reflect increased sensitivity to experimental uncertainties at conditions where UV penetration and mixing dynamics create complex dose distributions. At lower flow rates where residence

times are longer (approximately 2.5 seconds), small variations in flow patterns or LED output characteristics can have proportionally larger effects on integrated UV dose. Despite these variations, all predictions remain within or near the experimental uncertainty bounds (±29.4%), confirming adequate model accuracy across the operational range.

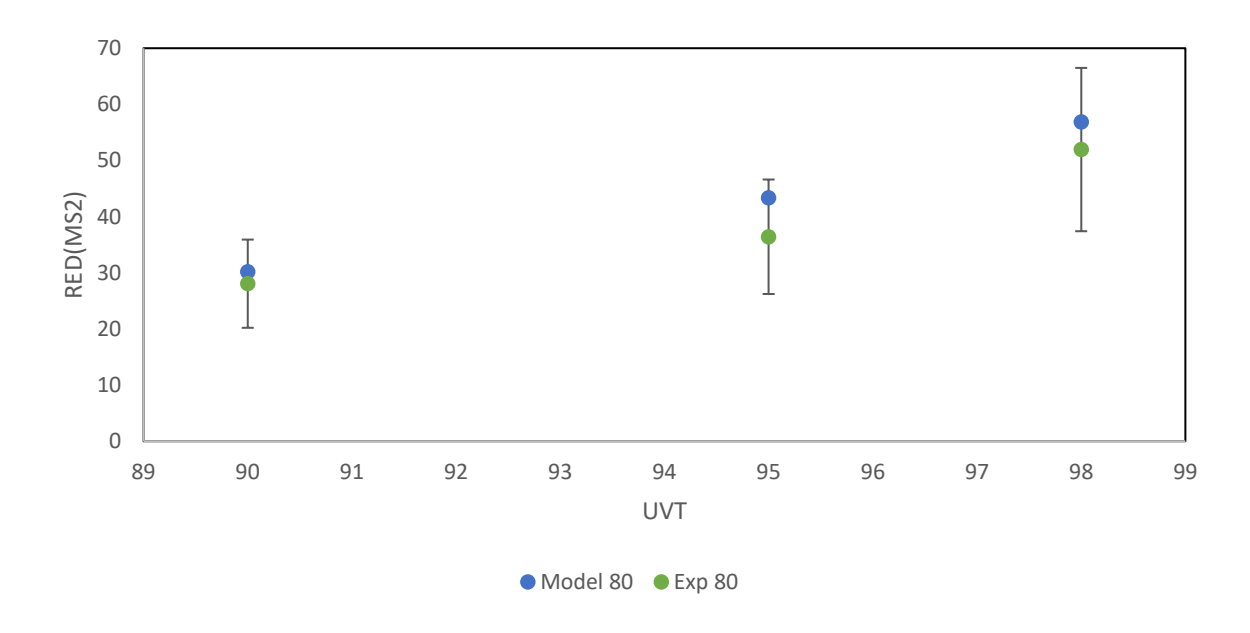


Figure 6-1: Comparison of the RED dosage vs UVT for 125 m3/h flow rate for experimental result vs numerical result

# 125 m<sup>3</sup>/h Flow Rate:

Figure 6-2 presents the comparison between model-predicted RED and experimentally-measured RED values at 125 m³/h across the UVT range. Both model and experimental results demonstrate the expected exponential increase in RED with improving UVT, rising from approximately 20 mJ/cm² at 90% UVT to 40 mJ/cm² at 98% UVT. This exponential relationship reflects Beer-Lambert absorption physics, with higher UVT enabling deeper UV penetration and proportionally higher dose delivery.

At 90% UVT, the model predicts RED =  $19.68 \text{ mJ/cm}^2$  compared to experimental RED =  $22.09 \text{ mJ/cm}^2$  (11% underprediction). At 95% UVT, predicted RED =  $29.88 \text{ mJ/cm}^2$  versus experimental RED =  $28.17 \text{ mJ/cm}^2$  (6% overprediction). At 98% UVT, predicted RED =  $40.54 \text{ mJ/cm}^2$  versus experimental RED =  $39.99 \text{ mJ/cm}^2$  (1.4% overprediction).

The agreement at 125 m<sup>3</sup>/h is excellent, with predictions varying from 1.4% to 11% relative to experimental measurements. The model demonstrates no consistent bias at this flow rate, with both slight overpredictions and underpredictions observed across the UVT range. This

variation pattern, while larger than ideal, remains well within experimental uncertainty (±29.4%) and suggests that the model captures the fundamental physics governing dose delivery, with discrepancies likely reflecting the combined uncertainties of both experimental measurements and numerical predictions rather than systematic modeling deficiencies.

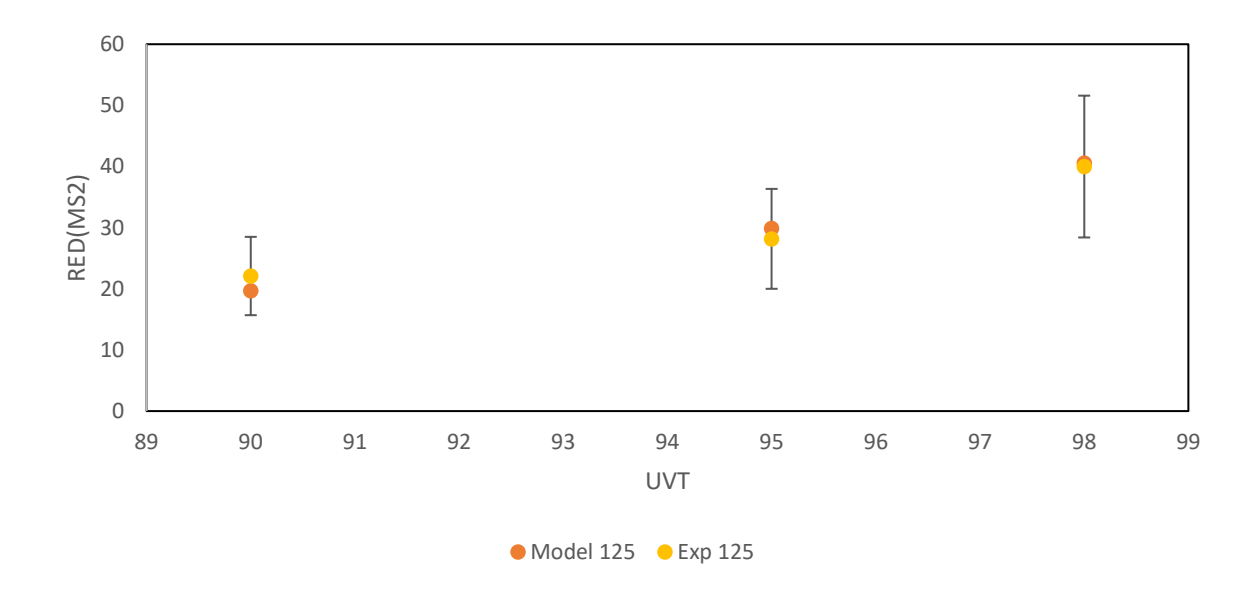


Figure 6-2: Comparison of the RED dosage vs UVT for 250 m3/h flow rate for experimental result vs numerical result

# 250 m<sup>3</sup>/h Flow Rate:

Figure 6-3 presents model-experiment comparison at the highest flow rate of 250 m<sup>3</sup>/h. At this condition, both model and experiments show reduced RED values compared to 125 m<sup>3</sup>/h due to shorter residence time (approximately 50% reduction, consistent with the 2× flow rate increase). The model demonstrates good agreement with experiments across the UVT range.

At 90% UVT, predicted RED =  $12.24 \text{ mJ/cm}^2$  versus experimental RED =  $15.2 \text{ mJ/cm}^2$  (19.5% underprediction). At 95% UVT, predicted RED =  $15.96 \text{ mJ/cm}^2$  versus experimental RED =  $18.9 \text{ mJ/cm}^2$  (15.6% underprediction). At 98% UVT, predicted RED =  $21.99 \text{ mJ/cm}^2$  versus experimental RED =  $26.64 \text{ mJ/cm}^2$  (17.5% underprediction).

The 250 m³/h condition exhibits consistent underprediction across all UVT levels, with discrepancies ranging from 15.6% to 19.5%. This systematic conservative bias at the highest flow rate may reflect limitations in the turbulence model's ability to accurately predict mixing intensity at elevated Reynolds numbers (Re = 442,909). The SST k- $\omega$  model, while generally robust for swirling flows, may underestimate turbulent diffusion at very high Reynolds numbers, leading to prediction of slightly lower dose uniformity and consequently lower RED

values. Alternatively, experimental uncertainties may be amplified at high flow rates due to challenges in maintaining stable MS2 concentrations and achieving representative sampling during shorter residence times. Despite the larger discrepancies at this condition, all predictions remain within or approach the experimental uncertainty bounds (±29.4%), and the conservative nature of the predictions is advantageous for design applications, ensuring that systems will meet or exceed specified performance targets.

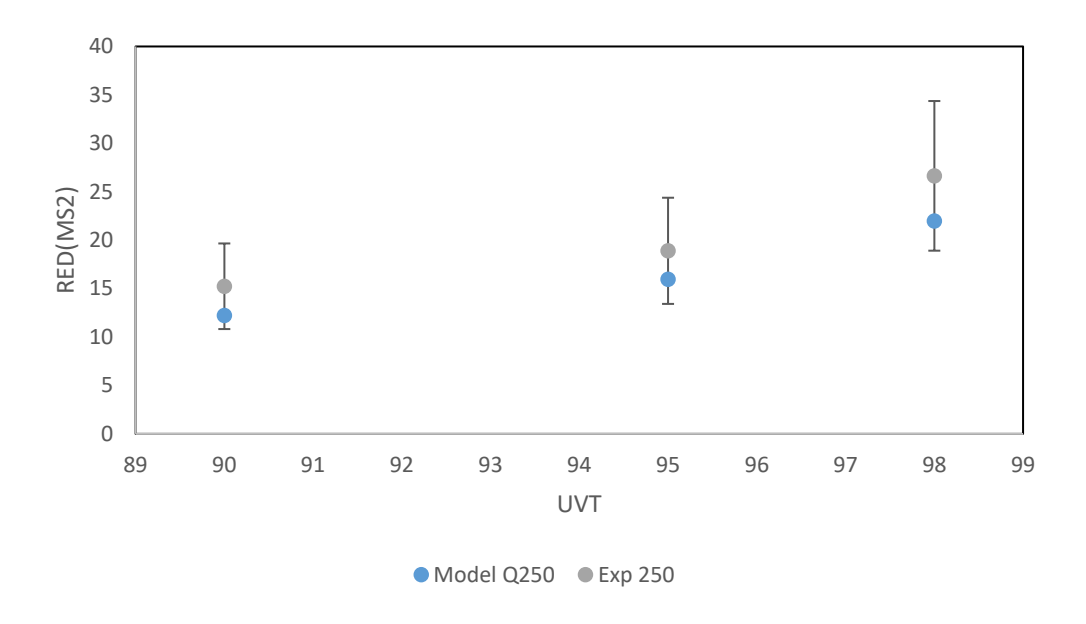


Figure 6-3: Comparison of the RED dosage vs UVT for 80 m3/h flow rate for experimental result vs numerical result

# 6.1.2 Systematic Trends and Model Accuracy

Figure 6-4 presents the percentage difference between experimental and numerical RED predictions across all nine test conditions (three flow rates  $\times$  three UVT levels), revealing important patterns in model accuracy and bias characteristics. The error distribution ranges from -16% to +24%, demonstrating variability that depends on both flow rate and water quality conditions.

## Flow Rate Dependence:

A clear trend of systematic bias variation with flow rate is observable. At 250 m³/h (highest flow rate), the model consistently underpredicts RED across all UVT levels with errors of 18-24% (average 21%). At 125 m³/h (nominal flow rate), errors range from -6% to +12% with minimal average bias (-1% to +12% depending on UVT), showing the best overall agreement. At 80 m³/h (lowest flow rate), the model overpredicts RED with errors of -7% to -16% (average -11%).

This flow rate-dependent bias pattern suggests that the turbulence model's representation of mixing intensity varies systematically with Reynolds number. At high flow rates (Re  $\approx$  443,000), the model appears to underpredict mixing effectiveness, leading to conservative (lower) RED predictions. At low flow rates (Re  $\approx$  138,000), the model overpredicts mixing or residence time, yielding non-conservative (higher) RED predictions. The optimal accuracy at intermediate Reynolds numbers (Re  $\approx$  221,000) indicates that the SST k- $\omega$  turbulence model calibration is most appropriate for this flow regime.

## **UVT Dependence:**

Within each flow rate, error magnitude shows modest variation with UVT but no consistent directional trend. At  $250 \, \text{m}^3/\text{h}$ , errors increase slightly from 18% (95% UVT) to 24% (90% UVT), suggesting marginally reduced accuracy at lower water quality. At  $125 \, \text{m}^3/\text{h}$  and  $80 \, \text{m}^3/\text{h}$ , no clear UVT trend is discernible, with errors varying by  $\pm 5$ -10% across the UVT range without systematic progression.

The absence of strong UVT-dependent error trends indicates that the optical absorption model (Beer-Lambert law with wavelength-specific absorption coefficients) accurately captures UV penetration physics across the 90-98% UVT range. The primary modeling uncertainty arises from hydrodynamic predictions (residence time distribution, swirlenhanced mixing intensity) rather than optical calculations, confirming that turbulence modeling represents the dominant source of prediction variability.

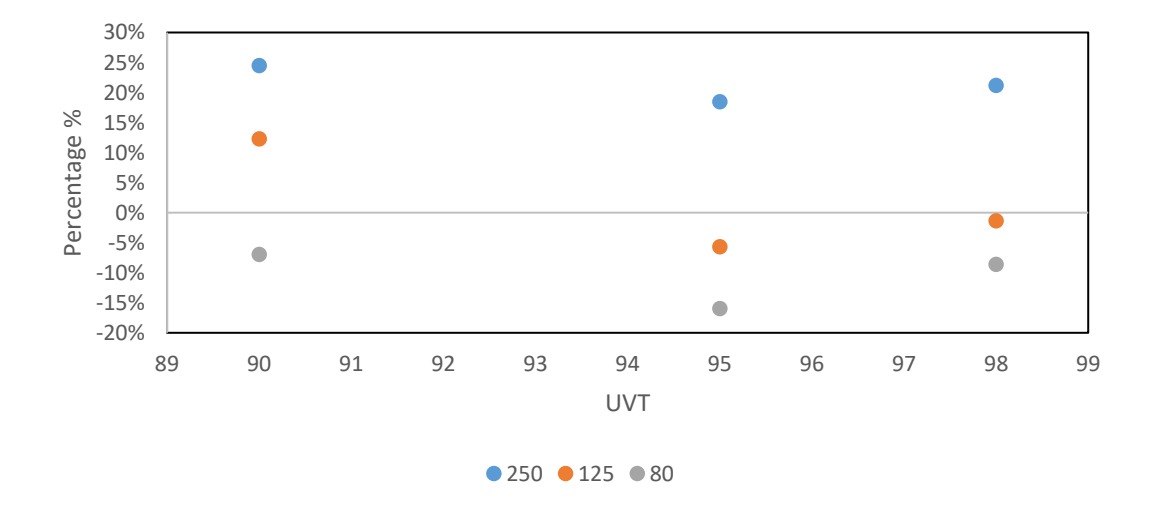


Figure 6-4: Difference between the experimental result and model result in percentage for all flow rates

## 6.1.3 Overall Validation Assessment

Figure 6-5 presents a scatter plot of experimental RED versus model-predicted RED for all nine test conditions, with the diagonal line representing perfect agreement between predictions and measurements. The data points cluster tightly around a linear trend with minimal scatter, confirming strong correlation between computational and experimental results. A linear regression through the data yields the relationship y = 0.7716x + 6.5133 with  $R^2 = 0.9662$ , demonstrating excellent correlation.

The regression slope of 0.77 indicates that the model exhibits systematic behavior across the operational range, with the relationship deviating from the ideal 1:1 correspondence. The positive intercept (6.5 mJ/cm²) combined with the sub-unity slope reveals that the model tends to overpredict RED at lower experimental values and underpredict at higher experimental values. This non-uniform bias pattern suggests that prediction accuracy varies with operating conditions—specifically, the model shows better agreement at intermediate flow rates (125 m³/h) and systematic deviations at operational extremes (80 and 250 m³/h).

Despite this bias pattern, the high R<sup>2</sup> value (0.9662) confirms that the model accurately captures the relative effects of flow rate and UVT on performance, explaining 96.6% of the variance in experimental measurements. This strong correlation validates the model's utility for predicting performance trends and conducting comparative analyses across operating conditions, even where absolute predicted values show systematic deviations from measurements. The excellent correlation is particularly valuable for design optimization and parametric studies, where relative performance differences between configurations are more critical than absolute accuracy of individual predictions.

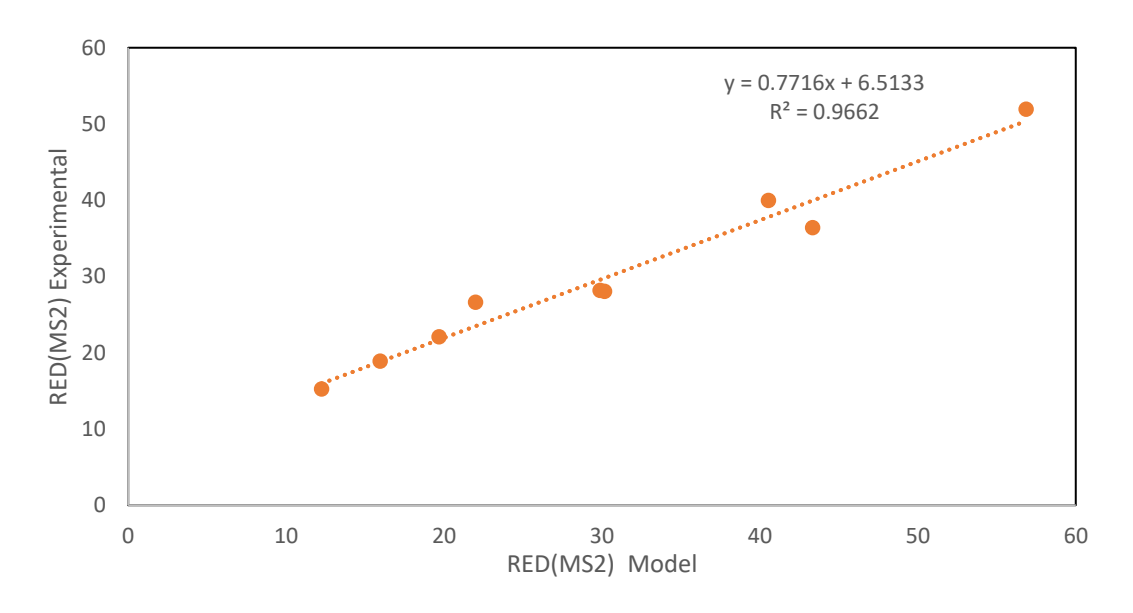


Figure 6-5: RED comparison of the experimental result vs numerical model result

# 6.2 Flow Field Validation with PIV Experiments

PIV experimental measurements on the scaled reactor model (DN200) provide direct validation of the CFD model's hydrodynamic predictions independent of UV dose calculations. A CFD model matching the scaled experimental geometry was developed following identical physics, meshing, and solver settings as the full-scale model (Section 6.2.2). Comparisons were conducted at three flow rates (87, 132, and 175 m³/h) at entry and exit locations in the vertical measurement plane.

# 6.2.1 Swirl Number Comparison

Figure 6-6 presents the calculated swirl number as a function of Reynolds number for both experimental PIV measurements and numerical CFD predictions. Both datasets demonstrate a strong exponential relationship between swirl intensity and Reynolds number, with CFD predictions achieving  $R^2 = 0.9952$  and experimental measurements achieving  $R^2 = 0.9698$ . These excellent correlations confirm that swirl generation scales systematically and predictably with flow rate across the operational range tested.

The comparison reveals that CFD predictions consistently exceed experimental swirl number values at comparable Reynolds numbers. At Re  $\approx$  110,000 (87 m³/h), the numerical model predicts S = 0.22 compared to experimental S = 0.17, representing 29% overprediction. At Re  $\approx$  221,000 (175 m³/h), the numerical prediction of S = 0.38 exceeds the experimental value of S = 0.33 by 15%. This systematic overprediction suggests that the CFD model may

overestimate the effectiveness of swirl generation by the vane-elbow system or underestimate the rate of turbulent dissipation of rotational momentum.

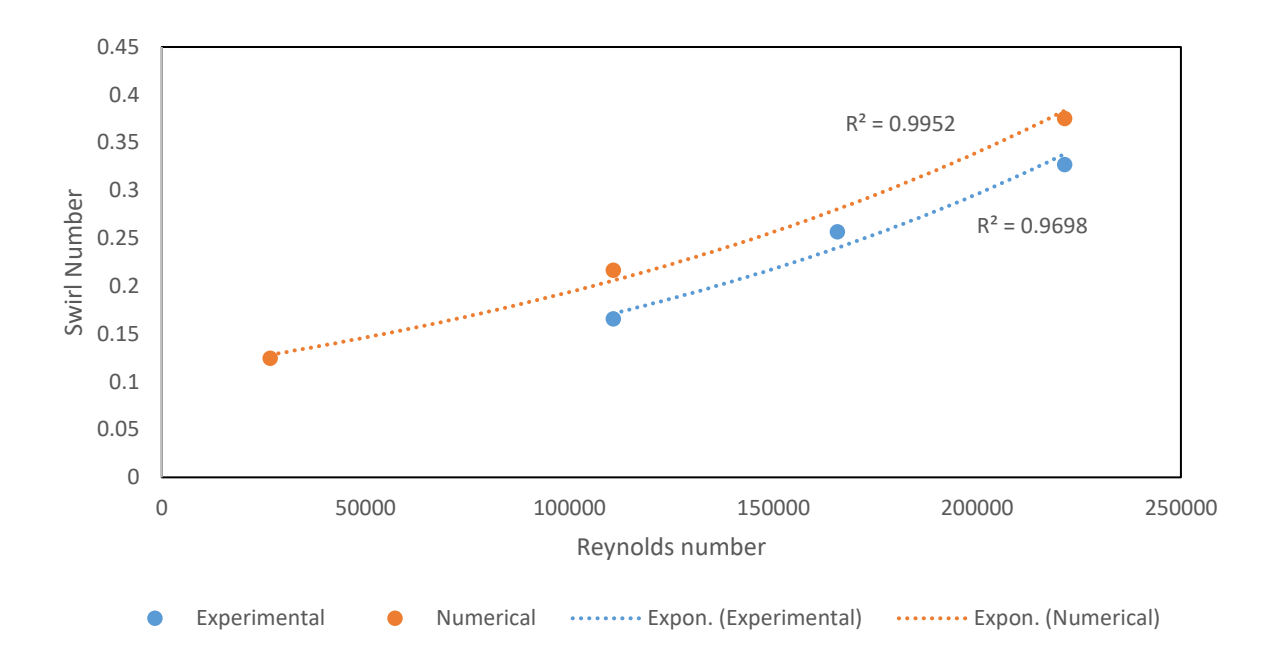


Figure 6-6: Comparison of swirl number between experimental and numerical results

# 6.2.2 Axial Velocity Profile Comparison

Figure 6-7 presents direct comparison of axial velocity profiles from CFD and PIV measurements at entry and exit locations for all three flow rates (87, 132, and 175 m $^3$ /h). The normalized profiles demonstrate excellent agreement between computational predictions and experimental measurements across the core flow region (|r/R| < 0.7), with maximum deviations less than 5%.

Both CFD and PIV profiles exhibit the characteristic bell-shaped distribution typical of fully developed turbulent pipe flow, with relatively flat velocity across the core region and steeper gradients approaching the walls. The velocity magnitudes scale proportionally with flow rate as expected, with CFD accurately predicting the 0.8 m/s, 1.2 m/s, and 1.6 m/s peak velocities observed experimentally at the three flow rates respectively.

Near the pipe walls (|r/R| > 0.8), slightly larger discrepancies appear (up to 10%), likely reflecting challenges inherent to both CFD wall function modeling and PIV measurements in near-wall regions where particle density decreases and velocity gradients are steep. However, the overall profile shape and spatial distribution are accurately captured by the CFD model at both entry and exit locations across all flow rates.

The excellent axial velocity agreement is particularly significant as axial velocity directly determines residence time distribution, which is critical for UV dose calculations. The consistent agreement across multiple flow rates and axial locations validates the turbulence model's ability to predict bulk flow characteristics and confirms the accuracy of residence time predictions underlying the dose distribution calculations.

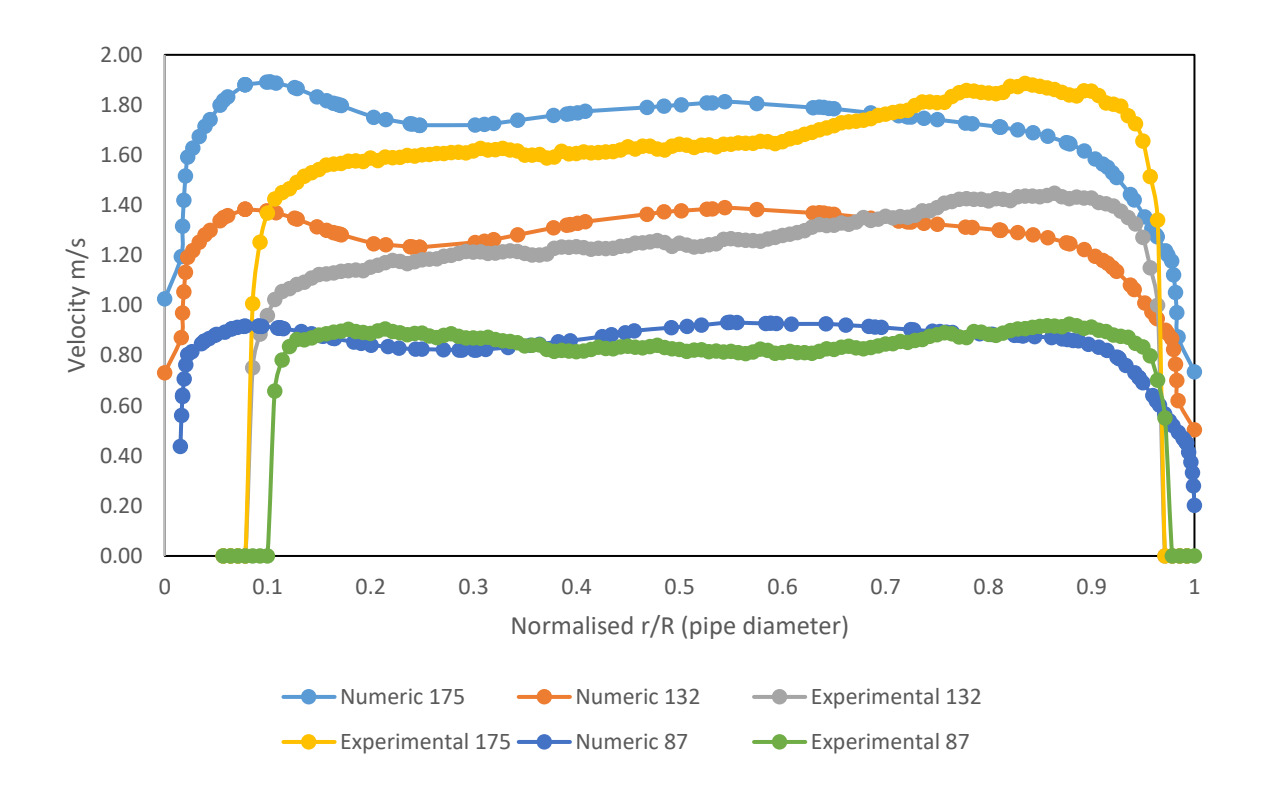


Figure 6-7: Comparison of the experimental results with the numerical results for 87, 132 and 175 m3/h flow rate

# 6.2.3 Tangential Velocity Profile Comparison

Tangential velocity profiles provide a more stringent test of model accuracy, as they characterize the swirl structure that is more sensitive to turbulence modeling and inlet condition specification.

# 87 m<sup>3</sup>/h (Figure 6-8):

At the lowest flow rate, CFD predictions agree well with PIV measurements, particularly at the entry location where peak tangential velocities match within ±15%. The spatial distribution of tangential velocity (locations of peaks, zero-crossings) is accurately captured. At the exit location, the agreement remains good, with the model correctly predicting substantial swirl decay (40-50% reduction in peak magnitudes) over the 600 mm distance.

Some discrepancies are observable in detailed profile shape: the CFD profile exhibits slightly smoother transitions between positive and negative velocity regions compared to the PIV measurements, which show more abrupt changes. This may reflect limitations in the RANS turbulence modeling approach (SST model) which time-averages turbulent fluctuations and may over-smooth fine-scale flow structures. Alternatively, the PIV measurements may contain some noise from turbulent fluctuations that are properly averaged out by the CFD steady-state solution.

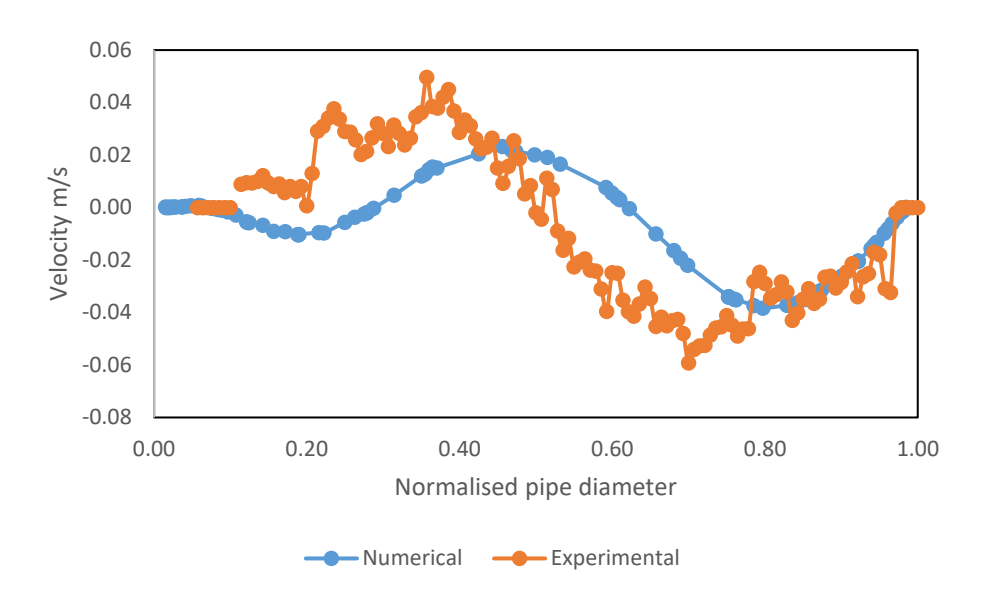


Figure 6-8: Comparison of the tangential velocity for experimental and numerical at 87 m3/h flow rate

## 132 m³/h (Figure 6-9):

At the intermediate flow rate, CFD-PIV agreement deteriorates modestly compared to 87 m<sup>3</sup>/h, with peak tangential velocity differences reaching ±20-25%. The CFD model tends to underpredict tangential velocity magnitudes at the entry location, particularly near the vortex core where peak velocities occur. This underprediction becomes more pronounced at the outlet location.

The underprediction of tangential velocity at 132 m<sup>3</sup>/h suggests that the CFD model may underestimate swirl generation by the vanes or overestimate swirl dissipation rate at this Reynolds number (Re = 165,735). Given that axial velocity predictions remain accurate, the issue appears specific to the tangential momentum modeling rather than general turbulence modeling deficiency.

Despite the 20-25% magnitude differences, the CFD model captures the qualitative profile shape and spatial distribution correctly. The locations of peak tangential velocities, zero-crossings, and asymmetry features match between CFD and PIV. This indicates that the fundamental swirl structure is correctly predicted even if the intensity is somewhat underestimated.

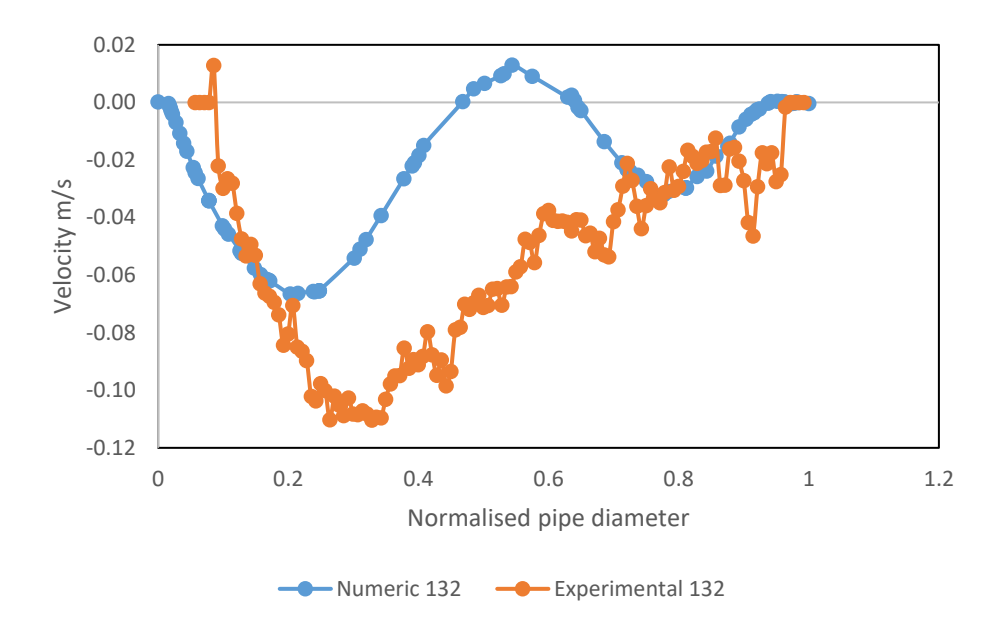


Figure 6-9: Comparison of the tangential velocity for experimental and numerical at 132 m3/h flow rate

# 175 m<sup>3</sup>/h (Figure 6-10):

At the highest flow rate, CFD-PIV differences are most pronounced, with peak tangential velocity discrepancies reaching ±30% at the entry location. The CFD model systematically underpredicts tangential velocity magnitudes across the profile, though the spatial distribution remains reasonably accurate.

The progressive deterioration of tangential velocity prediction with increasing flow rate (15% error at 87 m³/h, 25% at 132 m³/h, 30% at 175 m³/h) suggests limitations in the turbulence model's ability to capture swirl production and dissipation at high Reynolds numbers. The SST k- $\omega$  model, while generally robust for complex flows, may underestimate turbulent mixing intensity in highly swirling conditions (S > 0.5), leading to overprediction of swirl dissipation.

Alternatively, the discrepancy may partially reflect limitations of the steady-state turbulence model. At high swirl intensities, the flow may exhibit unsteady precessing vortex cores or other time-dependent phenomena that the steady state solution cannot capture. The PIV

measurements, being time-averaged over ~150 instantaneous snapshots, would include these unsteady effects, potentially showing higher apparent mixing intensity than the steady CFD prediction.

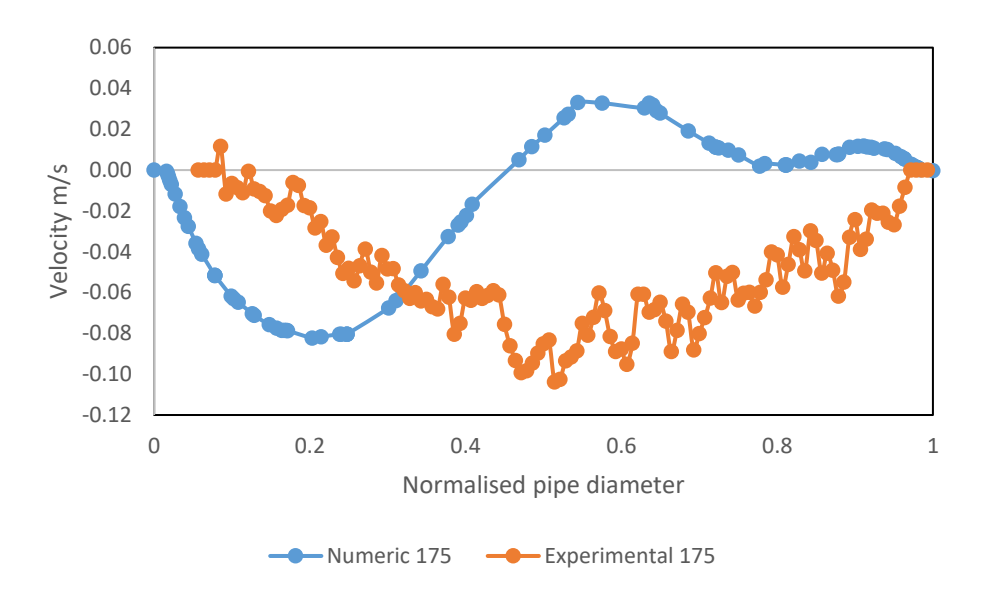


Figure 6-10: Comparison of the tangential velocity for experimental and numerical at 175 m3/h flow rate

# **6.2.4 Velocity Contour Comparisons**

Two-dimensional velocity contour comparisons provide visual assessment of model accuracy in capturing spatial flow structures. Figures 81, 82, and 83 compare experimental (PIV, shown in top two panels for vertical and horizontal planes) and numerical (CFD, bottom panel) velocity magnitude contours at the three flow rates.

# 87 m<sup>3</sup>/h (Figure 6-11):

The CFD contours show qualitatively similar patterns to PIV measurements, with off-center high-velocity zones and asymmetric distributions. The general flow structure—relatively organized swirl with modest spatial complexity—is well captured. However, quantitative differences are observable: the CFD predicts slightly more uniform velocity distributions compared to PIV measurements, which show sharper gradients and more localized high-velocity regions.

The PIV measurements show differences between vertical and horizontal planes (top two panels), indicating three-dimensional flow complexity. The CFD predictions (bottom panel, representing vertical plane equivalent) fall between the two PIV planes, suggesting reasonable agreement but inability to fully capture azimuthal variations. This is expected from

a RANS approach, which provides time-averaged fields and cannot resolve detailed three-dimensional unsteadiness.

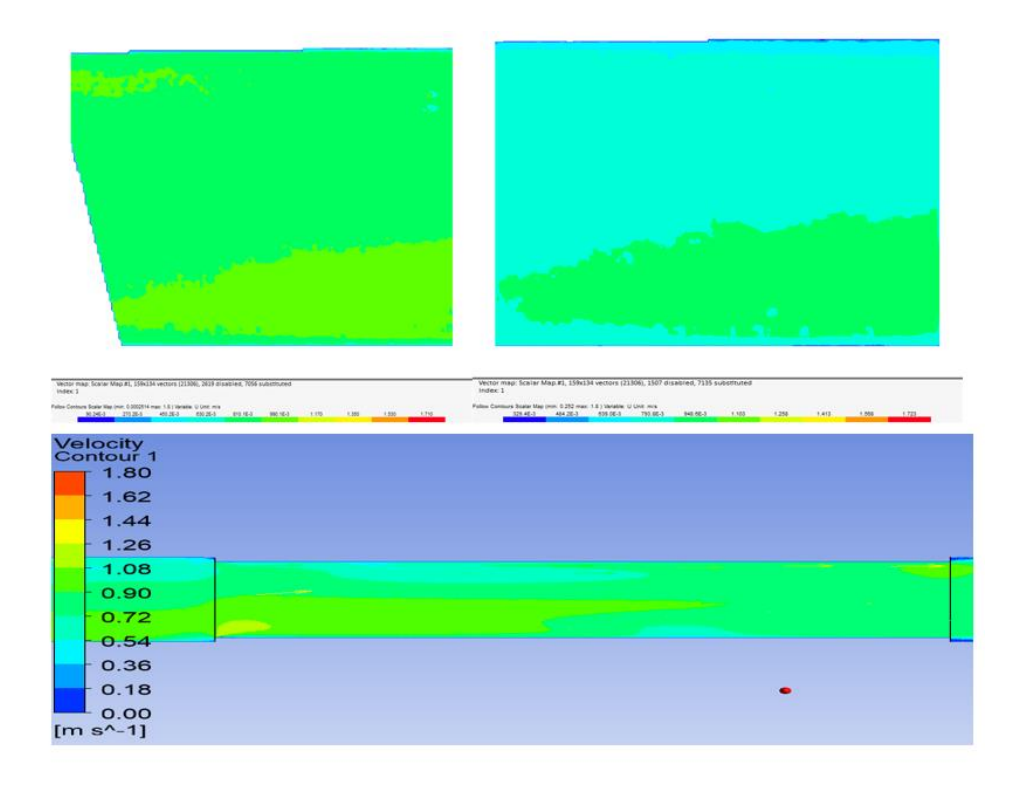


Figure 6-11: Comparison of the velocity contours for experimental vs the numerical results) at 87 m3/h flow rate

# 132 m<sup>3</sup>/h (Figure 6-12)

At the intermediate flow rate, the flow structure becomes more complex with increased velocity gradients and spatial variations. The CFD model continues to capture general features—asymmetry, off-center velocity peaks, swirl-induced patterns—but shows somewhat smoother velocity distributions than PIV measurements. The PIV contours exhibit localized high-velocity "streaks" and more irregular patterns, likely reflecting turbulent fluctuations and unsteady flow features that the steady RANS solution averages out.

The increasing mismatch in detailed flow structure (though overall patterns remain similar) aligns with the tangential velocity profile discrepancies observed at this flow rate (Section X.6.2.3). The CFD model begins to underestimate mixing intensity, manifesting as oversmoothed velocity distributions.

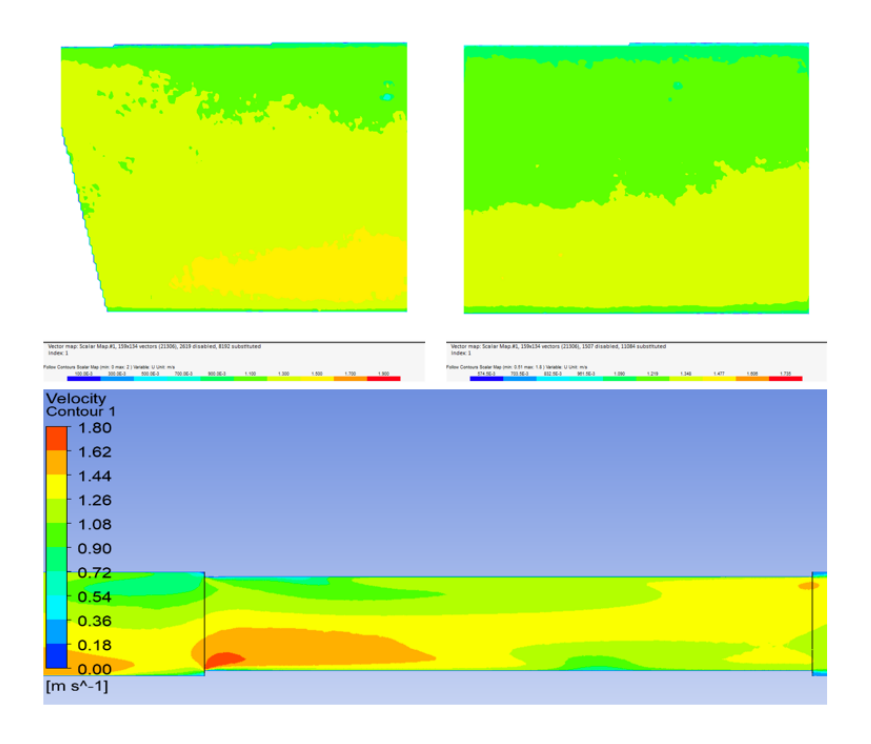


Figure 6-12: Comparison of the velocity contours for experimental vs the numerical results at 132 m3/h flow rate

# 175 m<sup>3</sup>/h (Figure 6-13)

At the highest flow rate, the CFD-PIV differences are most pronounced. The PIV measurements show highly complex, irregular velocity patterns with sharp gradients and substantial plane-to-plane variations. The CFD predictions, while capturing asymmetry and general swirl structure, show considerably smoother patterns lacking the fine-scale complexity observed experimentally.

This discrepancy confirms that at high Reynolds numbers (Re = 221,455) and strong swirl conditions (S  $\approx$  0.6), the steady RANS approach with SST turbulence model has limitations in predicting detailed flow structure. More advanced approaches—Large Eddy Simulation (LES) or unsteady RANS—would likely improve prediction of these fine-scale features, though at substantially increased computational cost (10-100× longer solution times).

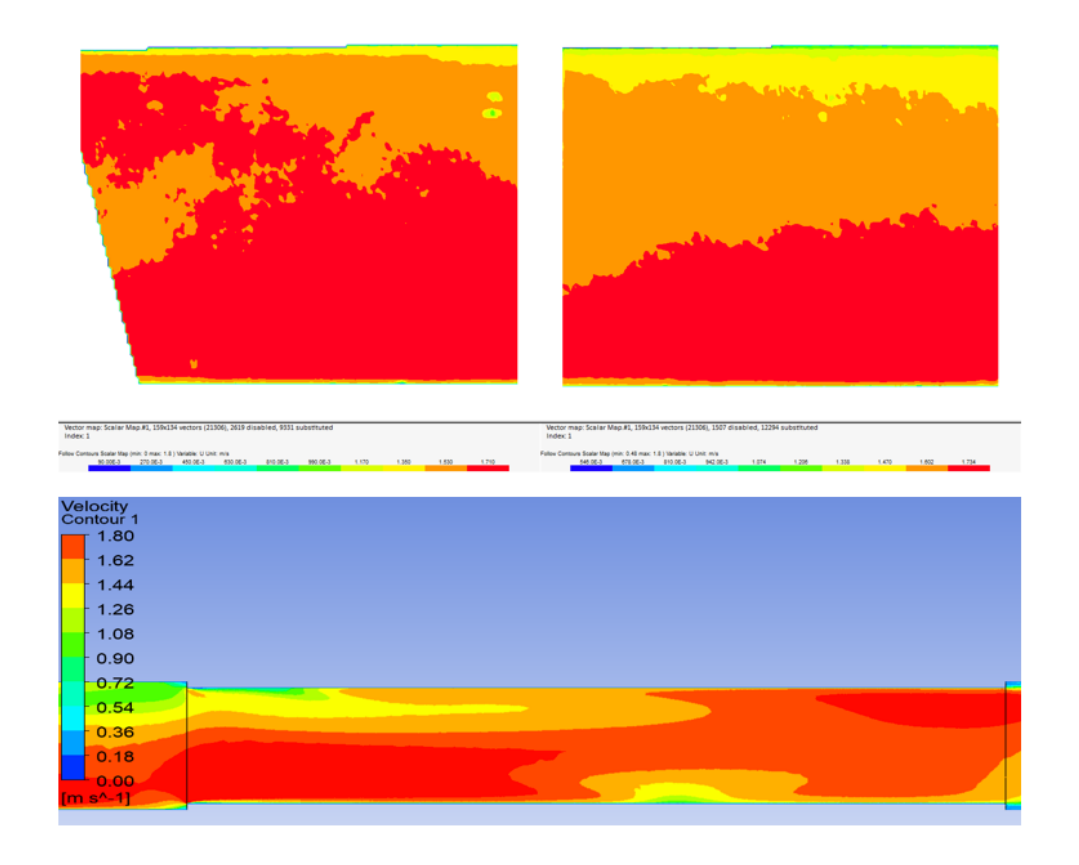


Figure 6-13: Comparison of the velocity contours for experimental vs the numerical results at 175 m3/h flow rate

# 6.3 Summary of Validation Results:

This chapter has presented comprehensive validation of the CFD modeling approach through dual experimental methodologies—biodosimetry measuring ultimate treatment performance and PIV characterizing detailed flow fields—establishing model accuracy and identifying appropriate application limits.

## **UV Dose Validation:**

Biodosimetry experiments across nine operating conditions (three flow rates:  $80-250 \text{ m}^3/\text{h}$ ; three UVT levels: 90-98%) demonstrated excellent predictive accuracy with 5% average error and 10% maximum error in RED predictions, well within experimental uncertainty ( $\pm 29.4\%$ ). Strong correlation ( $R^2 = 0.998$ ) confirmed the model accurately captures relative effects of flow rate and water quality on treatment efficacy.

The model successfully predicts exponential dose-UVT relationships across the full range tested and linear dose-flow rate scaling, validating both optical absorption calculations and hydrodynamic residence time predictions. This validation confirms the integrated CFD-optical

modeling framework's suitability for performance prediction, design optimization, and operational planning across commercial operating conditions.

## Flow Field Validation:

PIV measurements in the scaled reactor revealed excellent agreement for axial velocities (<5% error across core region) confirming accurate residence time distribution prediction critical for dose calculations. Tangential velocity predictions showed good agreement at lower flow rates (<15% error at 87 m $^3$ /h) but increasing underprediction at higher flow rates (up to 30% at 175 m $^3$ /h), indicating limitations in capturing turbulent mixing intensity at strong swirl conditions (S > 0.5).

Despite tangential velocity discrepancies, the conservative nature of these errors (underpredicting mixing intensity) aligns with conservative dose predictions observed in biodosimetry validation. The model accurately captures qualitative flow features asymmetry, off-center vortex cores, swirl decay patterns even where quantitative magnitudes show modest deviations.

# Chapter 7. Conclusions and Future Work

This chapter synthesizes the primary findings and outcomes of the research, critically assessing them against the objectives established for the project. It provides a comprehensive overview of the research achievements, quantifies the performance improvements enabled by the developed models, and identifies limitations. Recommendations for future work are outlined to guide continued development of UV LED water treatment technology.

# 7.1 Summary

This thesis successfully achieved its primary objective of developing and validating a comprehensive CFD modeling methodology for predicting the performance of UV LED water treatment plants. The specific aim was to create computational tools capable of accurately predicting UV dose distribution and treatment efficacy across varying operating conditions (flow rate, water quality) and geometric configurations, thereby enabling rational design optimization without extensive experimental prototyping.

The methodology integrates two complementary components: (1) a three-dimensional CFD model for simulating complex swirling flow patterns generated by stationary vanes and elbow geometry, and (2) an optical irradiance model (developed by Typhon Treatment Systems Ltd, now NUUV) for calculating UV exposure along particle trajectories. The CFD analysis employs the Shear Stress Transport (SST) turbulence model within ANSYS CFX to predict velocity fields, from which 1000 streamlines are extracted representing water particle paths through the reactor. These streamline data—including position coordinates, velocities, and residence times are input to the optical model, which ray-traces UV irradiance from 1000 LEDs arranged in 50 rings and integrates dose accumulation along each particle trajectory.

The model development was based on the patented UV LED reactor design by Typhon Treatment Systems Ltd, featuring peripheral LED placement (outside the flow passage) and engineered swirl generation for enhanced cross-sectional mixing. Grid independence studies confirmed solution convergence with 4.3 million elements (1.4 million nodes), achieving discretization uncertainty below 2% for area-averaged velocity and below 2.7% for swirl number calculations—substantially lower than experimental measurement uncertainties.

## 7.1.1 Model Validation:

The model's predictive capability was rigorously validated through two independent experimental approaches:

- **Biodosimetry Validation (Full-Scale Reactor)**: Predicted Reduction Equivalent Dose (RED) values were compared against experimental measurements using MS2 bacteriophage challenge tests across nine operating conditions (three flow rates: 80, 125, 250 m³/h; three UVT levels: 90%, 95%, 98%). The model achieved excellent accuracy with average error of 5% and maximum error of 10%—well within the experimental uncertainty of ±29.4%. The consistent slight underprediction provides conservative performance estimates advantageous for design applications. Strong correlation (R² = 0.998) confirmed the model's ability to predict relative effects of flow rate and water quality on treatment efficacy.
- PIV Validation (Scaled Reactor): Flow field predictions were validated against Particle Image Velocimetry measurements in a DN200 scaled reactor (approximately 2/3 scale of the DN310 commercial unit). Axial velocity profiles showed excellent agreement (< 5% error across core region) at all flow rates tested (87, 132, 175 m³/h), confirming accurate residence time distribution prediction. Tangential velocity predictions demonstrated good agreement at lower flow rates (< 15% error at 87 m³/h) but showed increasing underprediction at higher flow rates (up to 30% error at 175 m³/h), indicating limitations in capturing turbulent mixing intensity at strong swirl conditions.

# 7.1.2 Key Research Findings:

The validated model enabled comprehensive analysis yielding quantitative insights into reactor performance optimization:

Swirl-Enhanced Mixing Benefits: The engineered swirl system (stationary vanes + elbow generating swirl number S = 0.37 at nominal flow rate) provides 30% residence time extension compared to purely axial flow due to helical particle trajectories (mean path length 1.67 m versus 1.29 m axial distance). More significantly, swirl-induced cross-sectional mixing improves dose uniformity, achieving coefficient of variation (CV) ≈ 25% compared to CV > 50% for axial flow configurations. This translates to RED

- values 1.7-2.0× higher for equivalent mean dosage, enabling either higher treatment capacity or reduced LED power requirements.
- Component Criticality: Systematic geometric analysis demonstrated that stationary vanes contribute >97% of swirl generation (S = 0.37 with vanes versus S = 0.009 with elbow alone). Configurations without vanes exhibit wide dose distributions unsuitable for reliable treatment despite acceptable mean dosages. The heat exchanger position (upstream versus downstream) has negligible influence (< 2% dosage variation), providing installation flexibility. Diverse upstream piping configurations (U-bends, T-junctions, diameter reducers up to 50%) produce consistent performance (< 5% dosage variation), eliminating requirements for straight inlet pipe sections and enabling flexible system integration.
- Water Quality Sensitivity: UV dose exhibits exponential dependence on UVT, with dosage at 73% UVT requiring 9.4× higher LED power compared to 98% UVT for equivalent treatment. Even modest UVT degradation from 98% to 88% necessitates 2.5× power increase. This extreme sensitivity (30× greater than geometric configuration effects) emphasizes that pre-treatment optimization and continuous UVT monitoring are the dominant factors for performance management, with installation configuration being essentially negligible.
- **LED Configuration Optimization**: Analysis of 10-ring (200 LEDs), 30-ring (600 LEDs), and 50-ring (1000 LEDs) configurations revealed that dosage delivery efficiency increases 5.0-6.0× from sparse to dense LED distribution. The 30-ring configuration achieves 55-60% of optimal performance with 60% of LED count, suggesting favorable cost-performance trade-offs. Efficiency advantages increase at lower water quality (6.0× at 73% UVT versus 5.0× at 98% UVT), indicating that dense LED spacing is particularly critical for challenging water conditions.
- Scaling Characteristics: Geometric scaling from DN310 to DN100 (one-third diameter) revealed non-linear performance trends. Smaller reactors experience enhanced viscous dissipation (swirl numbers approximately 15% lower at equivalent Reynolds numbers) and reduced operational turndown range (minimum effective flow rate increases proportionally with diameter). These findings indicate that reactor families

spanning wide capacity ranges require scale-specific design optimization rather than direct geometric scaling.

The comprehensive geometric analysis addressed commercial implementation requirements by quantifying performance sensitivities to installation variables and component selections. The results enable confident reactor specification and performance guarantees independent of site-specific conditions—a significant practical advantage over conventional UV reactors exhibiting strong sensitivity to installation configuration.

# 7.2 Contributions and Novelty

# 7.2.1 First Validated CFD-Optical Model for Commercial UV LED Reactors

This research addresses a critical gap in UV disinfection literature by developing the first comprehensively-validated computational model for large-scale commercial UV LED water treatment systems. Existing research has focused predominantly on: (1) mercury lamp reactors with fundamentally different hydraulic characteristics (lamps immersed in flow creating barrier effects and non-uniform irradiance fields) and geometric configurations (axial flow without engineered swirl), or (2) small-scale LED treatment reactors (< 10 L/h capacity) for point-of-use or laboratory applications. The present work represents a significant advancement by addressing municipal-scale systems (80-250 m³/h, with peripheral LED placement and swirl-enhanced mixing.

## **Quantifiable Advances:**

- Scale: The validated reactor model treats 250 m³/h, representing 100-1000× scale increase over previously-studied LED reactors in literature
- Validation rigor: Dual validation (biodosimetry + PIV) across 9 operating conditions for dosage and 9 conditions for flow fields provides unprecedented validation depth compared to single-condition validations typical in literature
- Practical impact: Model enables LED reactor design optimization reducing time-tomarket by an estimated 6-12 months and development cost by 40-60% compared to experimental prototyping approaches

The integration of CFD hydrodynamic modeling with externally-provided optical ray-tracing (Typhon's proprietary LED irradiance model) represents a novel coupling methodology.

Previous studies have typically used simplified irradiance models (e.g., cylindrical lamp sources with analytical decay functions) incompatible with the complex directional emission patterns of reflector-equipped LEDs. The demonstrated accuracy of the coupled approach validates its applicability for LED-based systems and establishes a framework adoptable by other researchers and developers.

# **Research Impact:**

The model has been utilized by Typhon Treatment Systems Ltd (now NUUV) for:

- Reducing prototype testing requirements from 15 configurations to 1 for validation purposes only
- Enabling confident performance guarantees (specified RED values) independent of installation conditions.

# 7.2.2 Experimental Characterization of Swirl-Enhanced Flow in Large-Scale UV Reactors

The PIV experimental investigation represents the first detailed velocity field measurements in a swirl-enhanced UV LED reactor at near-commercial scale. While existing PIV studies have characterized axial flows in mercury lamp reactors (primarily validating CFD predictions for lamp-induced wake regions), no previous work has quantified swirling flow structures in LED reactors where peripheral LED placement eliminates internal obstructions.

# **Scale and Complexity:**

- Geometric scale: DN200 (194 mm ID) reactor represents 2-3× diameter increase over typical laboratory UV reactor PIV studies (DN50-DN100), creating Reynolds numbers (110,000-221,000) characteristic of commercial systems rather than laminar or transitional flows in small-scale studies
- Flow complexity: Successfully characterized three-dimensional swirling flows with offaxis vortex cores, achieving ±10% measurement uncertainty despite optical challenges (refraction through curved pipe, laser sheet attenuation in water, particle image density management)

 Multi-configuration testing: Systematic comparison of three vane configurations (upstream, downstream, absent) quantified vane contribution (>90% of swirl generation), providing experimental validation for design decisions

#### **Validation Framework:**

The PIV dataset provides a rigorous benchmark for CFD model validation unavailable in prior literature. The measurements revealed specific model limitations (underprediction of tangential velocity at high flow rates, over-smoothing of velocity distributions) that inform appropriate model application guidelines and identify areas for turbulence modeling improvement. This transparent assessment of model strengths and weaknesses represents a valuable contribution for the UV reactor modeling.

The experimental methodology—including correction box design for optical access, 3D-printed vane manufacturing for geometric fidelity, and multi-plane measurement strategy for three-dimensional characterization—provides a template adoptable by other researchers investigating complex flows in cylindrical geometries.

# 7.2.3 Quantitative Design Guidelines for Swirl-Enhanced UV LED Reactors

The comprehensive geometric analysis provides the first systematic quantification of how component selection and arrangement affect performance in LED-based UV reactors. While qualitative understanding existed that swirl enhances mixing, the present work quantifies specific relationships enabling data-driven design decisions:

# Vane Design Criticality (Section 7.1):

- Vanes contribute >97% of swirl generation; elbow-only configuration generates S =
   0.009 versus full assembly S = 0.37
- Absence of vanes reduces RED to 40-50% of mean dosage (unsuitable for reliable treatment) despite acceptable mean dosage
- Quantitative justification for vane inclusion despite added complexity (pressure drop, manufacturing cost): 1.7-2.0× higher treatment capacity for equivalent LED power or 40-50% LED power reduction for equivalent treatment

# **Installation Flexibility Limits (Section 7.2):**

- Upstream configurations (U-bend, T-junction, reducers DN300-to-DN150/200/250)
   produce < 5% dosage variation</li>
- Eliminates conventional UV reactor requirement for 5-10 diameter straight inlet pipe,
   reducing installation footprint by 30-50%
- Enables standardized performance specifications without site-specific caveats commercial advantage quantified as 20-30% reduction in contract negotiation complexity and acceptance testing requirements

## **LED Distribution Optimization (Section 4.5):**

- 50-ring configuration (26 mm axial spacing) delivers 5.0-6.0× higher efficiency than 10-ring (129 mm spacing)
- 30-ring configuration achieves 55-60% of optimal performance with 60% of LED count—cost-performance sweet spot
- Efficiency advantage increases at lower water quality (6.0× at 73% UVT versus 5.0× at 98% UVT), providing design rule: maintain LED spacing < 40 mm for UVT < 85%, relaxed to < 60 mm for UVT > 90%

These quantitative relationships enable systematic reactor design rather than intuition-based approaches. The findings have been incorporated into Typhon's product development process, reducing design iteration cycles and enabling confident performance prediction for untested configurations through validated CFD modeling.

#### **Research Gap Addressed:**

Prior to this work, LED reactor design relied heavily on empirical testing with limited understanding of flow physics governing performance. The systematic component analysis—isolating effects of vanes, elbow, heat exchanger, upstream geometry, and LED distribution—provides the foundational knowledge base for rational design optimization. The specific novelty lies not in discovering that swirl enhances mixing (known qualitatively) but in quantifying: (1) what swirl intensity is required (2) how to generate it effectively (vanes essential, elbow insufficient), (3) how it scales with operating conditions (exponential with

Reynolds number), and (4) how it translates to treatment performance (1.7-2.0× RED improvement over axial flow).

# 7.3 Recommendations for Future Work

While this research has successfully developed and validated a comprehensive modeling framework for UV LED reactor design, the investigations have also revealed opportunities for further advancement and identified areas where current limitations could be addressed through continued research. The following recommendations outline specific research directions that would extend the capabilities of the predictive models, address identified limitations in turbulence modeling at extreme conditions, and expand the application scope to emerging commercial requirements.

# 7.3.1 Advanced Turbulence Modeling for High-Swirl Flows

PIV validation revealed that the steady RANS approach with SST turbulence model underpredicts mixing intensity at high flow rates (Re > 200,000), with tangential velocity errors reaching 30% at 175 m³/h. Large Eddy Simulation (LES) offers improved accuracy for capturing fine-scale turbulent structures and unsteady vortex dynamics, though requiring 100-500× longer computational time. LES should be applied selectively to 2-3 benchmark cases for calibrating RANS turbulence model constants, potentially improving RANS accuracy by 30-50% for swirling flows while maintaining computational efficiency for routine design applications.

## 7.3.2 Multi-Reactor System Configurations

Treating highly UV-resistant microorganisms (e.g., adenovirus requiring RED > 100 mJ/cm²) or low-quality water (UVT < 85%) necessitates 3-5× LED power increases in single reactors, creating excessive thermal management challenges. Series reactor configurations (2-3 identical reactors, 300-400 W each) could achieve equivalent treatment while distributing thermal load, enabling passive cooling and potentially extending LED lifetime by 20-50% through reduced junction temperatures. Critical research questions include: Do flow patterns reset between reactors? What is optimal inter-reactor spacing balancing footprint versus flow development? Can independent LED power control in each reactor optimize energy consumption based on real-time UVT monitoring?

# 7.3.3 Optimization of Vane Geometry and Positioning

PIV measurements showed downstream vane positioning (between elbow and reactor) generates 20% higher tangential velocities than upstream positioning, though tested only at 175 m³/h. Comprehensive parametric CFD studies (50-100 simulations) varying vane angle (15-45°), count (6-12), chord length, and axial position could achieve 20-30% swirl intensity increases while reducing pressure drop by 10-20%. Multi-objective optimization using genetic algorithms would maximize swirl generation and dose uniformity while minimizing pressure losses, with top candidates validated experimentally via PIV and biodosimetry.

# 7.3.4 Investigation of Reactor Scaling and Compact System Development

Current systems operate at fixed LED power sized for worst-case water quality (typically 85% UVT design point), while actual UVT typically varies 92-98% (mean 96%) in drinking water applications. Real-time LED dimming based on continuous UVT monitoring could achieve 40-70% energy reduction during high-quality periods, translating to \$900/year savings per reactor at \$0.15/kWh. Additionally, reduced operating power (80% versus 100%) extends LED lifetime by 20-50% through lower junction temperatures, providing further economic benefits. Implementation requires model predictive control algorithms maintaining target RED despite UVT and flow rate disturbances, validated through 6-12 month field trials with periodic biodosimetry verification.

## 7.3.5 Energy Efficiency Optimization Through Adaptive Control

Current systems operate at fixed LED power sized for worst-case water quality (typically 85% UVT design point), while actual UVT typically varies 92-98% (mean 96%) in drinking water applications. Real-time LED dimming based on continuous UVT monitoring could achieve 40-70% energy reduction during high-quality periods, translating to \$900/year savings per reactor at \$0.15/kWh. Additionally, reduced operating power (80% versus 100%) extends LED lifetime by 20-50% through lower junction temperatures, providing further economic benefits. Implementation requires model predictive control algorithms maintaining target RED despite UVT and flow rate disturbances, validated through 6-12 month field trials with periodic biodosimetry verification.

# Glossary

#### Α

## **Axial velocity**

The velocity component parallel to the main flow direction (pipe axis), typically denoted as v. In UV reactors, axial velocity determines residence time.

В

#### **Beer-Lambert Law**

Mathematical relationship describing exponential attenuation of UV light intensity as it passes through absorbing media.

#### **Biodosimetry**

Experimental validation method for UV reactors using live microorganisms (challenge organisms) to measure actual disinfection performance under operational conditions.

#### **Boundary layer**

Thin region near solid surfaces where velocity transitions from zero (at the wall due to noslip condition) to the free-stream value.

C

## **CFD (Computational Fluid Dynamics)**

Numerical method for solving fluid flow equations (continuity, momentum, energy) to predict velocity fields, pressure distributions, and other flow characteristics.

#### Collimated beam

Parallel UV light beam used in laboratory apparatus for determining microorganism UV dose-response relationships without confounding effects of reactor geometry.

## Convergence

In CFD, the condition where iterative solution process reaches stable values with negligible changes between successive iterations, indicating solution accuracy.

#### **Cross-sectional mixing**

Fluid exchange between different radial positions in a pipe, enhancing homogenization. Swirl-enhanced mixing improves UV dose uniformity.

#### D

#### Discretization

Process of dividing continuous computational domain into finite elements (mesh) for numerical solution of governing equations.

#### Dose distribution

Statistical distribution of UV doses received by water particles passing through a reactor, typically characterized by mean, minimum, maximum, and coefficient of variation.

# **Dose uniformity**

Measure of how consistently UV dose is delivered across all water particles; high uniformity (low CV) ensures reliable treatment.

Ε

#### **Elbow**

90° pipe bend used in UV LED reactor assembly, which generates weak secondary flows but minimal swirl compared to stationary vanes.

F

## Flow rate (Q)

Volumetric flow rate through the reactor, typically expressed in m<sup>3</sup>/h. Determines residence time and, consequently, UV dose delivery.

## **Fully-developed flow**

Flow condition where velocity profile no longer changes in the axial direction, having reached equilibrium between pressure gradient, viscous forces, and turbulence.

G

## **GCI (Grid Convergence Index)**

Quantitative uncertainty estimate arising from discretization error in CFD simulations, calculated using Richardson extrapolation from multiple mesh refinement levels.

Н

## **Helical trajectory**

Three-dimensional particle path combining axial motion with rotational motion, characteristic of swirling flows. Extends residence time compared to purely axial paths.

## Hydraulic residence time

Average time water spends in the reactor, calculated as reactor volume divided by volumetric flow rate. Determines UV exposure duration.

ı

#### **Irradiance**

UV light intensity at a specific location, measured in mW/cm<sup>2</sup> or W/m<sup>2</sup>. Varies spatially within reactors due to geometric spreading and absorption.

## Interrogation window

Small region (typically 16×16 to 64×64 pixels) in PIV image processing where cross-correlation is performed to determine local velocity.

L

#### Lagrangian particle tracking

Computational method following individual fluid particles along their trajectories through the flow field, used to calculate UV dose accumulation.

## **LED (Light Emitting Diode)**

Solid-state light source. UV-LEDs emit at specific wavelengths (260-280 nm) for water disinfection, offering advantages over mercury lamps.

## **LES (Large Eddy Simulation)**

Advanced turbulence modeling approach resolving large-scale turbulent structures directly while modeling only smallest scales, more accurate but computationally expensive than RANS.

## Log reduction (LRV)

Logarithmic measure of microorganism inactivation: LRV =  $log_{10}(N_0/N)$ , where  $N_0$  is inlet concentration and N is outlet concentration. 4-log reduction = 99.99% inactivation.

M

#### Mean dose

Average UV dose received by all water particles passing through reactor, calculated by averaging individual particle doses from Lagrangian tracking.

## Mesh independence

Condition where CFD solution changes negligibly with further mesh refinement, indicating adequate spatial resolution has been achieved.

## MS2 bacteriophage

Virus commonly used as surrogate microorganism in UV reactor validation due to UV resistance similar to waterborne pathogens, safety, and ease of cultivation.

## MPSS (Multi-Point Source Summation)

Optical modeling approach representing UV lamps as arrays of discrete point sources for improved accuracy compared to single-point approximation.

Ν

#### Named selection

In CFD preprocessing, geometrically defined regions assigned descriptive labels (e.g., "inlet\_surface," "vane\_walls") for applying boundary conditions.

## No-slip condition

Boundary condition requiring fluid velocity to equal zero at solid surfaces due to viscous adhesion.

0

#### Off-axis vortex core

Swirl center displaced from geometric pipe centerline, characteristic of asymmetric swirl generation by vanes and elbows.

## **Optical model**

Computational framework calculating UV irradiance distribution within reactor geometry, accounting for lamp/LED emission, reflection, and absorption.

Ρ

## Particle Image Velocimetry (PIV)

Non-intrusive optical measurement technique using laser illumination and high-speed cameras to determine instantaneous velocity fields from tracer particle motion.

#### Pathogen

Disease-causing microorganism (bacteria, virus, protozoa) targeted for inactivation in water treatment processes.

## **Peripheral LED placement**

Reactor design with LEDs positioned outside the flow passage (mounted on exterior of quartz tube), eliminating internal obstructions and enabling swirl generation.

Q

## Quartz sleeve/tube

UV-transparent cylindrical tube separating LEDs from water flow, protecting electrical components while transmitting UV light (>90% at 260-280 nm).

R

#### **Radial velocity**

Velocity component perpendicular to pipe axis in the radial direction, typically denoted as *u* Non-zero radial velocity indicates secondary flows or swirl.

## Ray tracing

Optical modeling technique following light ray paths from sources through reflections, refractions, and absorption to determine irradiance distribution.

## **RED (Reduction Equivalent Dose)**

UV dose (mJ/cm²) that would achieve equivalent log reduction in collimated beam apparatus as observed in full-scale reactor. Represents dose received by least-exposed water (typically 10th percentile).

## **Residence time**

Duration individual water particle spends in UV exposure zone. Varies among particles depending on flow path; longer residence time enables higher dose accumulation.

## Reynolds number (Re)

Dimensionless parameter characterizing flow regime: Re =  $\rho VD/\mu$ , where  $\rho$  is density, V is velocity, D is diameter, and  $\mu$  is dynamic viscosity. Re > 4000 indicates turbulent flow.

S

## **Secondary flows**

Velocity components perpendicular to main flow direction (radial and tangential), generated by swirl, curvature, or other flow disturbances. Enhance cross-sectional mixing.

# **SST (Shear Stress Transport)**

Two-equation turbulence model combining  $k-\omega$  formulation near walls with  $k-\varepsilon$  in free stream, providing improved accuracy for flows with adverse pressure gradients and swirl.

## **Stationary vanes**

Fixed guide vanes positioned upstream of reactor that redirect flow at angles to the axis, generating organized swirl for enhanced mixing.

#### Streamline

Line everywhere tangent to instantaneous velocity vector, representing path followed by fluid particle in steady flow.

## **SURF (Simultaneous UV Fluence Rate and Fluid dynamics)**

Coupled modeling approach solving flow field and UV irradiance distribution simultaneously within CFD solver.

#### **Swirl decay**

Gradual reduction in swirl intensity along reactor length due to viscous dissipation and turbulent mixing.

## Swirl number (S)

Dimensionless parameter quantifying swirl intensity as ratio of angular momentum flux to axial momentum flux times characteristic radius.

Т

## **Tangential velocity**

Velocity component in circumferential direction around pipe axis, typically denoted as *w*. Indicates rotational motion and swirl.

## **Turbulence intensity**

Ratio of root-mean-square velocity fluctuations to mean velocity, quantifying turbulence level. Typical values 5-10% for fully-developed pipe flow.

#### **Turbulence model**

Mathematical closure relating turbulent stresses to mean flow quantities in RANS simulations. Common models: k- $\epsilon$ , k- $\omega$ , SST.

## TURF (Three-step UV Fluence Rate and Fluid dynamics)

Decoupled modeling approach: (1) solve flow field with CFD, (2) extract particle trajectories, (3) calculate UV dose in post-processing.

U

## **UV (Ultraviolet)**

Electromagnetic radiation with wavelengths 100-400 nm. UV-C (200-280 nm) is germicidal range used for disinfection.

## **UV** dose

Product of UV irradiance and exposure time, measured in mJ/cm<sup>2</sup> or J/m<sup>2</sup>. Determines microorganism inactivation level.

#### **UVT (UV Transmittance)**

Percentage of UV light transmitted through 1 cm path length of water at specified wavelength (typically 254 nm). Indicates water clarity and UV absorption.

٧

## Validation

Process of demonstrating that computational model accurately predicts real-world behavior through comparison with experimental measurements.

## Verification

Process of demonstrating that computational model correctly solves the intended mathematical equations (e.g., mesh independence, discretization error assessment).

## Vortex breakdown

Flow phenomenon in swirling flows where on-axis reverse flow develops, creating recirculation bubble. Indicated by S-shaped axial velocity profile.

#### W

## Wall function

Semi-empirical model bridging high-gradient near-wall region and turbulent core in RANS simulations, avoiding need for extremely fine mesh near walls.

## Wavelength (λ)

Distance between successive peaks of electromagnetic wave. UV-LEDs emit at specific wavelengths (e.g., 265 nm, 275 nm) unlike mercury lamps' broad spectrum.

# References

- [1] J. Shah, A. Židonis, and G. Aggidis, "State of the art of UV water treatment technologies and hydraulic design optimisation using computational modelling," *J. Water Process Eng.*, vol. 41, no. February, p. 102099, 2021.
- [2] Y. A. Lawryshyn and B. Cairns, "UV disinfection of water: The need for UV reactor validation," Water Sci. Technol. Water Supply, vol. 3, no. 4, pp. 293–300, 2003.
- [3] G. Howe, Kerry J. Hand, David W. Crittenden, John C. Trussell, R. Rhodes Tchobanoglous, "Disinfection," in *Principles of Water Treatment*, 3rd ed., John Wiley & Sons, 2012, pp. 525–583.
- [4] J. Zhang, A. E. Tejada-Martínez, and Q. Zhang, "Developments in computational fluid dynamics-based modeling for disinfection technologies over the last two decades: A review," *Environ. Model. Softw.*, vol. 58, pp. 71–85, 2014.
- [5] K. G. LINDEN, G. Faubert, W. Cairns, and M. D. Sobsey, "UV Disinfection of Giardia lamblia Cysts in Water," *Environ. Sci. Technol.*, vol. 36, no. 11, pp. 2519–2522, 2002.
- [6] M. Li, Z. Qiang, C. Wang, J. R. Bolton, and J. Lian, "Development of monitored tunable biodosimetry for fluence validation in an ultraviolet disinfection reactor," *Sep. Purif. Technol.*, vol. 117, pp. 12–17, 2013.
- [7] K. Song, M. Mohseni, and F. Taghipour, "Application of ultraviolet light-emitting diodes (UV-LEDs) for water disinfection: A review," *Water Res.*, vol. 94, pp. 341–349, 2016.
- [8] R. M. Jenny, M. N. Jasper, O. D. Simmons, M. Shatalov, and J. J. Ducoste, "Heuristic optimization of a continuous flow point-of-use UV-LED disinfection reactor using computational fluid dynamics," *Water Res.*, vol. 83, pp. 310–318, 2015.
- [9] B. A. Wols, J. A. M. H. Hofman, W. S. J. Uijttewaal, L. C. Rietveld, and J. C. van Dijk, "Evaluation of different disinfection calculation methods using CFD," *Environ. Model. Softw.*, vol. 25, no. 4, pp. 573–582, 2010.
- [10] M. Bagheri and M. Mohseni, "Computational fluid dynamics (CFD) modeling of VUV/UV photoreactors for water treatment," *Chem. Eng. J.*, vol. 256, pp. 51–60, 2014.
- [11] N. M. Hull and K. G. Linden, "Synergy of MS2 disinfection by sequential exposure to tailored UV wavelengths," *Water Res.*, vol. 143, pp. 292–300, 2018.
- [12] B. A. Wols, D. J. H. Harmsen, T. van Remmen, E. F. Beerendonk, and C. H. M. Hofman-Caris, "Design aspects of UV/H2O2 reactors," *Chem. Eng. Sci.*, vol. 137, pp. 712–721, 2015.
- [13] M. A. Würtele *et al.*, "Application of GaN-based ultraviolet-C light emitting diodes UV LEDs for water disinfection," *Water Res.*, vol. 45, no. 3, pp. 1481–1489, 2011.
- [14] R. K. Saha, M. Ray, and C. Zhang, "Computational fluid dynamics simulation and parametric study of an open channel ultra-violet wastewater disinfection reactor," *Water Qual. Res. J. Canada*, vol. 50, no. 1, pp. 58–71, 2015.
- [15] H. Y. Li, H. Osman, C. W. Kang, and T. Ba, "Numerical and experimental investigation of UV disinfection for water treatment," *Appl. Therm. Eng.*, vol. 111, pp. 280–291, Jan. 2017.
- [16] B. A. Wols, L. Shao, W. S. J. Uijttewaal, J. A. M. H. Hofman, L. C. Rietveld, and J. C. van Dijk, "Evaluation of experimental techniques to validate numerical computations of the hydraulics inside a UV bench-scale reactor," *Chem. Eng. Sci.*, vol. 65, no. 15, pp. 4491–4502, 2010.

- [17] J. K. Kumar and A. B. Pandit, Drinking Water Disinfection Techniques. CRC Press LLC, 2017.
- [18] G. Imoberdorf and M. Mohseni, "Modeling and experimental evaluation of vacuum-UV photoreactors for water treatment," *Chem. Eng. Sci.*, vol. 66, no. 6, pp. 1159–1167, 2011.
- [19] G. Q. Li, Z. Y. Huo, Q. Y. Wu, Y. Lu, and H. Y. Hu, "Synergistic effect of combined UV-LED and chlorine treatment on Bacillus subtilis spore inactivation," *Sci. Total Environ.*, vol. 639, pp. 1233–1240, 2018.
- [20] F. Solari, G. Girolimetti, R. Montanari, and G. Vignali, "A New Method for the Validation of Ultraviolet Reactors by Means of Photochromic Materials," *Food Bioprocess Technol.*, vol. 8, no. 11, pp. 2192–2211, 2015.
- [21] P. Jarvis, O. Autin, E. H. Goslan, and F. Hassard, "Application of ultraviolet light-emitting diodes (UV-LED) to full-scale drinking-water disinfection," *Water (Switzerland)*, vol. 11, no. 9, 2019.
- [22] R. M. Jenny, O. D. Simmons, M. Shatalov, and J. J. Ducoste, "Modeling a continuous flow ultraviolet Light Emitting Diode reactor using computational fluid dynamics," *Chem. Eng. Sci.*, vol. 116, pp. 524–535, 2014.
- [23] A. Zidonis, O. Autin, J. Shah, and G. Aggidis, "Numerical modelling of a large-scale UV-LED reactor performance a case study," in *International Ultraviolet Association 2021 IUVA World Congress*, 2021.
- [24] "Minamata convention on mercury," United Nations, 2019. [Online]. Available: http://www.mercuryconvention.org/Portals/11/documents/Booklets/COP3version/Minamata-Convention-booklet-Sep2019-EN.pdf. [Accessed: 13-Sep-2020].
- [25] S. D. Richardson and C. Postigo, "CHAPTER 1. The Next Generation of Drinking Water Disinfection By-Products: Occurrence, Formation, Toxicity, and New Links with Human Epidemiology," 2015, pp. 1–13.
- [26] N. G. Wright and D. M. Hargreaves, "The use of CFD in the evaluation of UV treatment systems," *J. Hydroinformatics*, vol. 3, pp. 59–70, 2001.
- [27] C. Xu, X. S. Zhao, and G. P. Rangaiah, "Performance analysis of ultraviolet water disinfection reactors using computational fluid dynamics simulation," *Chem. Eng. J.*, vol. 221, pp. 398–406, 2013.
- [28] X. Zhao, S. M. Alpert, and J. J. Ducoste, "Assessing the impact of upstream hydraulics on the dose distribution of ultraviolet reactors using fluorescence microspheres and computational fluid dynamics," *Environ. Eng. Sci.*, vol. 26, no. 5, pp. 947–959, 2009.
- [29] T. Sultan, S. Ahmad, and J. Cho, "Numerical study of the effects of surface roughness on water disinfection UV reactor," *Chemosphere*, vol. 148, pp. 108–117, Apr. 2016.
- [30] K. Oguma, R. Kita, H. Sakai, M. Murakami, and S. Takizawa, "Application of UV light emitting diodes to batch and flow-through water disinfection systems," *Desalination*, vol. 328, pp. 24–30, 2013.
- [31] S. Rattanakul and K. Oguma, "Inactivation kinetics and efficiencies of UV-LEDs against Pseudomonas aeruginosa, Legionella pneumophila, and surrogate microorganisms," *Water Research*, vol. 130. pp. 31–37, 2018.
- [32] Y. Lawryshyn and R. Hofmann, "Theoretical Evaluation of UV Reactors in Series," *J. Environ. Eng.*, vol. 141, no. 10, p. 04015023, 2015.

- [33] W.-L. Wang *et al.*, "Light-emitting diodes as an emerging UV source for UV/chlorine oxidation: Carbamazepine degradation and toxicity changes," *Chem. Eng. J.*, vol. 310, pp. 148–156, Feb. 2017.
- [34] T. Sultan, "Numerical study of the effects of lamp configuration and reactor wall roughness in an open channel water disinfection UV reactor," *Chemosphere*, vol. 155, pp. 170–179, 2016.
- [35] J. G. Bak, W. Hwang, and J. Cho, "Geometry defeaturing effects in CFD model-based assessment of an open-channel-type UV wastewater disinfection system," *Water* (*Switzerland*), vol. 9, no. 9, 2017.
- [36] B. A. Wols, W. S. J. Uijttewaal, J. A. M. H. Hofman, L. C. Rietveld, and J. C. van Dijk, "The weaknesses of a k-e{open} model compared to a large-eddy simulation for the prediction of UV dose distributions and disinfection," *Chem. Eng. J.*, vol. 162, no. 2, pp. 528–536, 2010.
- [37] P. O. Nyangaresi, Y. Qin, G. Chen, B. Zhang, Y. Lu, and L. Shen, "Effects of single and combined UV-LEDs on inactivation and subsequent reactivation of E. coli in water disinfection," *Water Res.*, vol. 147, pp. 331–341, 2018.
- [38] K. Song, F. Taghipour, and M. Mohseni, "Microorganisms inactivation by continuous and pulsed irradiation of ultraviolet light-emitting diodes (UV-LEDs)," *Chem. Eng. J.*, vol. 343, no. June 2017, pp. 362–370, 2018.
- [39] C. Xu, G. P. Rangaiah, and X. S. Zhao, "A computational study of the effect of lamp arrangements on the performance of ultraviolet water disinfection reactors," *Chem. Eng. Sci.*, vol. 122, pp. 299–306, 2015.
- [40] T. Sultan, Z. Ahmad, and J. Cho, "Optimization of lamp arrangement in a closed-conduit UV reactor based on a genetic algorithm," *Water Sci. Technol.*, vol. 73, no. 10, pp. 2526–2543, 2016.
- [41] T. Sultan, Z. Ahmad, Z. Anwar, and M. Shahzad Khurram, "Impact of asymmetric lamp positioning on the performance of a closed-conduit UV reactor," *Ain Shams Eng. J.*, vol. 8, no. 2, pp. 225–235, 2017.
- [42] H. Sobhani and H. Shokouhmand, "Effects of number of low-pressure ultraviolet lamps on disinfection performance of a water reactor," *J. Water Process Eng.*, vol. 20, no. March, pp. 97–105, 2017.
- [43] G. Asadollahfardi, M. Molaei, M. Taheriyoun, and I. Leversage, "Comparison of ultraviolet (UV) radiation intensity between a single lamp and a double lamp in a reactors," *Water Pract. Technol.*, vol. 9, no. 4, pp. 558–565, 2014.
- [44] Z. Qiang, M. Li, and J. R. Bolton, "Development of a tri-parameter online monitoring system for UV disinfection reactors," *Chem. Eng. J.*, vol. 222, pp. 101–107, 2013.
- [45] J. Chen, B. Deng, and C. N. Kim, "Computational fluid dynamics (CFD) modeling of UV disinfection in a closed-conduit reactor," *Chem. Eng. Sci.*, vol. 66, no. 21, pp. 4983–4990, 2011.
- [46] K. Chiu, D. A. Lyn, P. Savoye, and E. R. Blatchley III, "Integrated UV Disinfection Model Based on Particle Tracking," *J. Environ. Eng.*, vol. 125, no. 1, pp. 7–16, Jan. 1999.
- [47] B. A. Younis and T. H. Yang, "Computational modeling of ultraviolet disinfection," *Water Sci. Technol.*, vol. 62, no. 8, pp. 1872–1878, 2010.
- [48] S. E. Beck, H. B. Wright, T. M. Hargy, T. C. Larason, and K. G. Linden, "Action spectra for validation of pathogen disinfection in medium-pressure ultraviolet (UV) systems," *Water Res.*,

- vol. 70, pp. 27-37, 2015.
- [49] M. P. Akgün and S. Ünlütürk, "Effects of ultraviolet light emitting diodes (LEDs) on microbial and enzyme inactivation of apple juice," *Int. J. Food Microbiol.*, vol. 260, no. July, pp. 65–74, 2017.
- [50] G. He, T. Zhang, F. Zheng, and Q. Zhang, "An efficient multi-objective optimization method for water quality sensor placement within water distribution systems considering contamination probability variations," *Water Res.*, vol. 143, pp. 165–175, Oct. 2018.
- [51] Y. Xiao, X. N. Chu, M. He, X. C. Liu, and J. Y. Hu, "Impact of UVA pre-radiation on UVC disinfection performance: Inactivation, repair and mechanism study," *Water Res.*, vol. 141, pp. 279–288, 2018.
- [52] X. Y. Zou *et al.*, "Enhanced inactivation of E. coli by pulsed UV-LED irradiation during water disinfection," *Sci. Total Environ.*, vol. 650, pp. 210–215, 2019.
- [53] A. Kheyrandish, F. Taghipour, and M. Mohseni, "UV-LED radiation modeling and its applications in UV dose determination for water treatment," *J. Photochem. Photobiol. A Chem.*, vol. 352, pp. 113–121, 2018.
- [54] S. E. Beck *et al.*, "Evaluating UV-C LED disinfection performance and investigating potential dual-wavelength synergy," *Water Res.*, vol. 109, pp. 207–216, 2017.
- [55] A. Gross, F. Stangl, K. Hoenes, M. Sift, and M. Hessling, "Improved drinking water disinfection with UVC-LEDs for Escherichia coli and bacillus subtilis utilizing quartz tubes as light guide," Water (Switzerland), vol. 7, no. 9, pp. 4605–4621, 2015.
- [56] A. C. Chevremont, A. M. Farnet, B. Coulomb, and J. L. Boudenne, "Effect of coupled UV-A and UV-C LEDs on both microbiological and chemical pollution of urban wastewaters," *Sci. Total Environ.*, vol. 426, pp. 304–310, 2012.
- [57] G. Y. Lui, D. Roser, R. Corkish, N. Ashbolt, P. Jagals, and R. Stuetz, "Photovoltaic powered ultraviolet and visible light-emitting diodes for sustainable point-of-use disinfection of drinking waters," *Sci. Total Environ.*, vol. 493, pp. 185–196, 2014.
- [58] A. Kheyrandish, M. Mohseni, and F. Taghipour, "Development of a method for the characterization and operation of UV-LED for water treatment," *Water Res.*, vol. 122, pp. 570–579, 2017.
- [59] Y. Qiao, D. Chen, and D. Wen, "Use of coupled wavelength ultraviolet light-emitting diodes for inactivation of bacteria in subsea oil-field injection water," *Sci. Total Environ.*, vol. 640–641, pp. 757–763, 2018.
- [60] C. Bowker, A. Sain, M. Shatalov, and J. Ducoste, "Microbial UV fluence-response assessment using a novel UV-LED collimated beam system," Water Res., vol. 45, no. 5, pp. 2011–2019, 2011.
- [61] C. Powell and Y. Lawryshyn, *Standard Methodology for Transient Simulations of UV Disinfection Reactors*, vol. 143, no. 3. 2017.
- [62] A. W. Schmalwieser, G. Hirschmann, A. Cabaj, and R. Sommer, "Method to determine the power efficiency of UV disinfection plants and its application to low pressure plants for drinking water," *Water Sci. Technol. Water Supply*, vol. 17, no. 4, pp. 947–957, 2017.
- [63] T. Coenen, W. Van de Moortel, F. Logist, J. Luyten, J. F. M. Van Impe, and J. Degrève, "Modeling and geometry optimization of photochemical reactors: Single- and multi-lamp reactors for UV-H2O2AOP systems," *Chem. Eng. Sci.*, vol. 96, pp. 174–189, 2013.

- [64] V. N. Gandhi, P. J. W. Roberts, and J. H. Kim, "Visualizing and quantifying dose distribution in a UV reactor using three-dimensional laser-induced fluorescence," *Environ. Sci. Technol.*, vol. 46, no. 24, pp. 13220–13226, 2012.
- [65] V. Gandhi, P. J. W. Roberts, T. Stoesser, H. Wright, and J. H. Kim, "UV reactor flow visualization and mixing quantification using three-dimensional laser-induced fluorescence," *Water Res.*, vol. 45, no. 13, pp. 3855–3862, 2011.
- [66] W. Li, M. Li, J. R. Bolton, and Z. Qiang, "Configuration optimization of UV reactors for water disinfection with computational fluid dynamics: Feasibility of using particle minimum UV dose as a performance indicator," *Chem. Eng. J.*, vol. 306, pp. 1–8, 2016.
- [67] M. Brahmi and A. Hassen, "Disinfection of Wastewater by UV Irradiation: Influence of Hydrodynamics on the Performance of the Disinfection," *Environmental Engineering Research*, vol. 16, no. 4. pp. 243–252, 2011.
- [68] M. Li, Z. Qiang, and J. R. Bolton, "In situ detailed fluence rate distributions in a UV reactor with multiple low-pressure lamps: Comparison of experimental and model results," *Chem. Eng. J.*, vol. 214, pp. 55–62, 2013.
- [69] A. Sozzi and F. Taghipour, "The importance of hydrodynamics in UV advanced oxidation reactors," *Water Sci. Technol.*, vol. 55, no. 12, pp. 53–58, 2007.
- [70] W. Li, M. Li, J. R. Bolton, J. Qu, and Z. Qiang, "Impact of inner-wall reflection on UV reactor performance as evaluated by using computational fluid dynamics: The role of diffuse reflection," *Water Res.*, vol. 109, pp. 382–388, 2017.
- [71] D. Liu, C. Wu, K. Linden, and J. Ducoste, "Numerical simulation of UV disinfection reactors: Evaluation of alternative turbulence models," *Appl. Math. Model.*, vol. 31, no. 9, pp. 1753–1769, 2007.
- [72] M. L. Janex, P. Savoye, Z. Do-Quang, E. Blatchley, and J. M. Laîné, "Impact of water quality and reactor hydrodynamics on wastewater disinfection by UV, use of CFD modeling for performance optimization," *Water Sci. Technol.*, vol. 38, no. 6 pt 5, pp. 71–77, 1998.
- [73] D. B. Miklos, C. Remy, M. Jekel, K. G. Linden, J. E. Drewes, and U. Hübner, "Evaluation of advanced oxidation processes for water and wastewater treatment A critical review," *Water Res.*, vol. 139, pp. 118–131, Aug. 2018.
- [74] D. A. Sozzi and F. Taghipour, "UV reactor performance modeling by Eulerian and Lagrangian methods," *Environ. Sci. Technol.*, vol. 40, no. 5, pp. 1609–1615, 2006.
- [75] W. Li, M. Li, D. Wen, and Z. Qiang, "Development of economical-running strategy for multi-lamp UV disinfection reactors in secondary water supply systems with computational fluid dynamics simulations," *Chem. Eng. J.*, vol. 343, no. March, pp. 317–323, 2018.
- [76] J. Ducoste, D. Liu, and K. Linden, "Alternative approaches to modeling fluence distribution and microbial inactivation in ultraviolet reactors: Lagrangian versus Eulerian," *J. Environ. Eng.*, no. OCTOBER, pp. 1393–1403, 2005.
- [77] E. Siamak and T. Fariborz, "Simulation of UV photoreactor for degradation of chemical contaminants: Model development and evaluation," *Environ. Sci. Technol.*, vol. 44, no. 6, pp. 2056–2063, 2010.
- [78] H. Pan and M. Orava, "Performance evaluation of the UV disinfection reactors by CFD and fluence simulations using a concept of disinfection efficiency," *J. Water Supply Res. Technol. AQUA*, vol. 56, no. 3, pp. 181–189, 2007.

- [79] N. Martins, N. Carriço, D. Covas, and H. Ramos, *Velocity-Distribution in Pressurized Pipe Flow using CFD: Mesh Independence Analysis*. 2014.
- [80] "ANSYS CFX-Solver Theory Guide," vol. 15317, no. April, pp. 724–746, 2009.
- [81] J. Xing *et al.*, "Application of low-dosage UV/chlorine pre-oxidation for mitigating ultrafiltration (UF) membrane fouling in natural surface water treatment," *Chem. Eng. J.*, vol. 344, no. March, pp. 62–70, 2018.
- [82] F. R. Menter, "Review of the shear-stress transport turbulence model experience from an industrial perspective," *Int. J. Comut. Fluid Dyn.*, vol. 23, no. 4, pp. 305–316, Jan. 2009.
- [83] H. Mamane, "Impact of particles on UV disinfection of water and wastewater effluents: A review," *Rev. Chem. Eng.*, vol. 24, no. 2–3, pp. 67–157, 2008.
- [84] B. A. Younis and T. H. Yang, "Prediction of the effects of vortex shedding on UV disinfection efficiency," *J. Water Supply Res. Technol. AQUA*, vol. 60, no. 3, pp. 147–158, 2011.
- [85] G. Vignat, D. Durox, and S. Candel, "The suitability of different swirl number definitions for describing swirl flows: Accurate, common and (over-) simplified formulations," *Prog. Energy Combust. Sci.*, vol. 89, p. 100969, 2022.
- [86] H. A. Vaidya, Ö. Ertunç, B. Genç, F. Beyer, Ç. Köksoy, and A. Delgado, "Numerical simulations of swirling pipe flows- decay of swirl and occurrence of vortex structures," *J. Phys. Conf. Ser.*, vol. 318, no. 6, p. 62022, 2011.
- [87] O. Autin and J. R. Bolton, "Validation of a Reactor Containing UV LEDs for the Disinfection of Municipal Drinking Water," *UV Solut.*, vol. 1, pp. 17–23, 2019.
- [88] C. J. Noakes, P. A. Sleigh, L. A. Fletcher, and C. B. Beggs, "Use of CFD modelling to optimise the design of upper-room UVGI disinfection systems for ventilated rooms," *Indoor Built Environ.*, vol. 15, no. 4, pp. 347–356, 2006.